Studies on the formation of high ice-concentration cirrus in the Tropical Tropopause Layer

Division of Earth System Science,

Graduate School of Environmental Science,

Hokkaido University

Satoru Mimura

November 2018

Abstract

The cirrus clouds in the Tropical Tropopause Layer (TTL) play an important role in regulating the amount of water entering the stratosphere, while the modulation of stratospheric water vapor drives decadal changes in global surface temperature. Progress toward a better understanding of the cirrus formation has been made by in situ observations and cloud microphysical model simulations. However, the detailed cloud physical processes in the TTL are not fully understood. Here we focus on a thin (∼20 m) TTL cirrus with high ice-particle concentration (10^4 L^{-1}) reported during the Airborne Tropical Tropopause Experiment (ATTREX) campaign. Since 10^4 L^{-1} is an implausible concentration of heterogeneous ice nuclei, we could safely assume that the ice particles are formed by homogeneous nucleation. The ice particles of a few microns in radius in the thin layer suggest that they are observed a moment after nucleation and unperturbed by sedimentation, mixing, and diffusion, which makes it ideal to investigate exclusively the ice-nucleation processes. The purpose of the present study is to identify necessary conditions to simulate the observed features for better understanding of the ice-nucleation process in the TTL. The microphysical model employed here assumes homogeneous ice nucleation under the condition of conserved potential temperature and constant cooling rate.

The ice concentration realized at the termination of growth, $n_{\mathrm{i}}^{\mathrm{max}}$, is investigated from a series of simulations assuming monodisperse aerosols. It is found that $n_{\mathrm{i}}^{\mathrm{max}}$ increases as a function of cooling rate ($-\dot{T}$) while it decreases as aerosol radius becomes large. The aerosol-size dependence becomes remarkable following the increase of aerosol size. These features are brought about by the following two effects: (a) large (small) aerosols create small (large) numbers of large (small) ice particles due to the size dependency of the growth

rate of ice particles, and (b) large (small) aerosols initiate ice nucleation at a low (high) saturation ratio.

The aerosol-size dependency of $n_{\rm i}^{\rm max}$ suggests possible interactions between the aerosols with different size. The simulations conducted by giving aerosols of bimodal size with equal number concentration reveal that number of ice, $N_{\rm i}$, always increases from that nucleated from monodisperse aerosols. This increase results from increased ice nucleation from small aerosols due to Effect (a). It is pronounced when the radius of large aerosols ($r_{\rm l}$) is large and the number concentration of small aerosols ($n_{\rm s}$) is large, but takes a maximum when the radius of small aerosols ($r_{\rm s}$) meets $r_{\rm s}/r_{\rm l} \sim 0.7$ irrespective of $r_{\rm l}$. The size distribution of nucleated ice particles is always monodisperse under the conditions of $-\dot{T} = 3.3$ K h^{-1} and $r_{\rm l} = 0.1$ μm, while bimodal distribution is realized when $-\dot{T} = 30$ K h^{-1} and $r_{\rm l} = 1.0$ μm. The separation of two peaks becomes evident when the $r_{\rm s}/r_{\rm l}$ ratio is small. These features are understood by the large cooling rate required for large aerosols due to Effect (a) that leads to the termination of nucleation prior to the differential growth of ice particles. The size dependence of the terminal velocity implies that the size distribution may be distorted in $\sim$ 2 days for ice particles nucleated under small aerosol condition, while it may be maintained for no less than 4–5 days for those under large aerosol condition.

The cooling rate necessary for the formation of the observed thin cirrus will be accompanied by short time-scale gravity waves. The ice particles simulated in this study are always larger than those observed in the whole parameter range. This is because a certain amount of water is always nucleated under observational constraints, which results in an almost constant mean radius of ice particles irrespective of the simulation parameters. This robustness suggests that ice-particle radius is underestimated or water vapor mixing ratio is overestimated in ATTREX observations. A hypothetical scenario is proposed to explain the formation and development of TTL cirrus in a single story.

Contents

List of Symbols

C_{p} : Specific heat at constant pressure

D : Diffusion coefficient

g : Gravity acceleration

J : Applied heat per unit mass

J_{c} : Homogeneous nucleation rate coefficient

k : Boltzmann's constant

K : Kelvin term

K_{n} : Knudsen number

L_{c} : Latent heat of condensation at 0°C

M_{i} : Number of water molecules contained in one ice particle

M_{w} : Molecular weight of water

n : Number concentration of aerosol particles

n_{a} : Number of moles (amount of substance) of air

n_{i} : Number concentration of ice particles

$n_{\mathrm{i}}^{\mathrm{max}}$: The maximum ice-particle concentration

n_{l} : n_{a} of large aerosol

n_{s} : n_{a} of small aerosol

n_{sc} : The critical value of n_{s} at which the first nucleating aerosol (large or small) changes

n_{v} : Number of moles (amount of substance) of water vapor

n_{v0} : Initial value of n_{v}

N : Number of aerosol particles

N_{A} : Avogadro's number

N_{i} : Number of ice particles

p : Air pressure

p_0 : Initial value of p

p_{c} : Water vapor pressure at which the ice nucleation is initiated

p_{i} : Saturation water vapor pressure over ice

p_{i0} : Initial value of p_{i}

p_{iwc} : Water vapor pressure converted from ice water content

p_{s} : Standard air pressure (= 1000 hPa)

p_{v} : Water vapor pressure

q_{s} : Saturation mixing ratio

r : Aerosol radius

r_{i} : Ice-particle radius

$\bar{r_{\mathrm{i}}}$: Mean radius of ice particles

r_{l} : r of large aerosol

r_{s} : r of small aerosol

R : Ice nucleation ratio

R_{d} : Gas constant for dry air

R^{max} : The maximum ice nucleation ratio

R^{*} : Universal gas constant

$\mathrm{RH_i}$: Relative humidity over ice

S : Ice saturation ratio

S_{c} : Critical value of S ($\mathrm{RH_i}$) for ice nucleation (ice-nucleation threshold)

t : Time

T : Air temperature

T_0 : Initial value of T

T_{c} : Critical air temperature for ice nucleation

V : Volume of individual liquid aerosol ($= 4\pi r^3/3$)

V_{a} : Volume of air mass in the simulation

V_{a0} : Initial value of V_{a}

w : Ascending speed of air

W : Water content of ice particles (ice water content)

α : Accommodation coefficient

Δa_{w} : Water activity of aqueous solution

Γ : Dry adiabatic lapse rate ($\equiv g/C_{\mathrm{p}}$)

λ : Correction factor used to calculate K_{n}

χ : Water vapor (volume) mixing ratio

χ_0 : Initial value of χ

θ : Potential temperature

θ_{e} : Equivalent potential temperature

ρ_{i} : Density of ice

Chapter 1

Introduction

1.1 Stratospheric water and the Tropical Tropopause Layer

Stratospheric water vapor plays an important role in climate change. *Solomon et al.* (2010) reported that 0.1 K out of 0.4 K of the global surface temperature increase during 1980 to 2010 owes the stratospheric water vapor increase (Fig. 1.1). They suggested the importance of taking the stratospheric water vapor change into account for the simulation of the future climate change.

Atmospheric transport from the troposphere to the stratosphere is one of the important processes regulating the stratospheric water vapor. *Brewer* (1949) found the extreme dryness of the stratosphere, and pointed out that such dryness is only realized by dehydration for the air mass on its passage through the cold tropical tropopause. Based on the idea, he introduced the picture of stratospheric general circulation: the tropospheric air enters the stratosphere through the tropical tropopause, and reaches the high-latitude stratosphere. *Dobson* (1956) described similar picture of the stratospheric circulation based on the global distribution of total ozone: the air in the tropical mid-stratosphere where the ozone is produced by photochemical processes advects to mid- and high latitudes with

a slow descent. The stratospheric general circulation introduced by Brewer and Dobson is now called Brewer-Dobson circulation. *Newell and Gould-Stewart* (1981) proposed the "stratospheric fountain" hypothesis in which the entry of tropospheric air must be restricted to the tropical western Pacific during boreal winter and the Bay of Bengal in summer. This hypothesis was generally accepted until *Sherwood* (2000) indicated that the vertical motion near the tropopause over the western Pacific is downward. *Danielsen* (1982) discussed the dehydration mechanism of deep convection that passes through the tropical tropopause and enters the stratosphere (over shoot). Evidence of the dehydration at tropical tropopause was shown from the observational data of stratospheric water vapor estimated by satellite. It was revealed that the water vapor mixing ratio in the lower stratosphere showed a striped pattern reflecting the slow ascent corresponding to the seasonal variation of the tropical tropopause temperature. This was called as an "atmospheric tape recorder" based on the idea that seasonal variation of saturation water vapor mixing ratio corresponding to the tropical tropopause temperature is recorded on the "tape", that is, the air entering the stratosphere (*Mote et al.*, 1996).

The understanding on the removal of water from the air entering the stratosphere changed drastically. *Highwood and Hoskins* (1998) shed light on the idea of the tropical tropopause layer (TTL) introduced by *Atticks and Robinson* (1983). They pointed out that the boundary between troposphere and stratosphere is not a well defined surface at which the physical and chemical quantities of air change discontinuously, but instead should be treated as a layer extending from around 200 hPa to 80 hPa. This layer is located above the main convective outflow, and the air lifted up by tropospheric deep convection to the TTL ascends diabatically through the TTL due to radiative heating. The transport of air in the TTL is dominated by fast quasi-isentropic horizontal advection. This slow ascent and fast horizontal advection characterize the motion of the air in the TTL. The introduction of the TTL inspired a novel idea on the dehydration processes in the tropical tropopause region. *Holton and Gettelman* (2001) proposed a new mechanism of dehydration with

the aid of a simple two-dimensional model, in which the air mass is dehydrated during the horizontal advection through the cold trap region in the western tropical Pacific. This hypothesis was further examined by *Hatsushika and Yamazaki* (2003) reproducing the cold trap in the General Circulation Model (GCM). From the simulations, they revealed that dehydration in the TTL is caused by both low temperature and a pair of anticyclonic circulation associated with the "Matsuno-Gill pattern" over the western tropical Pacific, and introduced three-dimensional picture of the TTL dehydration (Fig. 1.2). The air mass, trapped by a pair of subtropical anticyclones in the TTL, is dehydrated during the advection through the cold region before diabatically ascending into the stratosphere. This understanding, initiated from the proposal by *Holton and Gettelman* (2001), is now becoming widely accepted as a key dehydration process for tropospheric air entering the stratosphere.

Dehydration in the TTL goes on by ice nucleation associated with the cooling of air mass in the cold region. Nucleated ice particles are observed as cirrus clouds in the TTL, which contribute not only to the determination of stratospheric water vapor but also to the global climate by changing the radiation budget of atmosphere (*Hartmann et al.*, 2001). Therefore, it is important to understand the ice-nucleation process in the TTL and to represent it correctly in the GCM simulations.

The ice nucleation in the TTL is also important on the global climate change through aerosol-cloud interaction. The Fifth Assessment Report from Intergovernmental Panel on Climate Change (IPCC AR5) examined the variation of the aerosol characters (i.e., composition, number and size) , caused by human activities and climate change. It is found that the radiative forcing driven by cloud adjustments due to aerosols is -0.55 (-1.33 to -0.06) W m^{-2} among the total radiative forcing of 2.29 (1.13 to 3.33) W m^{-2} from 1750 to 2010. The ranges shown in parentheses are the uncertainties. The large uncertainty in aerosol-cloud interaction suggests that it is also important to investigate TTL ice nucleation on climate change.

In spite of these importances, however, the ice-nucleation process in the TTL including the effect of aerosol character variation is not fully understood owing to the difficulty of in situ observation due to extreme low temperature and high altitude condition. Hence, the processes of TTL ice nucleation, and thus the stratospheric water vapor change, are not well represented in the numerical model simulations of future climate change.

In the next section, we describe ice-nucleation processes as the basis of our study.

1.2 Ice nucleation

Dehydration processes in the TTL are interpreted as a series of cloud microphysical processes, that is, the ice nucleation in the supersaturated air mass due to low temperature, the water vapor absorption by the growth of nucleated ice particles, and the removal of ice particles from air mass by fall out (sedimentation). The aerosol particles having the potential for nucleating ice particles are called as effective ice nuclei. There are two kinds of nucleation processes of ice particles, namely, homogeneous nucleation and heterogeneous nucleation. The features of these processes are described in the following subsections.

1.2.1 Homogeneous ice nucleation

Homogeneous ice nucleation is the nucleation of ice particles with the freezing of liquid aerosols. Growth of aqueous aerosols due to absorption of water molecules on their surface is caused by the increase of saturation ratio along with the cooling of air. As a result, liquid aerosol is frozen due to the increase of freezing point associated with the depression of solution concentration. Liquid sulfuric acid particles are found in the Junge layer which is surrounding the Earth at the altitudes from a few kilometers above the tropopause (9 to 17 km) to mid-stratosphere (28 km). From laboratory experiments, *Koop et al.* (2000) confirmed that homogeneous ice nucleation of liquid aerosols occurs under extremely low temperature, and proposed a parameterization to calculate the number of ice particles

nucleated homogeneously. According to their formulation, the number of nucleated ice particles per unit time ($dN_{\rm i}/dt$) is proportional to the product of the volume of individual liquid aerosol V and its number N:

$$\frac{dN_{\rm i}}{dt} = J_{\rm c} NV. \tag{1.1}$$

The proportional coefficient, $J_{\rm c}$, is called the homogeneous nucleation rate coefficient. *Koop et al.* (2000) indicated that it depends not on the solute but only on the water activity $\Delta a_{\rm w}$ of liquid aerosols expressed by the following empirical formula:

$$J_{\rm c} = 10^{-906.7+8502(\Delta a_{\rm w})-26924(\Delta a_{\rm w})^2+29180(\Delta a_{\rm w})^3}. \tag{1.2}$$

Here, $\Delta a_{\rm w}$ is a functions of temperature T, partial pressure of water vapor $p_{\rm v}$, and saturation water vapor pressure $p_{\rm i}$:

$$\Delta a_{\rm w} = \exp\left\{\frac{131.438T^2 + T(210368 - 41729.1\ln T) - 3323730}{R^* T^2}\right\}\left(\frac{p_{\rm v}}{p_{\rm i}} - 1\right), \tag{1.3}$$

where R^* is the universal gas constant. The partial pressure of water could be expressed by $p_{\rm v} = \chi p$, where χ is volume mixing ratio of water and p is atmospheric pressure. The increase of $J_{\rm c}$ due to the decrease of T makes ice-nucleation rate $dN_{\rm i}/dt$ higher and initiates ice nucleation ($N_{\rm i} \geq 1$) when the ice saturation ratio $S = p_{\rm v}/p_{\rm i}$ (relative humidity over ice; $\mathrm{RH_i}$) exceeds the threshold value of $\sim$1.6 ($\sim$160 %). After the initiation, the number of nucleated ice particles increases rapidly because of the strong sensitivity of $J_{\rm c}$ to S. Because of the supersaturation, ice particles grow moment after nucleation, and supersaturation is dissolved gradually along with the nucleation and growth of ice particles (see Fig. 3.1 for the time evolution). *Koop et al.* (2000) defined the threshold saturation ratio for the initiation of homogeneous ice nucleation $S_{\rm c}$ as the saturation ratio under which $1/e$ of initial aerosols nucleate in a minute, and expressed as functions of aerosol radius

and air temperature (Fig. 1.3). This result indicates that $S_c \simeq 1.6$ in the TTL, and that it corresponds well to the observed ice saturation ratio in the cirrus clouds formed in the polar stratosphere. Homogeneous ice nucleation is considered as the major ice-nucleation process in the TTL because of the large population ($> 10^5$ L^{-1}) of liquid aerosols (*Brock et al.*, 1995; *Borrmann et al.*, 2010).

1.2.2 Heterogeneous ice nucleation

Importance of another type of ice-nucleation process, heterogeneous ice nucleation, is pointed out as the observations in the TTL are accumulated. Heterogeneous ice nucleation is the ice-nucleation process with the water vapor condensing on the surface of solid aerosols (*Lynch et al.*, 2002). There are various pathways in heterogeneous ice nucleation: for example, direct water-vapor condensation to solid aerosols, collision of a solid aerosol with a liquid aerosol (contact freezing nucleation), and coagulation of liquid phase on solidus phase in the mixed (including soluble and insoluble components) aerosols (immersion freezing nucleation) (*Pruppacher et al.*, 1998; *Lynch et al.*, 2002). In heterogeneous ice nucleation, solidus surface decreases the free energy of the aerosol surface and makes the occurrence of ice nucleation easier. Thus the threshold temperature of ice nucleation is lower than that of homogeneous ice nucleation. From the in situ air craft measurements, *Cziczo et al.* (2013) investigated the composition of residual particles after sublimation of ice particles of cirrus clouds. They found that the ingredients of sublimated ice particles are mainly mineral dust and metallic particles, and proposed the ice nucleation threshold of 1.1 to 1.4 in ice saturation assuming those act as effective ice nuclei. The threshold of heterogeneous ice nucleation depends on the composition of effective ice nuclei in strong contrast to that of homogeneous ice nucleation being determined by aerosol radius and temperature. The candidates of effective ice nuclei for heterogeneous ice nucleation are not only mineral dust and metallic particles but also sea salt and ammonium sulfate (*Baustian et al.*, 2010; *Wise et al.*, 2010; *Shibata et al.*, 2012; *Jensen et al.*, 2013b). The background

population of those nuclei in the TTL is estimated to be less than 10^2 L^{-1} (often less than 20 L^{-1}). However, knowledge about solid aerosols which act as effective ice nuclei is incomplete and simple parameterization like homogeneous ice nucleation is not available.

Following the accumulation of in situ observations, the microphysical properties of TTL cirrus become available. It was found that cirrus clouds with low ice-particle concentrations ($< 10^2$ L^{-1}) are widely distributed in the TTL (*Krämer et al.*, 2009). In view of the agreement between the number concentration of observed ice particles and that of candidates of effective ice nuclei, it is becoming generally accepted that heterogeneous processes play an important role in the TTL ice nucleation (*Krämer et al.*, 2009; *Jensen et al.*, 2010; *Shibata et al.*, 2012; *Jensen et al.*, 2013a).

1.3 Progress of understanding TTL ice nucleation

The processes contributing to the formation of the TTL cirrus was considered to be the cold trap dehydration (*Holton and Gettelman*, 2001) and cooling associated with synoptic disturbances such as equatorial Kelvin waves (e.g. *Fujiwara et al.*, 2009). Under the ascending speed of no more than 0.03–004 m s^{-1} (1.1–1.4 K h^{-1} in cooling rate) associated with those disturbances, relatively low ice concentration (≤ 300 L^{-1}) cirrus seems to be formed in the TTL (*Jensen et al.*, 2010). Temperature decrease during the ice nucleation is estimated as 0.18–0.23 K under the assumption of ∼10 minutes ice nucleation. However, temperature fluctuations in the TTL obtained from in situ aircraft measurements (*Jensen and Pfister*, 2004) indicate that those associated with high-frequency mesoscale disturbances such as gravity waves appear in the amplitude ≥ 1 K, and that high ice-concentration cirrus is formed due to fast ascending motion (typically ≥ 0.1 m s^{-1}) associated with mesoscale disturbances. *Jensen et al.* (2010) pointed out from microphysical model simulations with homogeneous ice nucleation that the cirrus with high ice concentration (10^3 L^{-1}) could be formed frequently under TTL conditions (Fig. 1.4) due to mesoscale disturbances such

as gravity waves. In those cirrus, supersaturation is dissolved within few tens of minutes because the high ice concentration, thus the large surface area, leads effective water vapor uptake by ice-particle growth. In contrast, persistent high supersaturation inside and outside cirrus in the TTL was reported from measurements by aircraft, radiosondes (e.g., *Marenco et al.*, 1998; *Spichtinger et al.*, 2003; *Shibata et al.*, 2007), with the accuracies on the order of 10% in water vapor. This mysterious supersaturation was called "supersaturation puzzle" (*Peter et al.*, 2006) and was intensely debated by *Krämer et al.* (2009) and *Jensen et al.* (2010). They investigated in situ observational data, and revealed that the ice concentrations were frequently extremely low (Figs. 1.5 and 1.6) ($< 10^2$ L^{-1}), as compared to those expected from TTL environment (10^3 L^{-1}). This result was consistent with other observational results such as those by *McFarquhar et al.* (2000), *Thomas et al.* (2002) and *Lawson et al.* (2008). In those low ice-concentration cirrus, the time scale to dissolve supersaturation was relatively long (about a few hours) which was consistent with persistent high supersaturation inside and outside the cirrus in the TTL. Thus, the "supersaturation puzzle" in the TTL has become a "nucleation puzzle" (*Spichtinger and Krämer*, 2013) concerning why low ice-concentration cirrus is frequently observed in the TTL even though its environment could potentially form high ice-concentration cirrus.

Influential hypotheses about "nucleation puzzle" have been proposed in two different perspectives: that of cloud microphysics and atmosphere dynamics. The former interprets the major ice-nucleation process as heterogeneous ice nucleation, and this process contributes to the formation of frequently observed low ice-concentration cirrus (e.g. *Krämer et al.*, 2009; *Jensen et al.*, 2010; *Shibata et al.*, 2012). Number concentration of solid aerosols, identified as effective ice nuclei for heterogeneous ice nucleation, is consistent with that of ice particles in the cirrus observed frequently in the TTL (*Krämer et al.*, 2009). Furthermore, it is suggested that homogeneous ice nucleation is possibly prevented by heterogeneous ice nucleation (*Jensen et al.*, 2010; *Spichtinger and Cziczo*, 2010) because heterogeneous ice nucleation is initiated at lower RH_i than homogeneous ice nucleation.

In fact, *Jensen et al.* (2013b) reported a typical low ice-concentration cirrus in which the supersaturation persisted because of the growth of heterogeneously nucleated ice particles.

The latter attributes the formation of low ice-concentration cirrus to high-frequency short waves. *Spichtinger and Krämer* (2013) pointed out that interruption of cooling, thus ice nucleation in about 0.5–3 minutes, could suppress the number concentration of ice particles nucleated by homogeneous ice nucleation. They conducted a series of numerical experiments simulating two scenarios for ice nucleation: one by homogeneous ice nucleation only, and the other by both heterogeneous and homogeneous ice nucleations simultaneously. In these experiments, they assumed that high-frequency monochromatic waves are superimposed on large-scale waves (i.e., equatorial Kelvin waves). Among the frequency distributions of ice-particle concentrations obtained by integrating experiments with various weighting factors, they sought the optimal combination of weights to reproduce the observed frequency distribution of ice particles (Fig. 1.6). The results indicated that 79% of observed ice-particle concentration was explained only by homogeneous ice nucleation in slow large-scale waves, $\sim$ 20% stemmed from combined heterogeneous and homogeneous ice nucleations in slow large-scale waves, and only $\sim$ 1% came from homogeneous ice nucleation with or without heterogeneous ice nucleation in fast large-scale waves. From these experiments, *Spichtinger and Krämer* (2013) pointed out the importance of homogeneous ice nucleation associated with high-frequency gravity waves superimposed on large-scale waves such as equatorial Kelvin waves.

1.4 Purpose of this study

Most of the previous studies of TTL ice nucleation summarized in Section 1.3 investigate statistical distribution of ice-particle concentrations comparing those from in situ observations and simulated by cloud microphysical models. This is due not only to the lack of in situ data in the TTL but also to the limited resolution and deficient accuracy of obser-

vational data. These studies will be useful to understand ice-nucleation processes widely taking place in the TTL. However, there is no guarantee that the observed ice particles were actually nucleated by the process that is most probable in a statistical sense. In fact, ice-particle concentration of the TTL cirrus is also affected by other factors such as sedimentation of ice particles (*Spichtinger and Gierens*, 2009), mixing and diffusion of air, and effect of pre-existing ice particles that survived from sublimation (*Shi et al.*, 2015). In addition, because the information about aerosol size distribution in the TTL is limited (*Jensen et al.*, 2013b), initial aerosol size distributions given in the numerical simulations (*Jensen et al.*, 2010; *Spichtinger and Krämer*, 2013) inevitably refer to those from aerosol models (*Kärcher and Lohmann*, 2002b; *Weisenstein et al.*, 2007).

To make a break through in TTL studies, Airborne Tropical Tropopause Experiment (ATTREX) observation campaigns (*Jensen et al.*, 2013b, 2017) were conducted. Figure 1.7 shows examples of observed profiles from ATTREX2011 (*Jensen et al.*, 2013b) describing the detailed structure of TTL cirrus at the altitudes where ice-particle concentration (red) is high. In profiles A and B, relatively thick cirrus is observed, while thin ($\sim$ 20 m) cirrus with high ice-particle concentration (10^4 L^{-1}) is observed in profile C. Such a thin structure and a high concentration of ice particles with small radius suggest that this cirrus is observed soon after nucleation. Furthermore, ice-particle concentration of 10^4 L^{-1} could be only realized by homogeneous ice nucleation. These features are ideal for a detailed study on the microphysical processes of the TTL cirrus. Our focus on this particular example constitutes a strong contrast to previous studies concerned mainly on the statistics of TTL cirrus. It is true that sticking to just one example could end up as a case study. However, the rareness of observation frequency does not always mean that such an example is negligible. In our opinion, an idealized example could eliminate minor details and help open the door leading to the general understanding about the formation process of TTL cirrus.

The present study focuses on the high ice-concentration thin TTL cirrus introduced

in Fig. 1.7 (C) making it possible to assume that the cirrus is formed by homogeneous ice nucleation and observed a moment after nucleation without affected by sedimentation, mixing, and diffusion. Major science questions of this study are as follows:

1. How can the microphysical properties of aerosols, such as radius and number concentration, and external conditions, such as water mixing ratio and cooling rate, affect the TTL cirrus?

2. How can we understand the interaction of aerosols with different size in ice nucleation?

The results are discussed trying to draw useful implications that may lead to the general understanding about the formation process of the TTL cirrus.

The remainder of this paper is organized as follows. In Chapter 2, some attempts on the estimation of the microphysical properties of TTL cirrus are introduced. In Chapter 3, we describe the microphysical conditions necessary for the formation of the observed cirrus under the assumption of monodisperse aerosol distribution after a brief introduction of the microphysical cloud model used in this study. Bimodal distribution of aerosols is introduced in Chapter 4 focussing on the effect of aerosol interactions. Required conditions for the formation of observed cirrus is discussed in Chapter 5. Finally, Chapter 6 concludes the findings.

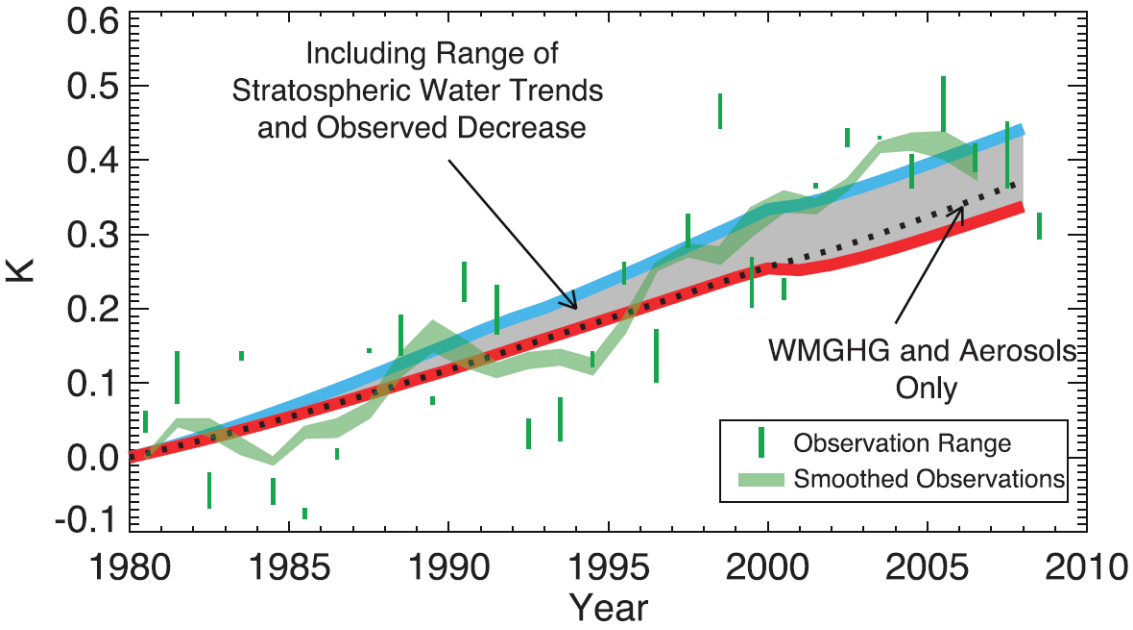

Figure 1.1: Time series of the measured and modeled temperature changes relative to 1980 (*Solomon et al.*, 2010). The former is obtained from three different observed global temperature records with the green markers indicating the range across the three data sets in each year, and the green shaded line shows range of the 5-year running mean of the three data sets. The later is calculated by taking well-mixed greenhouse gases and aerosols (dot line), plus temperature variation due to stratospheric water vapor changes (red: stepwise decrease in 2000–2001 is only considered, and blue: stratospheric water vapor trend of 0.5 ppmv per decade is included) into account.

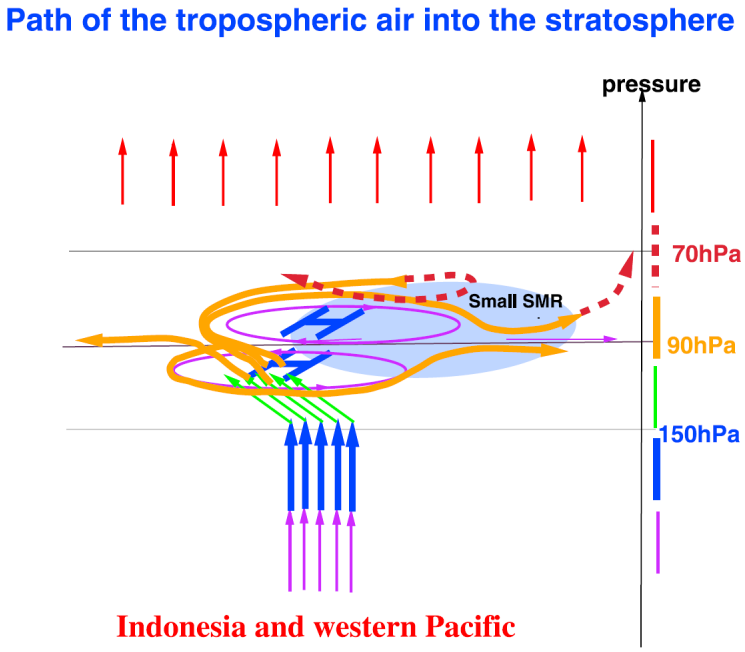

Figure 1.2: Schematic picture for the path of the air from the troposphere to the stratosphere through the tropical tropopause layer (*Hatsushika and Yamazaki*, 2003). The color of each line denotes the pressure level, and the shaded area corresponds to the minimum SMR (cold) region. The anticyclones around the tropopause are also drawn with purple lines.

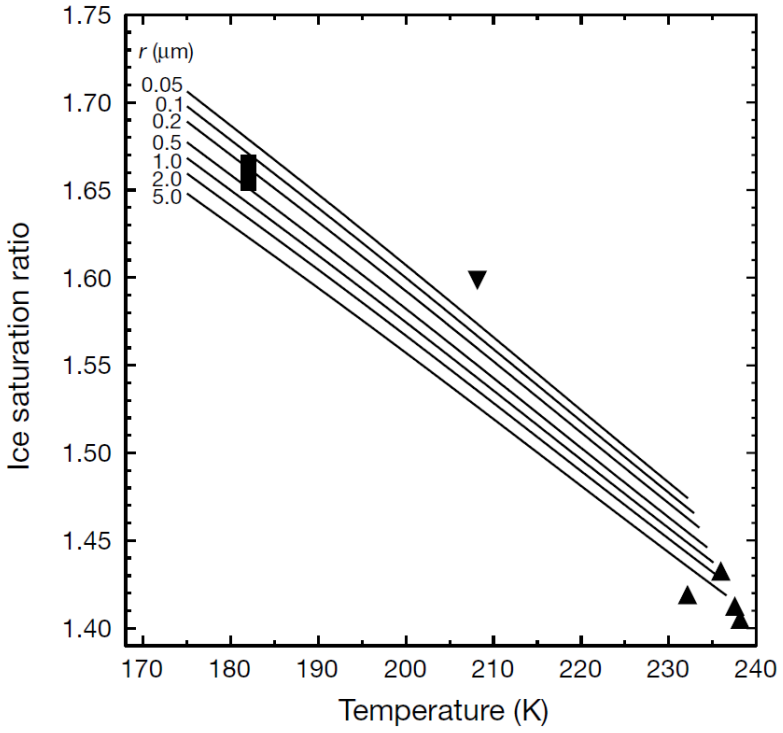

Figure 1.3: Ice saturation ratios for different aerosol radii as a function of temperature. Upward triangles indicate observations of liquid water droplets with the lidar technique and in situ measurements of ice saturation ratio in cirrus clouds at about 8 km altitude. Downward triangles indicate an upper limit for ice saturation ratio at 208 K from an in situ measurement of an orographically induced ice cloud at about 12 km altitude. Rectangles indicate lidar observations of a polar stratospheric ice cloud at an altitude of about 22 km at 182 K evaluated by means of a mesoscale microphysical box model together with light scattering calculations to simulate the observed lidar images along the quasi-lagrangian trajectory of the cloud particles (*Koop et al.*, 2000).

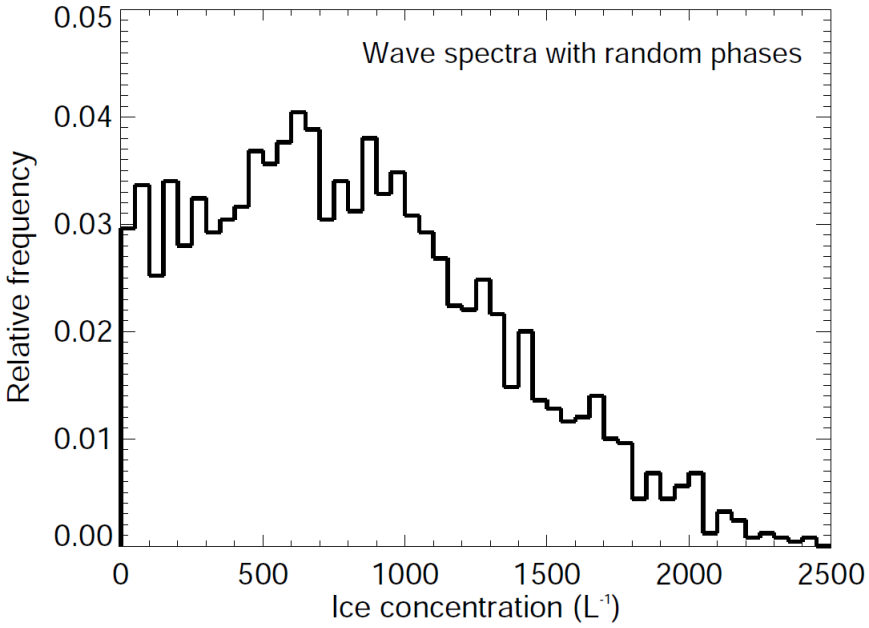

Figure 1.4: The frequency distribution of the maximum ice concentrations from a large number of parcel model simulations with spectra of waves (*Jensen and Pfister*, 2004) superimposed on slow cooling under the TTL environment. In each simulation, a different seed was used for the random number generation of phase offsets for each wave frequency in the spectrum (*Jensen et al.*, 2010).

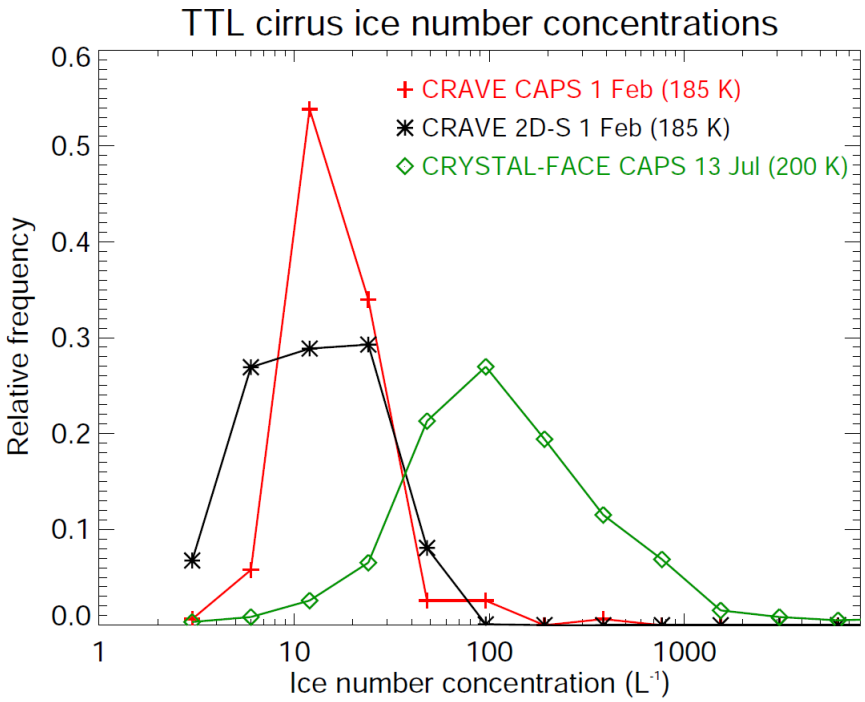

Figure 1.5: Red and black curves show ice-particle concentration frequency distributions observed by two different instruments, simultaneously, in very cold TTL cirrus sampled during the Costa Rica Aura Validation Experiment (CR-AVE) mission (*Lawson et al.*, 2008). Ice-particle concentrations in these clouds were almost exclusively less than 10^2 L^{-1}. The green curve shows the ice-praticle concentration frequency distribution from a warmer tropopause cirrus layer sampled during CRYSTAL-FACE (*Jensen et al.*, 2005) with larger ice concentrations predominating.

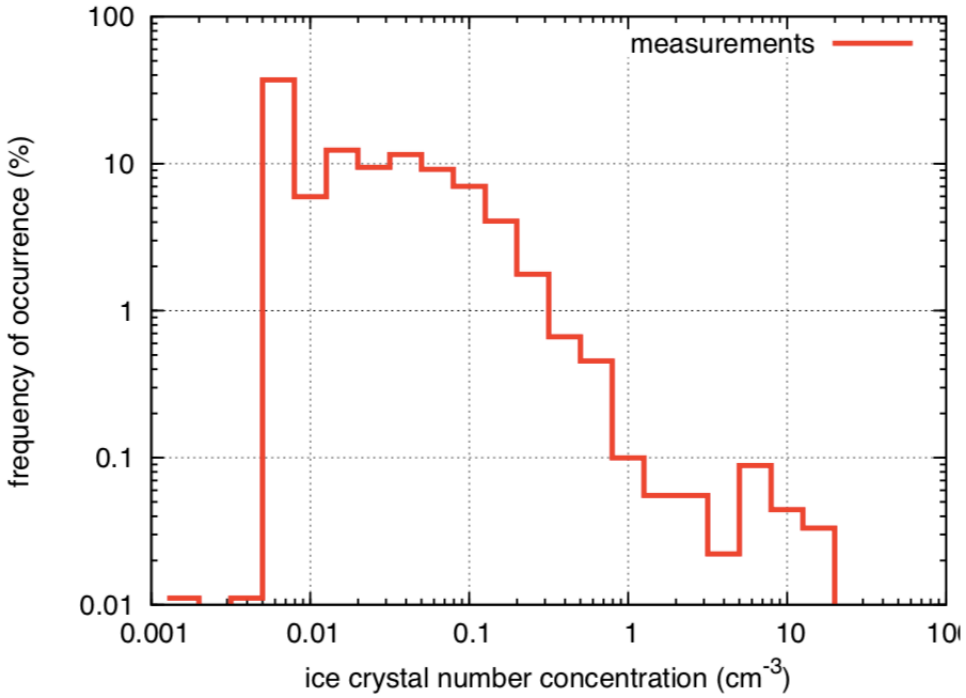

Figure 1.6: Measured ice-particle concentration distribution in near the TTL region over the western Indian Ocean, and eastern and western Pacific with the temperature range $T < 200$ K (*Spichtinger and Krämer*, 2013), achieved from aircraft, balloon and ground-based observations (*Krämer et al.*, 2009). As for the Fig. 1.5, observed frequency is highest where ice-particle concentration is less than 10^2 L^{-1} (0.1 cm^{-3}), decreases where ice-particle concentration is more than 10^2 L, and concludes to around 0.1 % where ice-particle concentration is more than 10^3 L^{-1} (1 cm^{-3}).

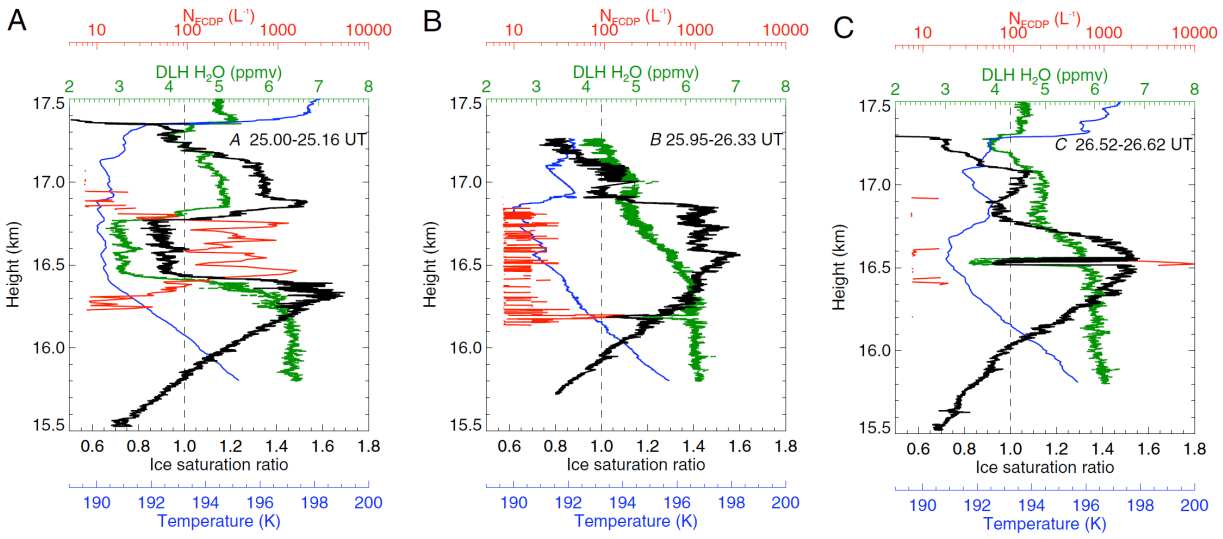

Figure 1.7: The vertical profiles of typical cirrus clouds observed in ATTREX2011 during the slow ascent or descent across the cirrus. Ice-particle concentration (red; L^{-1}), water vapor mixing ratio (green; ppmv), ice saturation ratio (black), and temperature (blue; K) are shown (*Jensen et al.*, 2013b).

Chapter 2

Estimation of the microphysical properties of TTL cirrus

Microphysical properties of the TTL cirrus such as the size distribution of ice particles have been observed mainly by in situ aircraft measurements and simultaneous observations of radiosondes and ground-based lidars. In this chapter, some results on the estimated microphysical properties of the TTL cirrus are introduced as a basis of our understanding on the ice-nucleation processes in the TTL.

2.1 Estimation of microphysical properties

Heymsfield (1986) reported that the ice concentrations of stratiform ice clouds observed by aircraft at the altitude of 16.2–16.7 km over the equator were at least 50 L^{-1} with the radius ranging from 2 (minimum detectable size) to 25 μm. *Thomas et al.* (2002) reported on optically thin (subvisible) cirrus clouds formed under an extremely cold condition (< 190 K) around 17 km over the tropics from in situ aircraft observations over the ITCZ in the Indian Ocean. The observed cirrus had the horizontal and the vertical scales of several hundred kilometers and 100–400 m, respectively, and the life time was at least 3 hours.

The size distribution of ice particles observed from inside and outside of the cirrus ranged from 0.2 to 11.5 μm in radius, and most of the ice particles inside the cirrus had the radius of about 5 μm. They mentioned, however, the possible existence of larger ice particles, as the maximum detectable radius of the instrument was 11.5 μm. *Peter et al.* (2003) reported that the ice-particle concentrations were extremely low (5–10 L^{-1}) with the radius of about 5–6 μm for subvisible cirrus layers measured just below the tropical tropopause. *Jensen et al.* (2005) analyzed the microphysical properties of the subvisible tropopause cirrus clouds, supposed to be similar to the TTL cirrus, over Florida in summer 2002. They found that the radius of ice particles in the cloud layer were ranging from 3.5 to 25 μm, and that the mode radius was about 10–25 μm. It was also reported that the cirrus layer was supersaturated with the relative humidity over ice (RH_i) of 1.2–1.3. Extensive sampling of very cold (188–198 K) subvisible cirrus over the tropical (0–10° N) eastern Pacific was made from the Costa Rica Aura Validation Experiment (CRAVE) campaign (*Lawson et al.*, 2008). It was found that the mean ice-particle concentration was 66 L^{-1} and that 84% of the observed ice particles was quasi spherical while large particles with the radius greater than 32.5 μm exhibited disk-shaped hexagonal plates. *Krämer et al.* (2009) examined the data set obtained from 28 aircraft flight observations over the tropical, mid-latitude and polar regions in order to confirm the supersaturation over ice in the cold (air temperature below 205 K) cirrus. They revealed that the supersaturation didn't exceed the homogeneous nucleation threshold in the cold cirrus and suggested that the water vapor uptake by ice growth did not proceed appreciably because the observed ice-particle concentration were much lower than that presumable from homogeneous nucleation. They suggested the contribution of heterogeneous nucleation as a possible explanation for the observed low concentration of ice particles.

Iwasaki et al. (2007) investigated the size distributions of ice particles and aerosols in the TTL, defined as the height range in which the temperature was lower than 198 K, using the simultaneous observations of the optical particle counter (OPC) and ground-

based lidar at Thailand in April 2003. They found that the mode radius of ice particles was less than 10 μm and that the number concentration of large particles having the radius greater than 0.8 μm was greater in the cirrus clouds, although the particle size distribution in the radius of less than 0.8 μm was similar between inside and outside of the cirrus cloud. This result suggests that the liquid aerosols with the radius greater than 0.8 μm was frozen. *Shibata et al.* (2012) analyzed the OPC and ground-based lidar data simultaneously obtained at Biak, Indonesia in January 2011. They found that the number concentration of the particles observed by the OPC, equipped with a thermodenuder to measure nonvolatile (solid) particles only, agreed with that of the ice particles of the cirrus (50–100 L^{-1}) estimated by the lidar observation. This result suggests that the heterogeneous nucleation is important in the TTL cirrus formation.

Microphysical properties of TTL cirrus are thus evaluated by various observational and analysis methods. Various aspects and statistical features of TTL cirrus have been accumulated by aircraft observations taking the advantages of the mobility, the flexibility of flight route, and the wide coverage of observation area. However, aircraft observations in the TTL have been limited because of its high altitude and extreme low temperature. In particular, TTL observations over the western Pacific in the boreal winter have not been conducted despite its importance in the dehydration of air entering the stratosphere. In addition, the problems such as the possible breaking of ice particles into pieces and insufficient data resolution due to the high-speed cruising of aircraft are pointed out on airborne in situ measurements of cirrus microphysical properties (*Field et al.*, 2003; *McFarquhar et al.*, 2007; *Jensen et al.*, 2009; *Korolev et al.*, 2013). On the other hand, the vertical profiles of cirrus have been obtained from balloon-borne measurements with relatively high resolution and precision, and the time evolutions of the cirrus as an Eulerian view over the observation site are described by lidar observations (*Iwasaki et al.*, 2007; *Fujiwara et al.*, 2010; *Shibata et al.*, 2012; *Hasebe et al.*, 2013; *Inai et al.*, 2013), although the number of sampled cirrus has remained small because the cirrus is not always present

over a field station. A new instrument, Cloud Particle Sensor (CPS; *Fujiwara et al.*, 2016), is becoming available to measure microphysical properties of cirrus, although very few in situ measurements of the cirrus have been conducted so far.

2.2 Knowledge obtained from ATTREX campaigns

ATTREX started in fall 2011 over the eastern tropical Pacific (ATTREX2011) and continued until 2015 with an extended coverage over the whole Pacific (*Jensen et al.*, 2013c, 2017) with the following purposes.

1. To make progress in the understanding on how the physical processes in the TTL (cloud microphysics, large scale air uplift, deep convection and wave activities) control the water vapor and chemical composition of the air mass entering the stratosphere.

2. To provide high-resolution dataset of the TTL physical composition for representing physical processes (cirrus, water vapor and ozone variability) necessary to incorporate in global models for future climate change.

In the ATTREX campaign, NASA Global Hawk Unmanned Aircraft System with the ceiling at ∼20 km in long duration (30 hours), ideal for sampling the TTL, was introduced for the first time. After reaching the observation area in the TTL, the aircraft flew up and down across the TTL cirrus slowly with the vertical speed of ∼2 m s^{-1} and obtained the high-resolution profiles of various quantities with the vertical resolution of a few meters. High-resolution profiles of TTL cirrus from ATTREX made it possible to discuss the details about TTL cirrus formation and revealed unprecedented features on the TTL cirrus (*Jensen et al.*, 2013b; *Ueyama et al.*, 2014).

Among the equipped instruments and observed parameters in ATTREX2011, those used in this study are shown in Table 2.1. The flight paths (latitude, longitude and height)

were retrieved by Global Positioning System (GPS). Temperature, pressure and wind velocities were observed by Meteorological Measurement System (MMS). Primary data of temperature and pressure were calibrated to static values by using wind speed to remove the influence of high-speed cruising aircraft. Water vapor mixing ratio was obtained from Diode Laser Hygrometer (DLH), a near-infrared external open-path diode laser spectrometer, to provide precise (precision of 50 ppbv for 20-Hz measurements) data. In ATTREX campaign, Fast Cloud Droplet Probe (FCDP) (Fig. 2.1) was introduced to measure the ice-particle concentration for the first time. FCDP was a laser spectrometer measuring the forward Mie scattering from ice particles. The size distribution of ice particles was obtained in 19 bins ranging from 0.5 to 25 μm in radius.

Typical examples of TTL cirrus observed ATTREX2011 was shown in Fig. 1.7. Cirrus was observed at the altitude of 16–17 km in all profiles (A, B, C). These cirrus clouds were considered to be formed in the TTL, since the analysis of geostationary satellite data combined with backward kinematic trajectories found no deep convection having reached to the altitude of 15 km. *Jensen et al.* (2013b) categorized these cirrus clouds into two distinct classes referring to the ice-particle concentrations.

1. High ice-particle concentration cirrus (profiles A and C):

   Cirrus clouds with ice-particle concentration of 10^3–10^4 L^{-1} are seen at the altitude around 16.5 km. The thickness of the cirrus is about 500 m at the altitude of 16.3–16.8 km in profile A, while it is only about 20 m at 16.5 km in profile C. In both profiles, RH_i decreases to 1.0 inside the cirrus suggesting that the high ice-particle concentration, and thus the large surface area, contributed to deplete the water vapor effectively to dissolve the supersaturation quickly. The ice-particle concentrations of 10^3–10^4 L^{-1} indicate that these cirrus clouds were formed homogeneously because that of heterogeneous ice nuclei is much smaller ($< 10^2$ L^{-1}).

2. Low ice-particle concentration cirrus (profile B):

Low ice-particle concentration (20–30 L^{-1}) cirrus is found at the altitude of 16.1–16.7 km. At the altitude around 16.2 km, we can see a thin cirrus with relatively high ice concentration (2×10^2 L^{-1}) and RH_i of 1.0. These features suggest that the water vapor has been depleted in a short period of time due to high-concentration ice particles. In contrast, supersaturation persists in the surrounding cirrus layer (with the radius of ice particles ranging 30–50 μm and possibly larger). It indicates that the water vapor depletion by ice growth has not completed in this layer because the time scale to dissolve the supersaturation under the low ice-concentration condition is estimated to be several hours. It should be pointed out that the maximum value of RH_i in this cirrus layer is high ($\sim$1.6) but never exceed the homogeneous nucleation threshold. *Jensen et al.* (2013b), mentioning that the ice-particle concentration of 20–30 L^{-1} corresponds to the particle concentration of heterogeneous ice nuclei (insoluble particles), suggests that homogeneous nucleation might have been prevented under low-concentration ice particles possibly nucleated by heterogeneous nucleation.

2.3 Indirect estimation of microphysical properties

Jensen et al. (2013b) discussed the nucleation processes of the observed cirrus by focusing on its ice-particle concentration. The size distribution of ice particles is available from ATTREX2011, however, has not been fully analyzed. During the ATTREX2011, the ice-particle concentration was observed by distinguishing the size range with the vertical resolution of a few meters. The size distribution is useful for more detailed discussion about observed cirrus formation processes. In this section, high resolution dataset of ATTREX2011 are analyzed to discuss detailed formation processes of the observed high ice-particle concentration cirrus, presumably nucleated by homogeneous nucleation (*Koop et al.*, 2000), by using the observed microphysical properties.

Shibata et al. (2007) estimated the ice-particle radius of TTL cirrus using the ice water

content (W) obtained from balloon-borne Cryogenic Frost point Hygrometer (CFH) sondes and ground-based lidar at Bandung, Indonesia. Figure 2.2 shows the profiles of water vapor mixing ratio and RH_i obtained by CFH (left), and those of backscattering coefficient and ice-particle concentration obtained from a ground based lidar (right). Ice-particle concentration was estimated by assuming that the radius of ice particles is 5 μm. At the altitude of 17–18 km, RH_i takes the maximum value of 152 % with some decreases (shade) at 17.1–17.6 km. *Shibata et al.* (2007) assumed that the homogeneous nucleation took place at the shaded altitude range at the nucleation threshold of 152 % in RH_i and that the water vapor, corresponding to the shade, was taken up by ice growth by referring to the agreement between the altitudes of observed cirrus and RH_i decrease, and to the observed RH_i close to the homogeneous nucleation threshold (*Koop et al.*, 2000). Under these assumptions, they estimated the radius of ice particles in the cirrus based on the theoretical correspondence between the value of W divided by backscattering coefficient and the ice-particle radius, and concluded that the radius of ice particles distributed in the range of 4–30 μm.

In ATTREX2011, the size distribution of ice particles were obtained in addition to their concentration and water vapor mixing ratio. This dataset could be used to calculate the W and thus, to estimate the critical value of RH_i for ice nucleation: S_c (homogeneous nucleation threshold) by putting the following three assumptions:

1. The nucleation and growth of ice particles took place at the altitude where they were observed, and the W corresponds to the amount of water vapor decreased from that when RH_i is equal to S_c.

2. The atmospheric condition remains the same after ice nucleation.

3. All ice particles are spherical.

The size distribution of ice particles, represented by the ice-particle concentrations n_{ij} at j-th bin with the mean radius of $\bar{r_{ij}}$, are used together with air temperature T, pressure

p, and water vapor mixing ratio χ in order to estimate $S_{\rm c}$. Ice saturation ratio S is the ratio of water vapor pressure of air $p_{\rm v}(=\chi p)$ against the saturation water vapor pressure $p_{\rm i}$ defined as a function of T:

$$S = \frac{p_{\rm v}}{p_{\rm i}}. \tag{2.1}$$

$S_{\rm c}$ is estimated as follows: $W = \sum_j 4\pi \bar{r_{{\rm i}j}}^3 n_{{\rm i}j}\rho_{\rm i}/3$, where $\rho_{\rm i}$ is the density of ice, is converted to water vapor pressure $p_{\rm iwc}$ by using the equation of state, $p_{\rm iwc} = WR^*T/M_{\rm w}$, where $M_{\rm w}$ and R^* are the molecular weight of water and the molar gas constant, respectively. The water vapor pressure $p_{\rm c}$ at which the ice nucleation is initiated is the sum of $p_{\rm iwc}$ and $p_{\rm v}$. Then $S_{\rm c}$ is

$$S_{\rm c} = \frac{p_{\rm c}}{p_{\rm i}} = \frac{p_{\rm v} + p_{\rm iwc}}{p_{\rm i}}. \tag{2.2}$$

In this study, $p_{\rm i}$ is calculated from Goff-Gratch equation (*Goff*, 1946). Hereafter, 1-Hz frequency data, available from NASA ESPO Data Archive[1], are used rather than the original data taken at the frequency of 20 Hz.

Figure 2.3 shows the vertical profile of $S_{\rm c}$ (green dots in the left panel) thus estimated corresponding to the cirrus shown in Fig. 1.7(A). Black line in the left panel shows the observed ice saturation ratio S and the bars in purple are the confidence intervals of $S_{\rm c}$ estimated by calculating W corresponding to the maximum and the minimum value of $r_{{\rm i}j}$ in each bin. We can see the estimated $S_{\rm c}$ (green dot) is less than the homogeneous nucleation threshold ($\sim$ 1.6–1.7) in the upper part (altitude range of 16.63–16.89 km) while it is greater than the threshold in the lower part (16.37–16.63 km) of the cirrus. The right hand panel of Fig. 2.3 shows the size distribution of the observed ice particles. The results are presented by integrating in three layers indicated by the base-lines of the histogram in the cirrus. Here, the upper boundary of the cirrus layer (black horizontal line) is defined by the altitude where the water vapor mixing ratio takes maximum (5.17 ppmv) in the upper part of the cirrus. The size distribution appears similar in the upper

[1]https://espoarchive.nasa.gov/archive/browse/attrex

(blue) and the middle (green) layers. However, they are distinct in the existence of large particles with the radius ≥ 11.2 μm. In the bottom part of the cirrus (orange), the large particles are also found while small-size particles almost disappear. These results indicate that this cirrus is affected by sedimentation of ice particles and that it does not satisfy the assumptions for S_{c} estimation mentioned above.

Similar consideration is made for the thin cirrus shown in Fig. 1.7(C). In contrast to the cirrus shown in Fig. 1.7(A), the thin structure suggests that the dynamical processes such as sedimentation, diffusion and mixing have not yet taken place, and thus suitable for the evaluation of S_{c}. The results are shown in Fig. 2.4. In the cirrus layer with high ice-particle concentration, all ice particles are found in the bin of 0.5–1.6 μm in radius (green; the minimum detectable size), suggesting that the effect of sedimentation could be neglected. Even in this ideal case, however, the estimated value of S_{c} in the cirrus doesn't reach the threshold of homogeneous nucleation (1.6–1.7). This disagreement is not resolved by taking the uncertainties in the observed cloud microphysical properties (concentration and size of ice particles) and water vapor mixing ratio into account. In order to make the estimated S_{c} fit for the homogeneous nucleation threshold, either $n_{\mathrm{i}} \geq 6{\times}10^4$ L^{-1} or $r_{\mathrm{i}} \geq 2.0$ μm is required if the observed radius or concentration, respectively, of ice particles is correct.

The discussion about the cirrus formation trying to identify the atmospheric environment at the time of the initiation of ice nucleation is not easy. As was mentioned above, however, the thin cirrus shown in Fig. 1.7(C) is ideal for the investigation of formation process of TTL cirrus. In the next chapter, the formation of high ice-particle concentration cirrus shown in Fig. 1.7(C) is investigated with the aid of a cloud microphysical model assuming the homogeneous ice nucleation.

Table 2.1: The instruments, observed parameters, with their precision and accuracy used in this study (*Jensen et al.*, 2013b).

instrument	parameter	precision	accuracy
MMS	temperature	unknown	±0.3 K
	pressure	unknown	±0.3 hPa
	3D winds	unknown	±1.0 m
DLH	water vapor mixing ratio	50 ppbv	5%
FCDP	number concentration and size of ice particles	10%	unknown

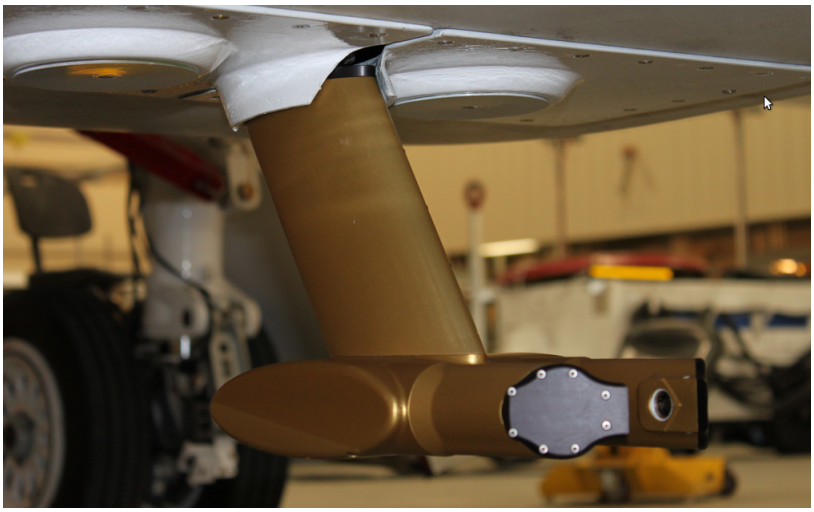

Figure 2.1: Fast Cloud Droplet Probe (FCDP) for measurement of the number concentration and size of ice particles. Laser spectrometer mounted on the tip of the arm (center of the picture) measures the forward Mie scattering from ice particles. Taken from https://espo.nasa.gov/home/sites/default/files/images/IMG_0772.JPG.

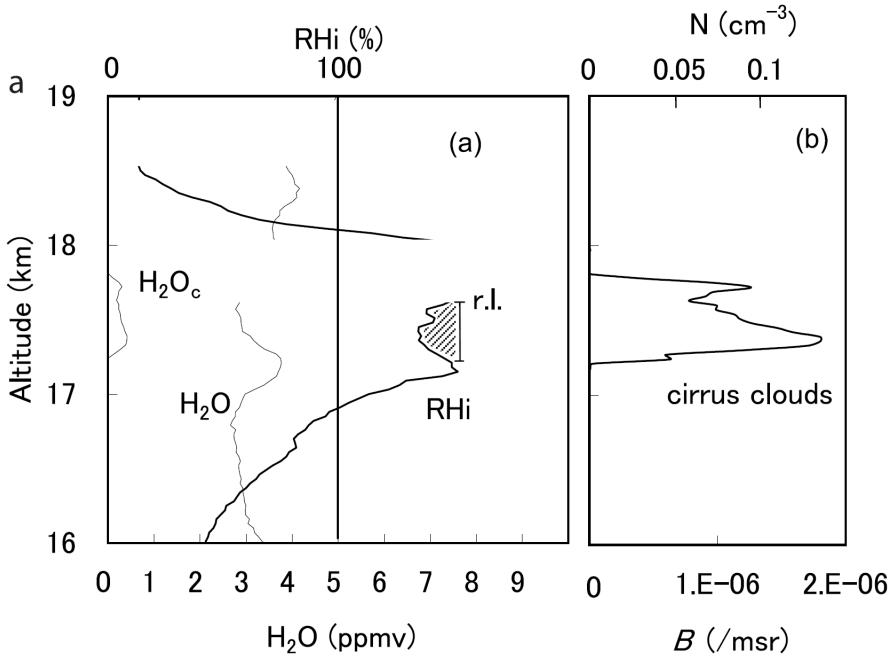

Figure 2.2: Profiles of (left) water vapor mixing ratio (thin solid line; lower axis) and relative humidity over ice (RH_i; thick solid; upper axis) obtained from Cryogenic Frost point Hygrometer (CFH) sondes, (right) ice-particle concentration (upper axis) estimated from backscattering coefficient (lower axis) observed by a ground-based lidar at Bandung, Indonesia. Shade area shows the amount of water having been depleted to form cirrus clouds (*Shibata et al.*, 2007).

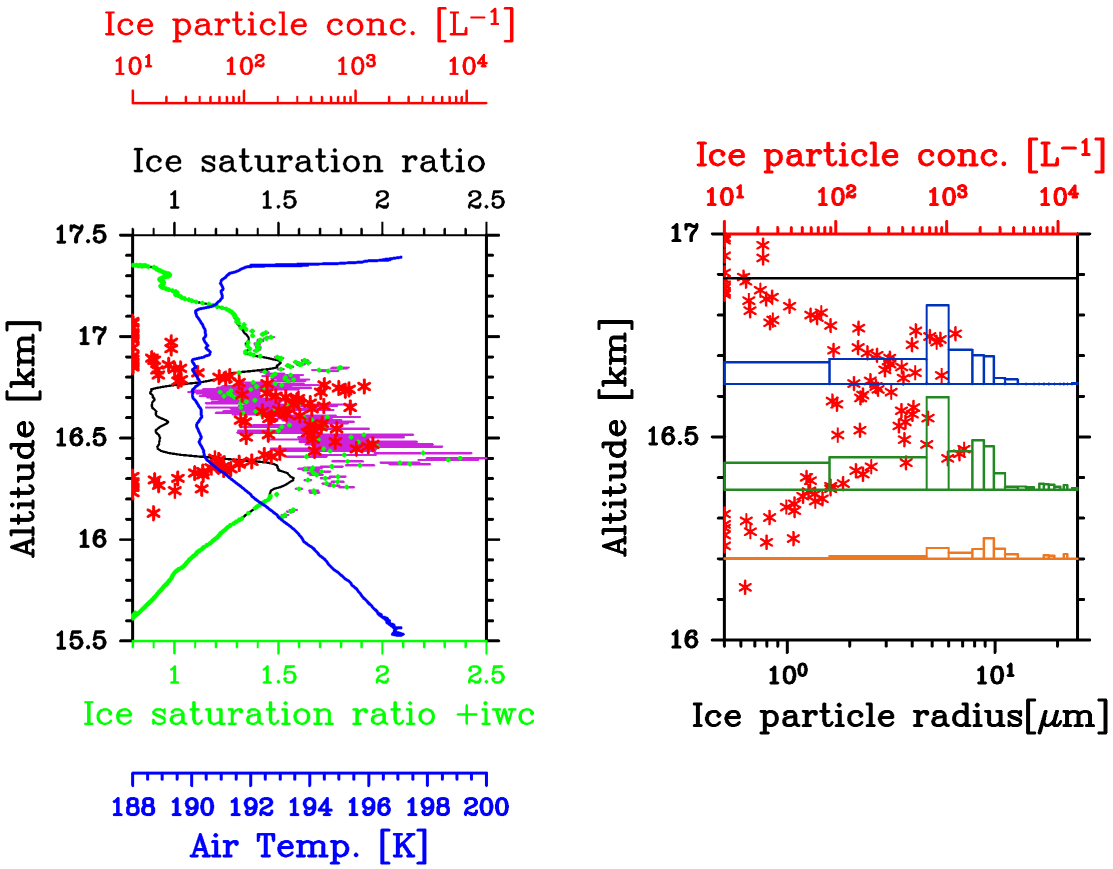

Figure 2.3: Profiles of homogeneous nucleation threshold (green) and its confidence interval (purple) estimated from observed ice-particle concentration (red), temperature (blue), and saturation ratio (black) shown in Fig. 1.7(A) in the left panel. The right panel shows the size distributions of ice particles integrated in the layer bounded by the base line of each histogram. The upper boundary of the cirrus (black horizontal line) is defined as the altitude at which the water mixing ratio takes maximum in the upper part of the cirrus. The areas of each rectangle correspond to the magnitude of ice-particle concentration on each bin.

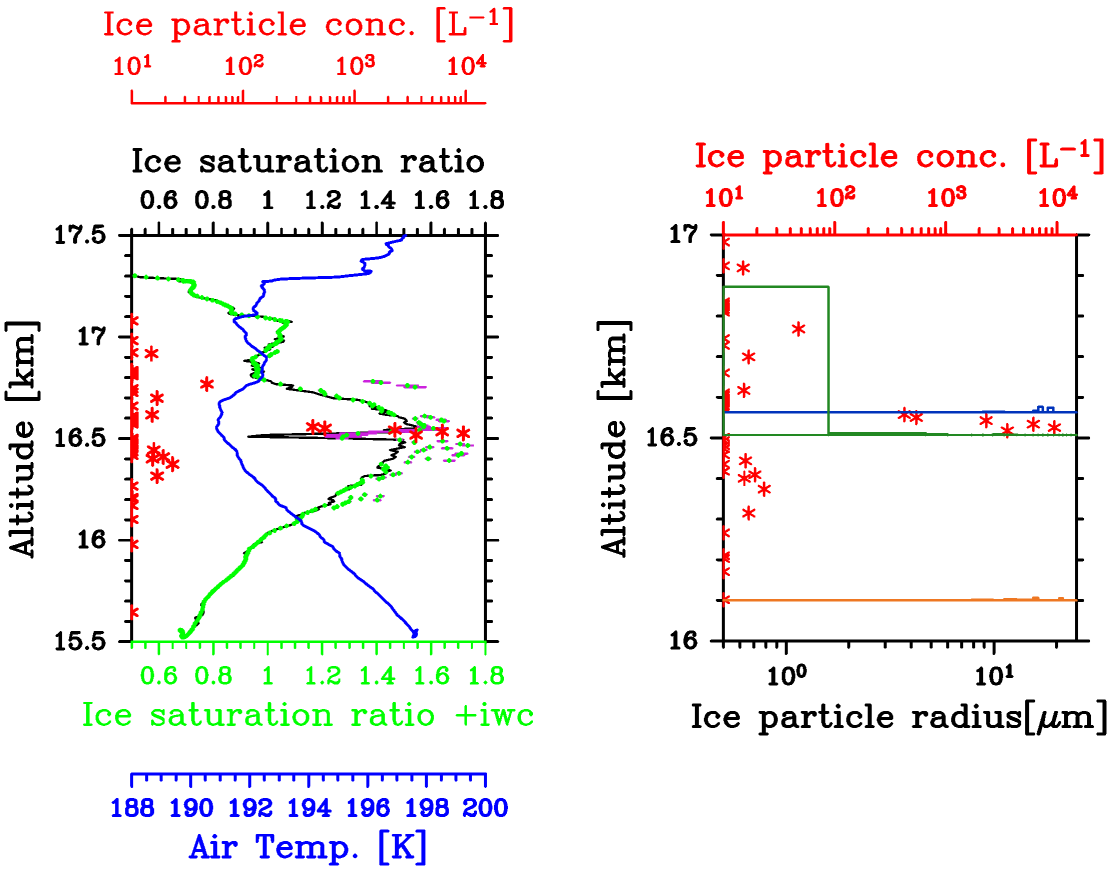

Figure 2.4: Same as Fig. 2.3 but for the case of Fig. 1.7(C). Note the change of axes from Fig. 2.3.

Chapter 3

Simulations with monodisperse aerosols

This study focuses on the thin cirrus shown in Fig. 1.7(C) composed of high concentration (10^4 L^{-1}) small ice particles. Since 10^4 L^{-1} would be an implausible concentration of heterogeneous ice nuclei, it is possible to assume that the ice particles were formed by homogeneous nucleation. The small size of the ice particles suggests that the particles were observed a moment after nucleation (Chapter 2). In this Chapter, the formation process of ice particles is investigated by using a cloud microphysical model assuming monodisperse aerosol particles as a first step. Interaction between aerosols with different radius will be discussed in the next Chapter by assuming aerosols of bimodal size distribution.

Kärcher and Lohmann (2002a,b) studied the dependency of the concentration of nucleating ice particles on frost-point temperature and cooling rate of air to parameterize homogeneous ice nucleation in the General Circulation Models. In the present study, initial water vapor mixing ratio χ_0 is introduced in place of the frost-point temperature in order to make a direct comparison with ATTREX profiles possible. Thus cooling rate of air, $-dT/dt = -\dot{T}$, χ_0, radius of monodisperse aerosol r and accommodation coefficient α are taken as sweeping parameters. Here, α represents the ratio of the number of captured

water molecules to that of collided water molecules in one ice particle. A series of parameter sweep experiments are carried out under the assumption of adiabatic ascent intending to simulate the meteorological process of the TTL ice nucleation to derive the maximum values of nucleating ice-particle concentration $n_{\mathrm{i}}^{\mathrm{max}}$. The validity of this assumption is confirmed by the fact that $\theta_{\mathrm{e}}/\theta - 1 \simeq \exp(L_{\mathrm{c}} q_{\mathrm{s}}/C_{\mathrm{p}}T) - 1 = O(10^{-5})$, where θ, θ_{e}, L_{c} and q_{s} are the potential temperature, equivalent potential temperature, latent heat of condensation (at 0°C), and saturation mixing ratio, respectively. The dynamical conditions necessary for the formation of TTL cirrus with an ice concentration of 10^4 L^{-1} is investigated by comparing $n_{\mathrm{i}}^{\mathrm{max}}$ and the observed value (10^4 L^{-1}) taking the uncertainty of α into account.

The microphysical model is explained in Section 3.1, showing time series of microphysical quantities for a simulation that leads to $n_{\mathrm{i}}^{\mathrm{max}} = 10^4$ L^{-1}. Then the dependencies of $n_{\mathrm{i}}^{\mathrm{max}}$ and size distribution of ice particles are examined as functions of $-\dot{T}$, r, χ_0, and α by conducting a series of parameter sweep experiments.

3.1 Descriptions on the model and settings

This study uses the microphysical box model employing the parcel method. The model, modified from the microphysical model developed at Nagoya University (*Daneva and Shibata*, 2001; *Maruwaka*, 2009; *Sakurai and Shibata*, 2012) following *Jensen and Pfister* (2004), describes the nucleation and growth of ice particles in the mass of air with the temperature T, pressure p, and volume V_{a}, following the supersaturation associated with adiabatic ascent. These variables satisfy the ideal gas law:

$$pV_{\mathrm{a}} = n_{\mathrm{a}} R^* T, \tag{3.1}$$

where n_{a} is the number of moles (amount of substance) of the air and R^* is a universal gas constant. n_{a} is a conserved quantity and is obtained by the initial conditions of temperature

pressure, and volume of air ($T_0,\ p_0$, and $V_{\mathrm{a}0}$) as follows:

$$n_{\mathrm{a}} = \frac{p_0 V_{\mathrm{a}0}}{R^* T_0}. \tag{3.2}$$

Because of the adiabatic constraint,

$$\theta = T \left(\frac{p_{\mathrm{s}}}{p} \right)^{R_{\mathrm{d}}/C_{\mathrm{p}}} \tag{3.3}$$

is also a conserved quantity, and thus, p_0 is expressed by T_0 as

$$p_0 = p_{\mathrm{s}} \left(\frac{T_0}{\theta} \right)^{C_{\mathrm{p}}/R_{\mathrm{d}}}, \tag{3.4}$$

where p_{s}, C_{p}, and R_{d} are standard air pressure (= 1000 hPa), the specific heat at constant pressure, and the gas constant for dry air, respectively.

State variables representing the atmospheric condition (T, p, V_{a}) satisfy the following thermodynamic equation describing adiabatic process:

$$C_{\mathrm{p}} \frac{dT}{dt} - \frac{R_d T}{p} \frac{dp}{dt} = J \ \ (= 0). \tag{3.5}$$

Here, J is the applied heat per unit mass taken to be zero in this study. The adiabatic ascent is expressed by cooling applied to the air at the constant rate of $-\dot{T}$. In this case, T, p, and V_{a} are represented by using T_0 and $\dot{T}$ as follows:

- Air temperature $T(t)$:

$$T(t) = T_0 + \int_0^t \dot{T}\ dt'. = T_0 + \dot{T} t \tag{3.6}$$

- Air pressure $p(t)$: From the Eqs. (3.4), (3.5), and (3.6),

$$p(t) = p_0 \left(1 + \frac{\dot{T}}{T_0} t\right)^{C_\mathrm{p}/R_d} = p_\mathrm{s} \left(\frac{T_0 + \dot{T}t}{\theta}\right)^{C_\mathrm{p}/R_d}. \tag{3.7}$$

- Volume of air $V_\mathrm{a}(t)$: From the Eqs. (3.1), (3.6), and (3.7),

$$V_\mathrm{a}(t) = V_{\mathrm{a}0} \left(1 + \frac{\dot{T}}{T_0} t\right)^{1 - C_\mathrm{p}/R_d}. \tag{3.8}$$

On the other hand, the amount of water vapor in the air mass is described by the volume mixing ratio $\chi(t)$, partial pressure of water $p_\mathrm{v}(t)$, and amount of substance of water vapor $n_\mathrm{v}(t)$. These variables satisfy the following equations based on ideal gas law about water vapor.

$$p_\mathrm{v}(t) = \chi(t) p(t), \quad p_\mathrm{v}(t) V_\mathrm{a}(t) = n_\mathrm{v}(t) R^* T(t). \tag{3.9}$$

When the initial conditions T_0, θ and χ_0 are given, p_0 is determined from Eq. (3.4). The initial values of water vapor pressure $p_{\mathrm{v}0}$ and amount of substance of water $n_{\mathrm{v}0}$ are obtained from Eq. (3.9). Before the ice nucleation is initiated, χ and n_v are kept constant at the values of χ_0 and $n_{\mathrm{v}0}$, while p_v decreases in response to the pressure decrease (Eq. (3.9)). Once p_v at each time step is determined from above equations, Δa_w is obtained from Eq. (1.3) by using T, p_v and p_i, which is calculated by

$$p_\mathrm{i} = \exp\left(9.550426 - \frac{5723.265}{T} + 3.5308 \ln T - 0.00728332 T\right), \tag{3.10}$$

referring to *Murphy and Koop* (2005), ice nucleation is described by applying J_c, calculated from Eq. (1.2) using Δa_w, to Eq. (1.1).

In this model, the radius r and number concentration n of aerosols is given as initial conditions (under monodisperse aerosol). Because the generation, growth and merging

of aerosol particles is not considered, r (thus, $V = 4\pi r^3/3$ in Eq. (1.1)) is conserved through the simulation, and number of aerosols $N = nV_{a0}$ is conserved until ice nucleation is initiated. Following the increase of J_c associated with adiabatic cooling (Eq. (3.6)), ice nucleation is initiated ($N_i \geq 1$). The number of ice particles is denoted by $[N_i]$, which is the integral part of N_i. The number concentration of ice particles n_i is calculated by n_i=$[N_i]/V_a$. Nucleated ice particles are assumed to have spherical shape (*Lawson et al.*, 2008) with the radius r_i. At the time of ice nucleation, r_i is the same as the source aerosol.

The depositional growth is calculated in a Lagrangian fashion; i.e., the time evolution of individual ice particles is traced from the following equation (*Hamill et al.*, 1977; *Pruppacher et al.*, 1998; *Daneva and Shibata*, 2001):

$$\frac{dr_i}{dt} = \frac{M_w D(p_v - Kp_i)}{\rho_i N_A r_i (1 + \lambda K_n) kT}. \tag{3.11}$$

Here, M_w, D, N_A and k are the molecular weight of water, the diffusion coefficient (*Fuchs and Sutugin*, 1971), the Avogadro's number and the Boltzmann constant, respectively. The Knudsen number, K_n, is a measure of ambient gas molecules surrounding the ice particles whether the continuum formulation of fluid dynamics could be applied or not. The Kelvin term, K, represents the Kelvin effect in which the vapor pressure over a curved surface is greater than that over flat plane. Correction factor λ, used to calculate K_n, is obtained from the following equation (*Fuchs and Sutugin*, 1971):

$$\lambda = \frac{1.333 + 0.71{K_n}^{-1}}{1 + {K_n}^{-1}} + \frac{4(1-\alpha)}{3\alpha}. \tag{3.12}$$

The r_i-dependency of the absorbed water amount with respect to ice growth is expressed by considering the time evolution of the number of water molecules in one ice particle M_i ($= (4/3)\pi {r_i}^3 \rho_i N_A / M_w$). Substituting Eq. (3.11), we may have

$$\frac{dM_i}{dt} = \frac{4\pi r_i D(p_v - Kp_i)}{(1 + \lambda K_n) kT}, \tag{3.13}$$

which shows that the absorbed water amount associated with the ice growth is proportional to $r_{\rm i}$.

The decrease of water vapor associated with the growth of ice particles is calculated as follows by using the number of water molecules $M_{{\rm i}j}$ in j-th nucleated ice particle ($j = 1, \cdots, [N_{\rm i}]$):

$$n_{\rm v}(t) = n_{\rm v0} - \frac{1}{N_{\rm A}} \sum_{j}^{[N_{\rm i}]} M_{{\rm i}j}(t). \tag{3.14}$$

Then, $\chi(t)$ is calculated by

$$\chi(t) = \frac{n_{\rm v}(t)}{n_{\rm a}}. \tag{3.15}$$

This $\chi(t)$ and $p(t)$ given by Eq. (3.7) can be combined to calculate $p_{\rm v}$ of the next time step. The process of nucleation and growth of ice particles are, thus, calculated by integrating Eqs. (1.1) and (3.13).

In Chapters 3 and 4, the results with $\alpha = 0.3$ are shown by referring to *Pratte et al.* (2006), and the dependency on α is discussed as the range of uncertainty of the results. The initial volume of the air mass $V_{\rm a0}$ is set to 1 L. In case the maximum number of ice particles $N_{\rm i}^{\rm max}$ is less than 10^4, the calculation is repeated by making $V_{\rm a0}$ larger until $N_{\rm i}^{\rm max} \geq O(10^4)$ to ensure the significance of the results. Thus $V_{\rm a0}$ is generally different in each experiment ranging from 1 to $\sim 10^4$ L. The aerosols are assumed to be monodisperse with the number concentration of 10^5 L^{-1} referring to the measurements in the upper tropical troposphere (*Brock et al.*, 1995; *Borrmann et al.*, 2010). This value is large enough to study the formation of ice particles with the concentration of 10^4 L^{-1} (*Kay and Wood*, 2008).

Based on above settings, a series of numerical experiments simulating the homogeneous ice nucleation taking place in the air mass advected isentropically in the TTL. Figure 3.1 shows the time series of ${\rm RH_i}$, p, T, χ, mean radius of nucleated ice particles $\bar{r}_{\rm i}$, and $n_{\rm i}$ as an example of model simulation associated with a case of $r = 0.01$ μm and $\chi_0 = 6$ ppmv. In response to the applied cooling (2.4 K h^{-1}), ${\rm RH_i}$ gradually increases as T decreases, and ice nucleation is initiated when ${\rm RH_i}$ reaches the threshold of homogeneous nucleation. ${\rm RH_i}$

and χ turn to decrease as the growth of nucleated ice particles by absorbing water vapor becomes evident until RH_i decreases below the nucleation threshold in about three minutes and n_i reaches 10^4 L^{-1}. During the progress of ice nucleation, $\bar{r}_i$ remains almost constant at $\sim$0.1 μm (dashed green curve) as the growth of nucleated particles is compensated for by the successive nucleation of small ice particles. Decrease of χ (solid green curve) is also invisible during this period and it becomes evident when $\bar{r}_i$ reaches $\sim$1 μm and the depositional growth of ice particles takes effect. The $\bar{r}_i$ increases as nucleated ice particles grow, and finally it reaches $\sim$ 1.9 μm when RH_i becomes enough low and the depositional growth of ice particles almost ceases. This study focuses on the ice-formation process, and considers the time evolution from the initiation of ice nucleation to the "termination" of particle growth defined by the condition of $RH_i < 101\%$. When the cooling rate is large, RH_i rises again before it reaches 101%. In this case, the termination of particle growth is defined at the time when RH_i takes the minimum.

Figure 3.2 shows the size distribution of nucleated ice particles achieved at the termination of particle growth for the experiment shown in Fig. 3.1. The mode radius of nucleated ice particles is found at the bin with the particle size of 1.82–1.91 μm; $\bar{r}_i$ also falls into this bin. The radius of all ice particles range from 1.32 to 3.63 μm. It is worth mentioning here that most of the simulated ice particles have the radius greater than 1.6 μm, while the radius of observed ice particles from ATTREX2011 falls almost exclusively in the range of 0.5–1.6 μm.

In the present study, n_i^{max} is examined as a function of $-\dot{T}$, χ_0, r, and α, and is denoted by $n_i^{max}(-\dot{T}, \chi_0, r, \alpha)$; the effects of sedimentation, mixing, and diffusion are not considered. The parameters $-\dot{T}$, χ_0, and r are swept in the ranges 0.1–100 K h^{-1}, 1–100 ppmv, and 0.01–10 μm, respectively, with $\alpha = 0.3$ to determine the cloud microphysical conditions necessary for the formation of TTL cirrus with the ice concentration of 10^4 L^{-1}. The variations associated with the uncertainty of α are discussed by sweeping it in the range 0.2–1.0 (*Skrotzki et al.*, 2013).

3.2 Number concentration of nucleated ice particles

In this Section, the dependencies of nucleated ice-particle concentration $n_{\rm i}^{\rm max}$ on each parameter ($-\dot{T}$, χ_0, r, α) are discussed referring to the cross sections of $n_{\rm i}^{\rm max}$ obtained by fixing two of the four parameters.

Figure 3.3 shows the distribution of $n_{\rm i}^{\rm max}$ as functions of $-\dot{T}$ and χ_0 while fixing the values of r and α to 0.01 μm and 0.3, respectively (distribution of $n_{\rm i}^{\rm max}(-\dot{T}$, χ_0, 0.01 μm, 0.3)). Contours are drawn based on the simulations with the parameters given by open diamonds. The red contour (10^4 L^{-1}) corresponds to the ice-particle concentration of the thin cirrus observed in ATTREX2011 (Fig. 1.7(C)). From the results, dependencies of $n_{\rm i}^{\rm max}$ on $-\dot{T}$ and χ_0 are summarized as follows.

With a constant χ_0, $n_{\rm i}^{\rm max}$ is an increasing function of $-\dot{T}$. This feature is consistent with the results of past modeling studies (*Kärcher and Lohmann*, 2002a,b; *Hoyle et al.*, 2005; *Jensen et al.*, 2010). This is understood as follows. For larger values of $-\dot{T}$, the rapid decrease of temperature leads to the rapid increase of the homogeneous nucleation rate coefficient $J_{\rm c}$ due to its strong dependency on T (and thus RH$_{\rm i}$) as can be seen from Eqs. (1.2) and (1.3). As the temperature dependency of $J_{\rm c}$ is much stronger than that of depositional ice growth (Eq. (3.13)), the successive ice nucleation prevails over the depositional growth of nucleated ice particles. After nucleation stops, a large number of ice particles deplete water vapor in excess of saturation effectively due to their large surface area. Therefore, the supersaturation is dissolved faster than the cases for smaller values of $-\dot{T}$. On the other hand, $n_{\rm i}^{\rm max}$ is a decreasing function of χ_0. This may be explained as follows. With a fixed $-\dot{T}$, the rate of depositional growth of ice particles is high when χ_0 is large (Eq. (3.13)). This leads to the rapid uptake of water vapor by existing ice particles, preventing the increase in RH$_{\rm i}$. As a result, the nucleation of successive ice particles is suppressed. This behavior of $n_{\rm i}^{\rm max}$ is equivalent to the frost point dependency discussed by *Kärcher and Lohmann* (2002a,b).

The dependency of $n_{\rm i}^{\rm max}$ on r and $-\dot{T}$ is discussed by choosing 6 ppmv as a represen-

tative value of χ_0 referring to the observed thin cirrus (Fig. 1.7(C)). Figure 3.4 shows the distribution of $n_{\rm i}^{\rm max}(-\dot{T}$, 6 ppmv, r, 0.3). One of the interesting features is that the sensitivity of $n_{\rm i}^{\rm max}$ to r is different between the lower left and the upper right domains of the diagram. We can see that the contours of $n_{\rm i}^{\rm max}$ is almost parallel to the abscissa so that $n_{\rm i}^{\rm max}$ is almost a function of $-\dot{T}$ in the lower left domain. On the other hand, the contours are directed from lower left to upper right indicating some dependency of $n_{\rm i}^{\rm max}$ on r in the upper right domain. The decreasing tendency of $n_{\rm i}^{\rm max}$ with respect to r at a constant $-\dot{T}$ is due to the improved efficiency of water vapor uptake by aerosols with large nuclei (and thus large ice particles) corresponding to those distributed in the upper right domain of the diagram.

Finally, $n_{\rm i}^{\rm max}$ dependency on α, the uptake efficiency of water molecules by the growth of ice particles, is briefly mentioned here. For larger values of α, each ice particle has higher growth rates leading to the suppressed nucleation of successive ice particles and resulting in the smaller numbers of $n_{\rm i}^{\rm max}$. The hatching in Fig. 3.4 indicates the range of the contour of 10^4 L^{-1} when α is swept from 0.2 (lower boundary of the hatching) to 1.0 (upper boundary). With a fixed r ($-\dot{T}$), a larger value of $-\dot{T}$ (a smaller number of r) is required for a larger number of α. When r is small, the dependency of $n_{\rm i}^{\rm max}$ on r becomes unimportant so that α becomes an influential parameter as well as $-\dot{T}$.

3.3 Size distribution of ice particles

Figure 3.5 shows the size distributions of nucleated ice particles at the moment when the growth of ice particles is terminated for the cases of $n_{\rm i}^{\rm max} \sim 10^4$ L^{-1} with $r = 0.1$ μm (left) and $r = 1.0$ μm (right), i.e., $f_{\rm r_i}$(3.3 K h^{-1}, 6.0 ppmv, 0.1 μm, 0.3) and $f_{\rm r_i}$(30 K h^{-1}, 6.0 ppmv, 1.0 μm, 0.3), respectively, in our notation. The features we see from $f_{\rm r_i}$(3.3 K h^{-1}, 6.0 ppmv, 0.1 μm, 0.3)(Fig. 3.5 left) is similar to those from $f_{\rm r_i}$(2.4 K h^{-1}, 6.0 ppmv, 0.01 μm, 0.3)(Fig. 3.2). This will be because the experimental conditions for both figures

are similar. More specifically, the coordinate (r, $\dot{T}$) is located in the lower left domain of Fig. 3.4, where the $n_{\mathrm{i}}^{\mathrm{max}}$ dependency on r, thus the $f_{\mathrm{r_i}}$ dependencies on r is small. The radius of ice particles ranges from 1.32 to 3.31 μm and the mode radius is found in the bin of 1.82–1.91 μm for the case of $f_{\mathrm{r_i}}$(3.3 K h^{-1}, 6.0 ppmv, 0.1 μm, 0.3). The size range is similar to that of $f_{\mathrm{r_i}}$(2.4 K h^{-1}, 6.0 ppmv, 0.01 μm, 0.3)(Fig. 3.2), but the bin of largest ice particles shifts one rank to smaller size and the size distribution shows more compact shape at the vicinity of mode radius. This compactness may be understood as follows. In the case of $r = 0.1$ μm, the water vapor uptake by nucleated ice particles is faster and the period necessary to dissolve the supersaturation is shorter as compared to the case of $r = 0.01$ μm. Consequently, the difference in the growth rate of nucleated ice particles is kept small, leading to the narrow size distribution of nucleated ice particles.

The size distribution $f_{\mathrm{r_i}}$(30 K h^{-1}, 6.0 ppmv, 1.0 μm, 0.3)(Fig. 3.5 right), corresponding to the set of parameters located in the upper right domain of Fig. 3.4 (strong dependency of $n_{\mathrm{i}}^{\mathrm{max}}$ on r), has a narrow knifelike shape different from the other two cases discussed above. The radius of ice particles is distributed in an extremely narrow range (radius of 2.09–2.51 μm). This is because large ice particles nucleated from large aerosols have grown quite rapidly and the supersaturation is dissolved in a short period. The mode radius of ice particles, being found in the particle size bin of 2.29–2.40 μm, is larger than that in the cases of $r = 0.1$ μm and $r = 0.01$ μm.

Comparing the size distributions $f_{\mathrm{r_i}}$ under the condition of fixed $n_{\mathrm{i}}^{\mathrm{max}}$, we can see that the dependency of $f_{\mathrm{r_i}}$ on r is not so evident, the radius of ice particles is widely distributed, and the mode radius is relatively small when r is small, but that the $f_{\mathrm{r_i}}$ dependency on r is pronounced, the size distribution shows narrow knifelike peak, and the mode radius is large when r is large.

3.4 Two effects on ice nucleation

The $n_{\rm i}^{\rm max}$ dependencies on each parameter ($-\dot{T}$, χ_0, r, α) are summarized as follows.

1. $n_{\rm i}^{\rm max}$ increases as the increase of cooling rate.
2. $n_{\rm i}^{\rm max}$ decreases as the increase of initial water mixing ratio.
3. $n_{\rm i}^{\rm max}$ decreases as the increase of aerosol radius (r) non-linearly pronounced in large r.
4. $n_{\rm i}^{\rm max}$ decreases as the increase of accommodation coefficient.

In particular, the Feature 3, demonstrating a clear nonlinearity, is understood by considering the following two effects that affect nucleation and growth of ice particles.

(a) Large (small) aerosols create small (large) numbers of large (small) ice particles due to the size dependency of the growth rate of ice particles.

(b) Large (small) aerosols initiate ice nucleation at a low (high) saturation ratio.

The Effect (a) indicates that the successive nucleation of ice particles is suppressed as the radius of aerosols is large, because nucleated large ice particles absorb water vapor efficiently. The feature that $n_{\rm i}^{\rm max}$ decreases as r increases (Fig. 3.4) is understood by Effect (a). In particular, the fact that the dependency of $n_{\rm i}^{\rm max}$ on r becomes evident for large r implies that Effect (a) becomes also evident for large r. Besides, the dependency of $f_{\rm r_i}$ on r, investigated by comparing $f_{\rm r_i}$ under the conditions of different set of $-\dot{T}$ and r but resulting in the same $n_{\rm i}^{\rm max}$ (Section 3.3), demonstrates that it is small (large) when r is small (large). This is explained as follows. In order to keep the resultant ice concentration $n_{\rm i}^{\rm max}$ in the order of 10^4 L^{-1}, large (small) $-\dot{T}$ and quick (sustained) ice-nucleation process are required. This is because the water vapor uptake efficiency by ice growth is high (low) when the aerosol radius is large (small), thus nucleated ice particles are large (small) due

to Effect (a). Therefore, the shape of $f_{\mathrm{r_i}}$ becomes narrow (wide) and the mode radius becomes large (small) for aerosols of large (small) radius.

The Effect (b) could be understood by referring to Eq. (1.1). The number of nucleated ice particles per unit time dN_{i}/dt is expressed as the product of the volume of aerosols V, the number of aerosols N, and the homogeneous nucleation rate coefficient J_{c} which increases drastically as $\mathrm{RH_i}$ increases (Eqs. (1.2) and (1.3)). In consequence, ice nucleation is initiated at a lower $\mathrm{RH_i}$ for larger radius and the same number of aerosols.

From Effect (a) and Effect (b), it is suggested that the interaction between the aerosols with different radius could affect the ice-nucleation processes, which is not investigated under monodisperse aerosols. Furthermore, the interesting feature of $n_{\mathrm{i}}^{\mathrm{max}}$-dependency on r shown in Fig. 3.4 suggests that the aerosol interaction will depend on the sizes of aerosols. In the next chapter, the effect of aerosol interactions on homogeneous nucleation is discussed by introducing a bimodal distribution of aerosols.

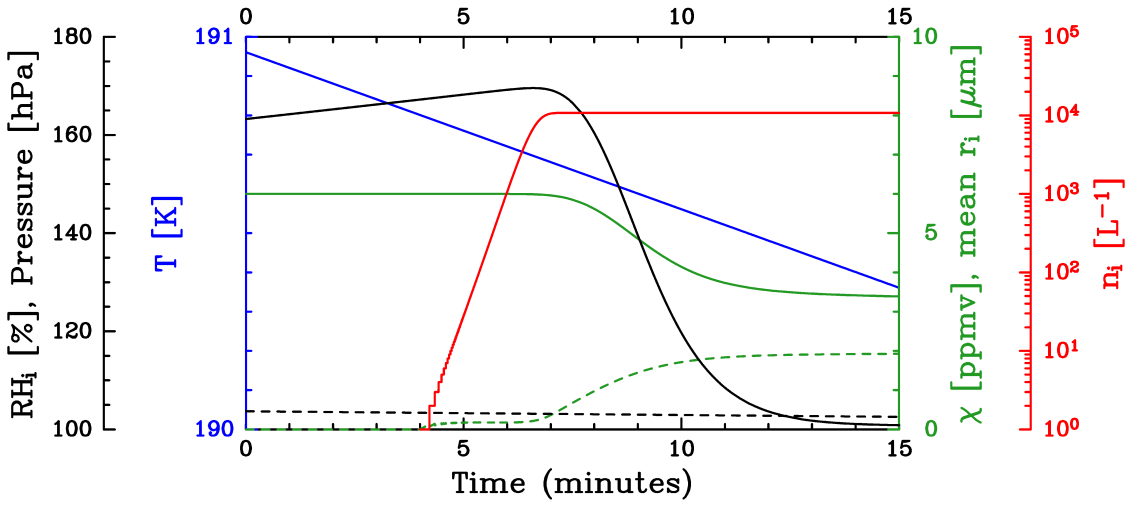

Figure 3.1: Time series of microphysical quantities calculated by the cloud microphysical model over a period of 15 minutes including the start and finish of ice nucleation. The assumed cooling rate is 2.4 K h^{-1}, the initial water vapor mixing ratio is 6 ppmv, the radius of aerosol particles is 0.01 μm, and the accommodation coefficient is 0.3. Relative humidity over ice is plotted in solid black, pressure in dashed black, temperature in blue, water vapor mixing ratio in solid green, mean radius of nucleated ice particles in dashed green, and ice-particle concentration in red (*Mimura et al.*, 2016).

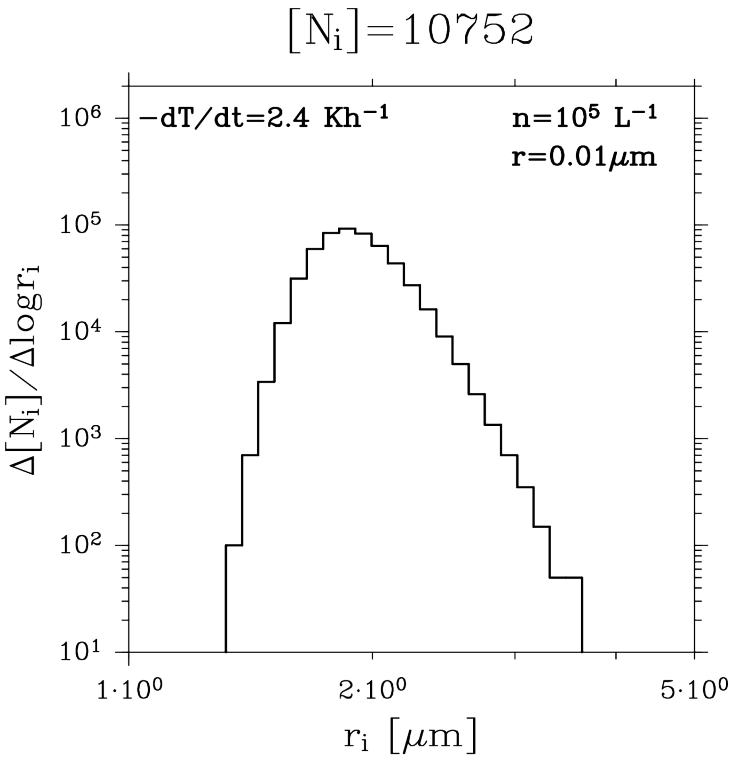

Figure 3.2: The size distribution of ice particles at the moment when the supersaturation is dissolved, obtained from the simulation shown is Fig. 3.1.

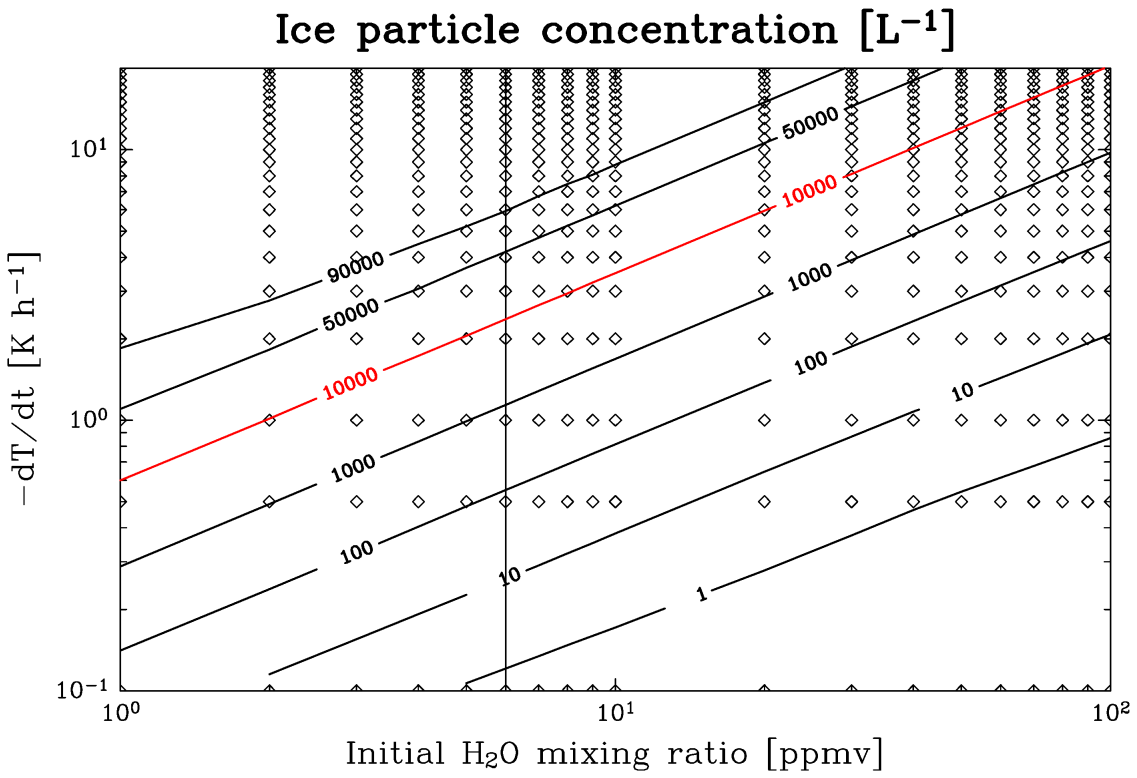

Figure 3.3: Distribution of maximum ice-particle concentration ($n_{\mathrm{i}}^{\mathrm{max}}$, contours) expressed as a function of cooling rate ($-dT/dt$; $-\dot{T}$) and initial water vapor mixing ratio for a fixed aerosol radius of 0.01 μm. Contours are drawn based on values from simulations with parameters given by the open diamonds. The black vertical line indicates the observed water vapor mixing ratio when the high ice-particle concentration cirrus was sampled (*Mimura et al.*, 2016).

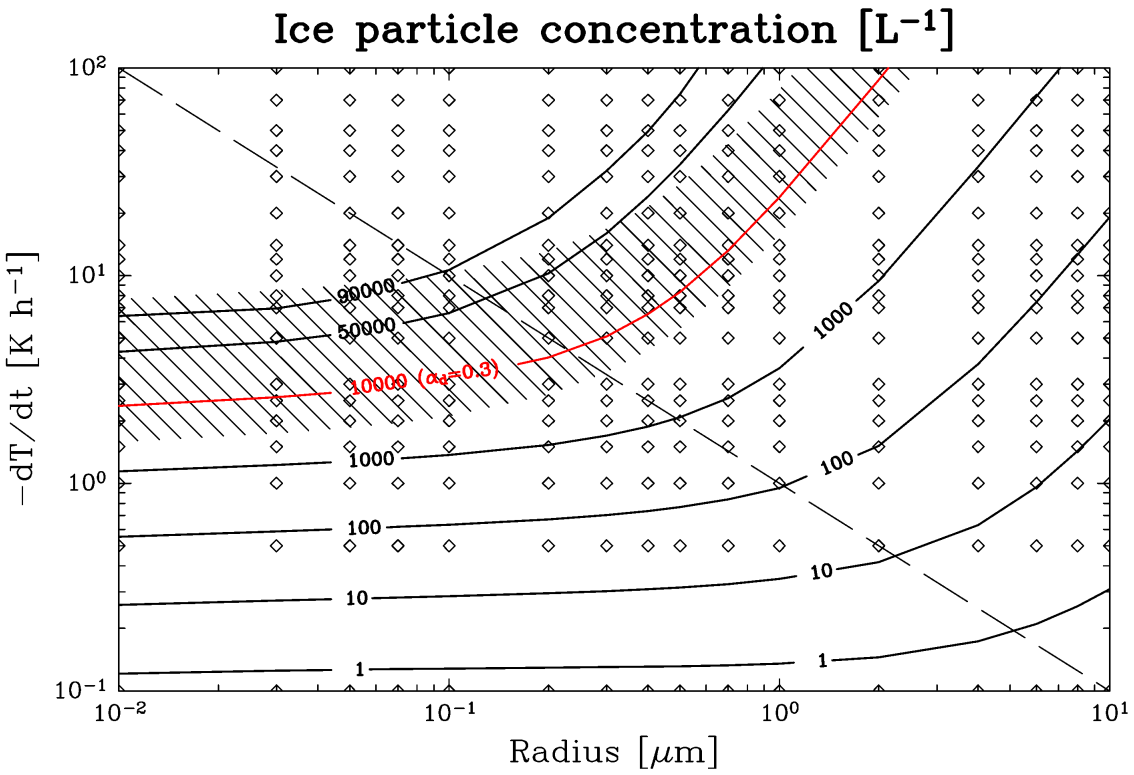

Figure 3.4: As for Fig. 3.3 except that $n_{\rm i}^{\rm max}$ is expressed as a function of cooling rate and radius of aerosol particles. The initial water vapor mixing ratio is taken to be 6 ppmv. Hatching indicates the range of the contour of 10^4 L^{-1} when α is swept from 0.2 (lower boundary of the hatching) to 1.0 (upper boundary). The dashed line indicates the boundary that roughly divides the parameter domain between weak (lower left) or strong (upper right domain) dependency of $n_{\rm i}^{\rm max}$ on aerosol size (*Mimura et al.*, 2016).

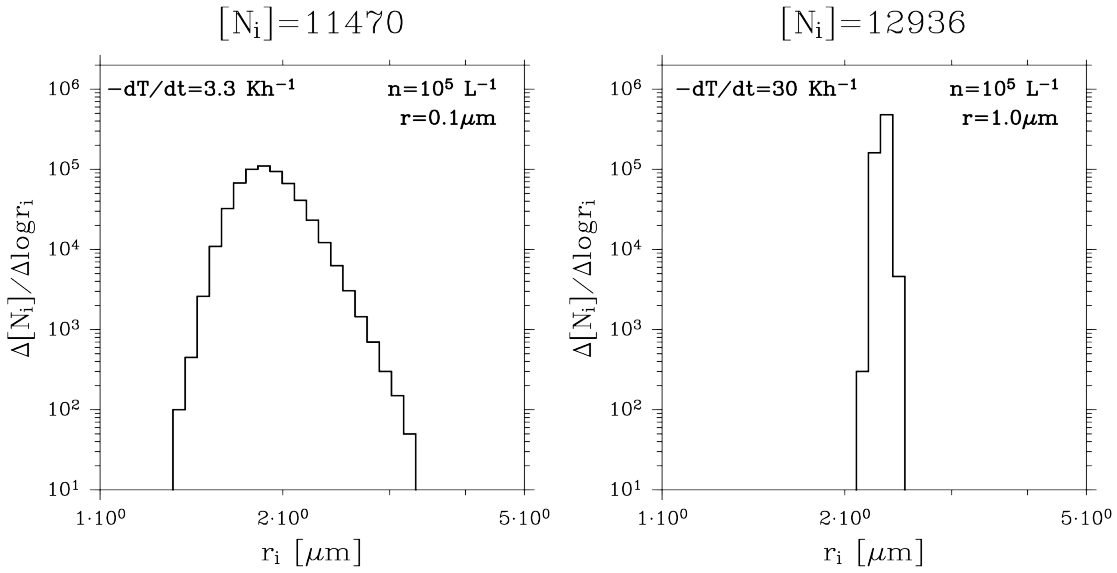

Figure 3.5: Same as Fig. 3.2, but for the results under the condition of $-\dot{T} = 3.3$ K h^{-1}, $\chi_0 = 6.0$ ppmv, and $r = 0.1$ μm (left), and $-\dot{T} = 30$ K h^{-1}, $\chi_0 = 6.0$ ppmv, and $r = 1.0$ μm (right).

Chapter 4

Simulations with bimodal aerosols

In this chapter, a simulation assuming the bimodal size distribution of aerosols is shown as an example of interaction between two kinds of aerosols (Section 4.1), and the size dependency of the interaction is discussed assuming two kinds of aerosols with the same number concentration but different radius (Section 4.2). The effect of aerosol number concentrations on the interaction is investigated in Section 4.3, and the size distributions of nucleated ice particles are discussed in Section 4.4.

4.1 Bimodal aerosol size distribution

Let assume two kinds of aerosols with the radii (r_a, r_b), number of particles (N_a, N_b), and particle number concentrations (n_a, n_b) as initial conditions. Figure 4.1 shows the time series of the simulations conducted under the conditions of $-\dot{T} = 3.3$ K h^{-1} and χ_0=6.0 ppmv with the monodisperse aerosols ($r = 0.1$ μm, $n = 2.0 \times 10^5$ L^{-1})(A), and with the bimodal aerosols ($r_\mathrm{a} = 0.1$ μm, $r_\mathrm{b} = 0.07$ μm, $n_\mathrm{a} = n_\mathrm{b} = 1.0 \times 10^5$ L^{-1})(B). In the simulation with bimodal aerosols (B), a half of monodisperse aerosols (A) are replaced by the same amount of small size aerosols. Time evolutions of RH$_\mathrm{i}$ (black), T (blue), χ (green) and ice nucleation ratio R are shown from the time of the first ice-particle

nucleation ($t = 0$) to the last ice nucleation. Ice nucleation ratio R is defined as the ratio of the number of nucleated ice particles ($[N_\mathrm{i}]$) to the initial number of aerosols (N), represented as $R = [N_\mathrm{i}]/N$. Red dashed line and red dash-dot line indicate ice nucleation ratios from large and small aerosols, represented as $R_\mathrm{a} = [N_\mathrm{ia}]/N$ and $R_\mathrm{b} = [N_\mathrm{ib}]/N$, respectively. As the temperature (blue) decreases associated with cooling, $\mathrm{RH_i}$ (black) increases and ice nucleation starts ($t = 0$) when $\mathrm{RH_i}$ exceeds the homogeneous nucleation threshold, which leads to the increase of R (red). Because the radius r_a of large aerosols is the same as that of monodisperse aerosols (0.1 μm), the ice nucleation starts from the aerosols of this size in both cases. However, a difference in the time evolution of R and that of $R_\mathrm{a} + R_\mathrm{b}$ emerges after the nucleation from small aerosols takes place in the bimodal case. If we compare R, R_a and R_b at the time of the last ice nucleation (the maximum ice nucleation ratio R^max, $R_\mathrm{a}^\mathrm{max}$, and $R_\mathrm{b}^\mathrm{max}$, respectively), $R_\mathrm{a+b}^\mathrm{max} = R_\mathrm{a}^\mathrm{max} + R_\mathrm{b}^\mathrm{max}$ is slightly larger than R^max, indicating that more ice particles nucleate from aerosols with bimodal size distribution. Hereafter, we call this the amplification effect. The feature that the ice nucleation starts from large aerosols in the bimodal case is explained by Effect (b) pointed out from the simulations with monodisperse aerosol. On the other hand, it is found that the maximum ice nucleation ratio from small aerosols $R_\mathrm{b}^\mathrm{max}$ is smaller than that from large aerosols $R_\mathrm{a}^\mathrm{max}$. This makes a contrast to the expectation from Effect (a) derived from monodisperse aerosols, that is, the number of nucleated ice particles is larger for smaller aerosols. In the case of bimodal aerosols, however, fast ice growth of large ice particles (nucleated from large aerosols) suppresses the nucleation from small aerosols that follows. The ice nucleation from two kinds of aerosols are thus not independent, and it is quite interesting to study the nucleation processes of ice particles with bimodal aerosols, suggesting an amplification of the number of ice particles due to aerosol interaction.

4.2 The size dependency of aerosol interaction

4.2.1 The amplification effect

In order to study the aerosol size dependency of the amplification effect, maximum ice nucleation ratios $R_{\mathrm{a}}^{\max}$ and $R_{\mathrm{b}}^{\max}$ are calculated by sweeping r_{b} (0.01–10 μm) under the condition of fixed r_{a} (0.1 μm) assuming the initial aerosol concentrations of $n_{\mathrm{a}} = n_{\mathrm{b}} = 10^5$ L^{-1}. Figure 4.2 shows the dependency of $R_{\mathrm{a}}^{\max}$, $R_{\mathrm{b}}^{\max}$ and $R_{\mathrm{a+b}}^{\max}$ on r_{b}. The red line indicates maximum ice nucleation ratio under monodisperse aerosols for comparison. It becomes larger as r becomes smaller. This is explained by Effect (a) (Section 3.4). Dashed, dotted, and solid lines in black indicate $R_{\mathrm{a}}^{\max}$, $R_{\mathrm{b}}^{\max}$ and $R_{\mathrm{a+b}}^{\max}$, respectively, calculated under the bimodal aerosols. The black solid line crosses the red line at $r_{\mathrm{b}} = r_{\mathrm{a}}$ indicated by the vertical line positioned at the fixed value of r_{a} (0.1 μm). The blue horizontal line, which extends from the point where $r_{\mathrm{b}} = r_{\mathrm{a}}$ to the left boundary, indicates maximum ice nucleation ratio under the monodisperse aerosols with the radius $r_{\mathrm{b}} = r_{\mathrm{a}} = 0.1$ μm for reference.

The features of aerosol interaction described as a function of r_{b} could be specified by relative magnitude of r_{b} to r_{a}. The first domain is characterized by a big difference between the radii r_{a} and r_{b} (Domain 1: $r_{\mathrm{b}} \gg r_{\mathrm{a}}$, and Domain 2: $r_{\mathrm{b}} \ll r_{\mathrm{a}}$). In Domain 1, $R_{\mathrm{a+b}}^{\max}$ (black solid) is approximated by $R^{\max}$ (red) indicating the proximity to monodisperse aerosols with $r = r_{\mathrm{b}}$. This is because the nucleation rate of aerosol b (large aerosol) is much larger than that of aerosol a (small aerosol) due to Effect (b), and the nucleation of aerosol a is almost negligible. In Domain 2, $R_{\mathrm{a+b}}^{\max}$ tends to $R^{\max}$ (blue horizontal line) calculated with monodisperse aerosols of $r = r_{\mathrm{a}}$. Again, this is because the nucleation rate of large aerosol is much larger than that of small aerosol due to Effect (b). These features can be summarized as follows: in the domain in which there is an appreciable difference between the radius of two kinds of aerosols, the total amount of $R^{\max}$ is well approximated by $R^{\max}$ of large aerosols and the aerosol interaction is negligible.

The aerosol interaction becomes evident in the domain in which the radius of two kinds of aerosols is similar. In general, $R_{\mathrm{a}}^{\max}$ (dashed) decreases as r_{b} increases. This is because the nucleation of aerosol a is suppressed as r_{b} becomes large due to Effect (b). On the other hand, $R_{\mathrm{b}}^{\max}$ (dotted) has a maximum. This is brought about by two contrasting effects. One is Effect (a) that makes $R_{\mathrm{b}}^{\max}$ decrease as r_{b} increases (responsible for the decrease to the right hand side of the maximum). The other is Effect (b) that suppresses the nucleation of small aerosols due to the size dependency of nucleation rate (the decrease to the left hand side of the maximum). The results shown in Fig. 4.2 indicate that the nucleation ratio of bimodal aerosols $R_{\mathrm{a+b}}^{\max}$ is generally larger than that of monodisperse aerosols $R^{\max}$ (blue horizontal line connected at $r = r_{\mathrm{a}}$ to the left hand side of red line). The increase of the nucleation ratio, what we call the amplification effect due to aerosol interaction, is pronounced when r_{b} is close but not equal to r_{a}. This amplification may be understood as a part of nucleated ice particles in the case of monodisperse aerosols is replaced by those from small aerosols under the bimodal case. The small ice particles nucleated from small aerosols lead to weak suppression of the nucleation of successive ice particles, which results in a large number of ice particles to be nucleated. This feature suggests that Effect (a), that rules the ice nucleation of monodisperse aerosols, could apply also to that of bimodal aerosols.

4.2.2 The size dependency of the amplification effect

In this section, the size dependency of $R_{\mathrm{a+b}}^{\max}$ on r_{b} is investigated to explore the nature of the amplification effect. Figure 4.3 is the same as Fig. 4.2, but for $R_{\mathrm{a+b}}^{\max}$ corresponding to the different values of the radius of the fixed aerosol r_{a}. Each vertical line identifies the value of r_{a} for the curve of the corresponding color. From this figure, it is found that $R_{\mathrm{a+b}}^{\max}$ becomes large as r_{a} becomes small. This is understood by Effect (a) that states the number of nucleated ice particles increases as the radius of aerosols is small. It is interesting to note that the curves of $R_{\mathrm{a+b}}^{\max}$ appear similar, that is, $R_{\mathrm{a+b}}^{\max}$ takes maximum to the left side

of $r_{\rm a}$ and decrease, monotonously to zero as $r_{\rm b}$ becomes large.

In order to explore the physical foundation of this feature, Fig. 4.3 is rewritten by scaling the horizontal axis by $r_{\rm a}$. The result is shown in Fig. 4.4. Because $n_{\rm a}$ and $n_{\rm b}$ are the same, $r_{\rm a}$ and $r_{\rm b}$ are reversible. For example, the value of $R^{\rm max}_{\rm a+b}$ with $r_{\rm a} = 0.05$ and $r_{\rm b} = 0.1$ ($r_{\rm b}/r_{\rm a} = 2.0$) is equal to that with $r_{\rm a} = 0.1$ and $r_{\rm b} = 0.05$ ($r_{\rm b}/r_{\rm a} = 0.5$). In order to avoid this redundancy, we denote the two types of aerosols as large and small with the radii $r_{\rm l}$ and $r_{\rm s}$ in stead of a and b. The horizontal axis is redefined as $r_{\rm s}/r_{\rm l}$ and is shown in the range of $[0, 1]$. In addition, the maximum nucleation ratio, rewritten by $R^{\rm max}_{\rm s+l}$, is also normalized by that of monodisperse aerosols ($R^{\rm max}_{r_{\rm s}=r_{\rm l}}$). As a result, the amplification effect is represented by a non-dimensional value. The result is shown in Fig. 4.5. The asterisks indicate the maxima of the amplification effect defined as the magnitude of $R^{\rm max}_{\rm s+l}$ relative to $R^{\rm max}_{r_{\rm s}=r_{\rm l}}$ ($R^{\rm max}_{\rm s+l}/R^{\rm max}_{r_{\rm s}=r_{\rm l}}$). The amplification effect due to aerosol interaction appears in the domain wherever the value is greater than unity. It is readily seen that the maximum of $R^{\rm max}_{\rm s+l}/R^{\rm max}_{r_{\rm s}=r_{\rm l}}$ is large when $r_{\rm l}$ is large, indicating the stronger amplification effect for larger aerosols. This feature is suggested from the findings of Fig. 3.4 indicating that the dependency of $n_{\rm i}^{\rm max}$ on r becomes evident for large aerosols. In other wards, the amplification effect is large for large aerosols in the case of bimodal aerosols. Another interesting feature is that this amplification effect takes maximum at around $r_{\rm s}/r_{\rm l} = 0.7$ irrespective of $r_{\rm l}$.

4.3 The concentration dependency of aerosol interaction

Equation (1.1) indicates that the number of nucleated ice particles per unit time (ice nucleation rate) is proportional to that of aqueous aerosol particles. In Section 4.3, the effect of number concentrations of bimodal aerosols on the aerosol interaction is investigated. For the purpose of investigating the size dependency of the amplification effect (Section 4.2),

we assumed the number concentration of 10^5 L^{-1} for large and small aerosols and that of 2×10^5 L^{-1} for monodisperse aerosols as sufficient values to nucleate ice particles with the concentration of 10^4 L^{-1}. In order to discuss the dependency of the aerosol interaction on the number of aerosols, we need to start from the examination of the range of n applicable to the nucleation of ice particles of 10^4 L^{-1}.

4.3.1 Setting of initial number concentration of aerosols

Firstly, the dependency of nucleated ice particles N_i on the initial concentration of aerosols is discussed under monodisperse aerosols. Figure 4.6 shows the variations of N_i as a function of n in the range of 10^3–10^7 L^{-1} for some typical values of r under the condition of $-\dot{T} = 3.3$ K h^{-1}, $\chi_0 = 6$ ppmv, and 1 L of initial air mass. The fact that the small values of r results in a large values of N_i is understood by Effect (a). The linear growth of N_i that appear as superposed lines in different color in the domain of relatively small n ($\leq 10^3$–10^4 L^{-1}) is due to the lack of aerosols available for ice nucleation. The number of nucleated ice particles is limited by that of aerosols N, and almost aerosols are nucleated ($N_\mathrm{i}\sim N$). Such a restriction must be avoided to understand the interaction of bimodal aerosols. We can see from Fig. 4.6 that the initial aerosol concentrations of 10^4 L^{-1} and 10^5 L^{-1} will be sufficient for the aerosols of $r = 1.0$ μm and $r = 0.02$ μm, respectively. One may note that N_i shows a slight decrease as n becomes large and takes a maximum in the case of small aerosols. This decrease is brought about by the suppression of ice nucleation due to the growth of already nucleated ice particles. As is stated by Eq. (1.1), ice nucleation rate is proportional to the number of aerosols and the ice nucleation is initiated at a lower $\mathrm{RH_i}$ in the case of larger N. From the results, we could regard the aerosol concentration of 10^5 L^{-1} as an appropriate value to discuss the formation process of the cirrus with the ice-particle concentration of 10^4 L^{-1} for the aerosols with the radius range of $0.02\leq r\leq 1.0$ μm. The dependency of aerosol interaction on the number concentration of large (n_l) and small (n_s) aerosols is studied in the next section.

4.3.2 Aerosol interaction under a fixed radius ratio of aerosols

Figure 4.7 shows the dependency of the maximum ice nucleation ratio $R_{\mathrm{s+l}}^{\mathrm{max}}$=$[N_{\mathrm{i}}]/(N_{\mathrm{s}}+N_{\mathrm{l}})$ on n_{s} under the condition of $r_{\mathrm{l}} = 0.1$ μm and $n_{\mathrm{l}} = 10^5$ L^{-1}. In order to make the amplification effect clear, a fixed size ratio of $r_{\mathrm{s}}/r_{\mathrm{l}} = 0.7$ is chosen. Black dashed and dash-dot curves indicate the maximum ice-nucleation ratio from large ($R_{\mathrm{l}}^{\mathrm{max}}$) and small ($R_{\mathrm{s}}^{\mathrm{max}}$) aerosols, respectively, while the red solid curve shows that of monodisperse aerosols (R^{max}). Black solid line is the sum of $R_{\mathrm{l}}^{\mathrm{max}}$ and $R_{\mathrm{s}}^{\mathrm{max}}$ ($= R_{\mathrm{s+l}}^{\mathrm{max}}$). Depending on the changes of n_{s} in the range of 10^3 L^{-1} to 10^7 L^{-1}, total number concentration of aerosols ($n = n_{\mathrm{s}}+n_{\mathrm{l}}$) varies from 1.01×10^5 to 1.01×10^7 L^{-1}. In the domain of $n_{\mathrm{s}} < 10^4$ L^{-1}, $n \sim n_{\mathrm{l}} \sim 10^5$ L^{-1} and the decrease of $R_{\mathrm{s+l}}^{\mathrm{max}}$ in response to the increase of n_{s} could be neglected. On the other hand, $R_{\mathrm{s+l}}^{\mathrm{max}}$ decreases as n_{s} increases (black solid) similar to the decrease of R^{max} under monodisperse aerosols (red solid) in the domain of $n_{\mathrm{s}} > 10^5$ L^{-1}. As for the contribution of large and small aerosols, we can see $R_{\mathrm{l}}^{\mathrm{max}}$ (dashed) decreases as n_{s} increases. This is because the facilitation of ice nucleation from small aerosols due to the increase of n_{s} leads to the suppression of ice nucleation from large aerosols. In contrast, $R_{\mathrm{s}}^{\mathrm{max}}$ (dashed-dot) takes a maximum. This is understood as the follows. Both $n_{\mathrm{i}}^{\mathrm{max}}$ and $R_{\mathrm{s}}^{\mathrm{max}}$ increase in response to the increase of n_{s} as long as n_{s} is subject to the limitation of ice nucleation from small aerosols. The increase of $n_{\mathrm{i}}^{\mathrm{max}}$ along with the increase of n_{s} stops as n_{s} becomes large. $R_{\mathrm{s}}^{\mathrm{max}}$ becomes well approximated by the maximum nucleation ratio of monodisperse aerosols with the radius of r_{s} as n_{s} becomes larger than n_{l}, because ice nucleation from large aerosol is suppressed.

The magnitudes of $R_{\mathrm{l}}^{\mathrm{max}}$ and $R_{\mathrm{s}}^{\mathrm{max}}$ are reversed at around $n_{\mathrm{s}} = 3 \times 10^5$ L^{-1}. This value seems to correspond to n_{sc}, the critical value of n_{s} at which the types (large or small) of aerosols nucleating first are reversed. The value of n_{sc} is derived as follows. Equation (1.1) indicates that the nucleation rate is proportional to the product of the volume of individual aerosol ($V = 4\pi r^3/3$) and the number of aerosols N. Under bimodal aerosol distribution, the magnitude of VN for small and large aerosols is reversed at $n_{\mathrm{sc}} = n_{\mathrm{l}} \left(r_{\mathrm{l}}/r_{\mathrm{s}}\right)^3$. For

example, $n_{\rm sc} = 2.92 \times 10^5$ L^{-1} if $n_{\rm l} = 10^5$ L^{-1} and $r_{\rm s}/r_{\rm l} = 0.7$. The reversal of the magnitude of $R_{\rm l}^{\rm max}$ and $R_{\rm s}^{\rm max}$ also takes place at around $n_{\rm sc}$ under several $r_{\rm s}/r_{\rm l}$ conditions ($n_{\rm sc} = 3.70\times10^6$ L^{-1} for $r_{\rm s}/r_{\rm l} = 0.3$, $n_{\rm sc} = 8.00\times10^5$ L^{-1} for $r_{\rm s}/r_{\rm l} = 0.5$, and $n_{\rm sc} = 1.37\times10^5$ L^{-1} for $r_{\rm s}/r_{\rm l} = 0.9$). Since $N_{\rm s}$ and $N_{\rm l}$ are not constant but decrease as the ice nucleation proceeds, the above criterion holds as a diagnosis of which of the aerosols the ice nucleation begins. It means, the relative magnitudes of $R_{\rm s}^{\rm max}$ and $R_{\rm l}^{\rm max}$ depend almost entirely on that of the ice nucleation rate but only weakly on the growth of nucleated ice particles, indicating that the type of the aerosol (either large or small) nucleated first controls the relative magnitude of $R_{\rm s}^{\rm max}$ and $R_{\rm l}^{\rm max}$. A series of simulations conducted by giving the value of $r_{\rm l}$ different from 0.1 μm gave similar results on the $n_{\rm s}$-dependency of $R_{\rm s+l}^{\rm max}$.

4.3.3 The dependency on the radius ratio of aerosols

In this section, the dependencies of $R_{\rm s+l}^{\rm max}$ on $n_{\rm s}$ is further investigated for the cases of $r_{\rm s}/r_{\rm l}$ different from 0.7 as was considered in the previous section. The results are illustrated by plotting the ratio of $R_{\rm s+l}^{\rm max}$ to $R_{r_{\rm l}=r_{\rm s}}^{\rm max}$ ($R_{\rm s+l}^{\rm max}/R_{r_{\rm s}=r_{\rm l}}^{\rm max}$) as a function of $n_{\rm s}$. Figure 4.8 shows the results for the cases of $r_{\rm s}/r_{\rm l} = 0.7$ (dotted), 0.9 (dash-dot), 0.5 (dashed) and 0.3 (solid) assuming $r_{\rm l} = 0.1$ μm. As $n_{\rm s}$ becomes smaller, $R_{\rm s+l}^{\rm max}/R_{r_{\rm s}=r_{\rm l}}^{\rm max}$ approximates to 1 because the aerosol distribution comes close to monodisperse. Due to Effect (a), on the other hand, $R_{\rm s+l}^{\rm max}/R_{r_{\rm s}=r_{\rm l}}^{\rm max}$ increases along with the increase of $n_{\rm s}$ owing to the increase of ice particles nucleated from small aerosols. Ice nucleation is approximated by that of monodisperse aerosol condition with $r = r_{\rm s}$ and $n = n_{\rm s}$ when $n_{\rm s}$ becomes enough large to make the ice nucleation from small aerosols dominant. The increasing tendency of $R_{\rm s+l}^{\rm max}/R_{r_{\rm s}=r_{\rm l}}^{\rm max}$ along with the increase of $n_{\rm s}$ is strong (weak) when $n_{\rm s}$ is smaller (larger) than $n_{\rm sc}$ irrespective of the value of $r_{\rm s}/r_{\rm l}$. This is because the relative magnitude of $R_{\rm l}^{\rm max}$ and $R_{\rm s}^{\rm max}$ is reversed at $n_{\rm sc}$. We can regard $n_{\rm sc}$ as the critical value at which the dominance in the origin of ice particles changes between large and small aerosols. Therefore, the growth of $R_{\rm s+l}^{\rm max}/R_{r_{\rm s}=r_{\rm l}}^{\rm max}$ with respect to $n_{\rm s}$ becomes remarkable under the condition that

r_s/r_l (thus n_{sc}) is relatively small. This is also understood by Effect (b) pointed out under monodisperse aerosol condition. The increase of R_s^{max} in response to the increase of n_s is less evident for smaller aerosols, because ice nucleation rate of small aerosols is small. Accordingly, large values of n_s are required to make the ice nucleation from small aerosols dominant when r_s/r_l is small. The amplification effect appears stronger for smaller values of r_s/r_l (Fig. 4.8) when the ice nucleation from small aerosols is dominant (e.g., $n_s = 10^7$ L^{-1}), because the maximum ice nucleation ratio is large for small aerosols (Fig. 4.3) due to Effect (a).

The results for the cases of different values of r_l are almost the same as those shown above. The amplification effect of aerosol interaction is larger (smaller) for larger (smaller) r_l reflecting the feature seen in Fig. 4.5. Besides, the values of n_s required for the dominance of ice nucleation from small aerosols (monodisperse condition of small aerosols) are large in the case of large r_l. This is because the suppression of ice nucleation from small aerosol becomes strong as the size dependency of ice nucleation becomes large for large aerosols (upper right domain of Fig. 3.4).

4.4 The size distribution of nucleated ice particles

One of the advantages of introducing bimodal aerosol distribution is a possible realization of bimodal distribution of nucleated ice particles. The size distribution of ice particles is discussed in Section 3.3 by conducting a series of simulations with a fixed value of n_i^{max} under monodisperse aerosols. We found the change of the distribution function is small, the radius range of ice particles is wide, and the mode radius is small for small aerosols (Figs. 3.2 and 3.5). It is suggested that the differences in the ice-nucleation rate and in the growth rate between large and small aerosols could bring about bimodal distribution of nucleated ice particles. Here in this subsection, ice-particle size distributions are investigated by conducting a series of simulations for several values of r_s/r_l. The conditions are set to

$-\dot{T}$ = 3.3 K h^{-1}, χ_0 = 6.0 ppmv, r_l = 0.1 μm, and n_l = n_s = 10^5 L^{-1} referring to the nucleation condition of the ice-particle concentration of 10^4 L^{-1} under monodisperse aerosols. Hereafter, we show the ice-particle size distributions realized at a time when the supersaturation is almost dissolved (RH$_\mathrm{i}$ < 101%) by the growth of ice particles.

Figure 4.9 compares the size distributions of ice particles simulated under the conditions of $r_\mathrm{s}/r_\mathrm{l} = 0.1$ and $r_\mathrm{s}/r_\mathrm{l} = 0.7$. The number of nucleated ice particles originated from small aerosols (blue) is larger in the case of $r_\mathrm{s}/r_\mathrm{l} = 0.7$ than that of 0.1. This is explained by Effect (b) under the monodisperse aerosols, and is consistent with the discussions in Section 4.2. There is no appreciable difference between the size distributions of total ice particles (sum of red and blue) and those originated from large aerosols (red). The distribution functions are always monodisperse and the mode radii are found in the bin of 1.82–1.91 μm even when the values of $r_\mathrm{s}/r_\mathrm{l}$ are changed between 0 to 1. This is because the ice nucleation always starts from a large aerosol ($n_\mathrm{s}r_\mathrm{s}^3 < n_\mathrm{l}r_\mathrm{l}^3$) in the whole range of $r_\mathrm{s}/r_\mathrm{l}$, and R_l is always larger than R_s under this condition.

Similar simulations are repeated by changing the number concentration of small aerosols to 10^6 L^{-1} while that of large aerosols is retained to 10^5 L^{-1} (Fig. 4.10). The critical condition for realizing $R_\mathrm{s} \geq R_\mathrm{l}$ is $r_\mathrm{s}/r_\mathrm{l} \geq (n_\mathrm{l}/n_\mathrm{s})^{1/3} = 10^{-1/3} \sim 0.46$. When $r_\mathrm{s}/r_\mathrm{l} = 0.1$, the ice particles nucleated from small aerosols increase as compared to those when $n_\mathrm{s} = 10^5$ L^{-1} (Fig. 4.9 left) due to the increase of n_s. But the proportion of ice particles nucleated from small aerosols stays very small. In the case of $r_\mathrm{s}/r_\mathrm{l} = 0.7$ ($> 10^{-1/3}$), on the other hand, the number of ice particles nucleated from small aerosols [N_is] is larger than that from large aerosols [N_il] (Fig. 4.10 right). As for the mode radius of ice particles, that from small aerosols is smaller than that from large aerosols in the case of $r_\mathrm{s}/r_\mathrm{l} = 0.1$, although the mode radius of total ice particles is found in the bin of 1.82–1.91 μm, the same as that under monodisperse aerosols (left panel of Fig. 3.5). When $r_\mathrm{s}/r_\mathrm{l} = 0.7$, the mode radius of ice particles nucleated from both large and small aerosols is located in the same bin, but is shifted one rank small (1.74–1.82 μm). This shift is due to a large number of small

ice particles nucleated from small aerosols. As the first ice nucleation occurs from small aerosols, the nucleation from large aerosols is suppressed. However, the increase of $n_{\rm s}$ does not effectively shift the mode radius of ice particles as to realize bimodal distribution of ice particles even if $r_{\rm s}/r_{\rm l}$ is changed in the range of 0.1 to 1.0.

The reason why the size distribution of ice particles becomes monodisperse is because the radius of ice particles are widely distributed due to the depositional growth of ice particles until the supersaturation is dissolved. In order to realize bimodal distribution of ice particles, those ice particles nucleated from large aerosols should grow quickly while those from small aerosols must not grow appreciably. In view of the dependency of $n_{\rm i}^{\rm max}$ on r and the arguments presented in Sections 3.2 and 3.3, such a condition is found in the upper right domain of Fig. 3.4. Simulations are conducted under the conditions of $-\dot{T} = 30$ K h^{-1}, $\chi_0 = 6.0$ ppmv, $r_{\rm l} = 1.0$ μm, and $n = 10^5$ L^{-1}. The values of $r_{\rm s}/r_{\rm l}$ are chosen as the amplification effect ($R_{\rm s+l}^{\rm max}/R_{r_{\rm s}=r_{\rm l}}^{\rm max}$) becomes almost maximum for each value of $n_{\rm s}$, that is, 0.8, 0.7, and 0.6 are chosen for $n_{\rm s}$ of 10^4, 10^5, and 10^6 L^{-1}, respectively.

Figure 4.11 shows the size distributions of ice particles simulated under the condition of $n_{\rm s} = 10^5$ L^{-1} with $r_{\rm s}/r_{\rm l} = 0.1$ and 0.7. Although the values of $n_{\rm i}^{\rm max}$ and $r_{\rm s}/r_{\rm l}$ are the same as those of Fig. 4.9, the size distributions are qualitatively different. We can see a bimodal distribution function composed of two knifelike peaks for both cases. Bimodal distribution functions in similar shape appear except for the cases with the value of $r_{\rm s}/r_{\rm l}$ close to 1. The formation of distinguished two peaks results from the strong dependency of $n_{\rm i}^{\rm max}$ on r in the upper right domain of Fig. 3.4 (Section 3.3). Due to the strong cooling rate and fast growth of ice particles nucleated from large aerosols (Effect (a)), the ice particles, both from large and small aerosols, are distributed in the narrow ranges in radius.

Figure 4.12 shows the size distribution of ice particles obtained from the simulation with $n_{\rm s} = 10^4$ L^{-1}. In this case, ice nucleation from large aerosols is dominant in both $r_{\rm s}/r_{\rm l} = 0.1$ and 0.6 because these values are smaller than the critical value of $r_{\rm s}/r_{\rm l} = (n_{\rm l}/n_{\rm s})^{1/3} \sim 2.15$. The bimodal distribution of nucleated ice particles is obvious when $r_{\rm s}$ is enough small

($r_s/r_l = 0.1$). However, two peaks of the distribution function overlap and the bimodal distribution is no longer observed in the size distribution of total ice particles in the case of the maximum amplification effect ($r_s/r_l = 0.8$).

Figure 4.13 is the same as Fig. 4.12 but for the simulation condition of $n_s = 10^6$ L^{-1}. The values of r_s/r_l are 0.1 and 0.6. Nucleation from small aerosols exceeds that from large aerosols when r_s/r_l is larger than the critical value of $r_s/r_l \sim 0.46$. The bimodal distribution is obvious when r_s is small ($r_s/r_l = 0.1$). It becomes less obvious under the condition of the maximum amplification effect ($r_s/r_l = 0.6$), and the bimodal distribution of nucleated ice particles disappears when r_s/r_l is close to 1.

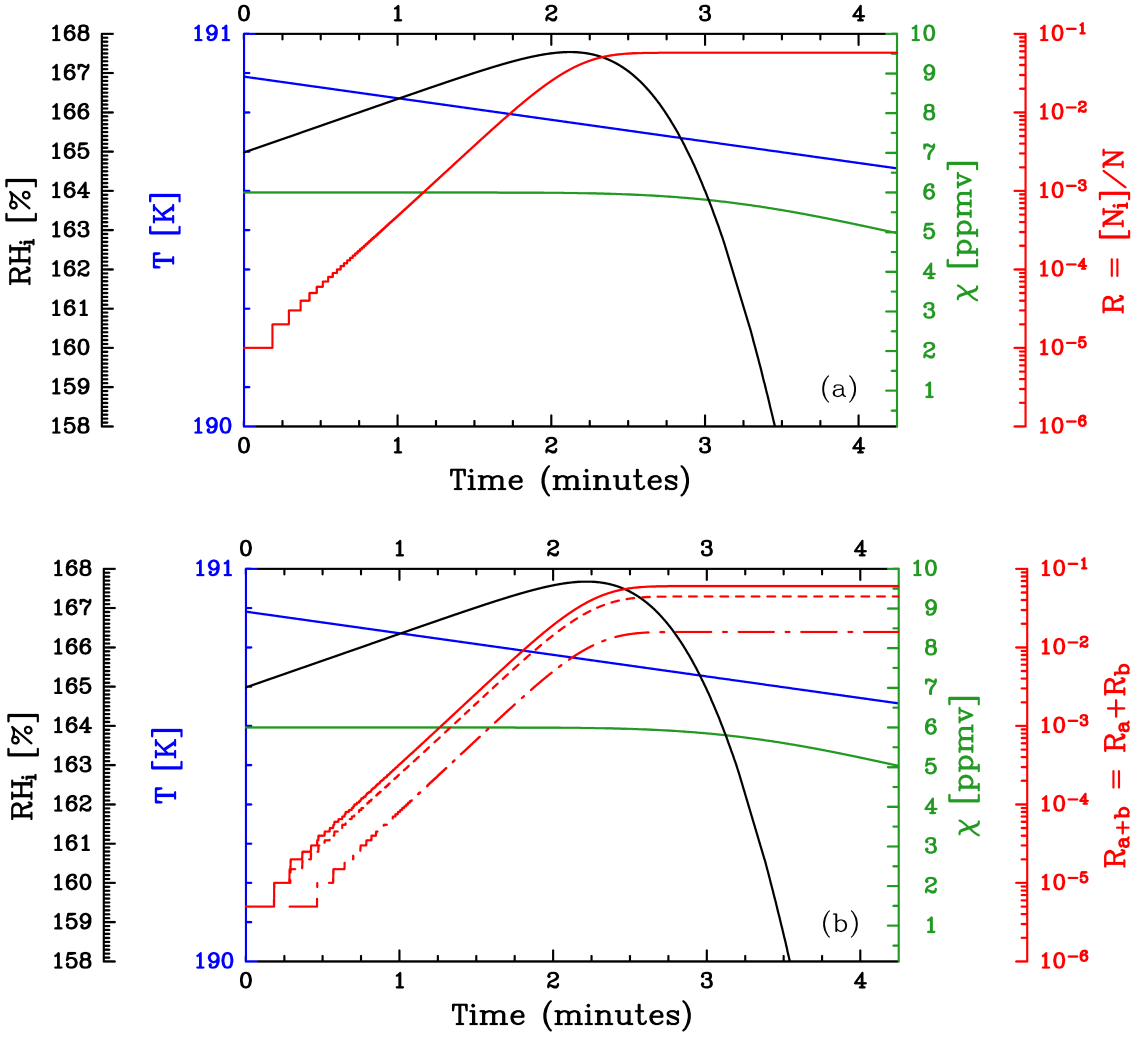

Figure 4.1: (A) Time evolutions, from the initiation ($t = 0$) to the termination of ice nucleation, of temperature (blue), relative humidity over ice (black), water vapor mixing ratio (green) and ice nucleation ratio (red) simulated under the conditions of cooling rate $-\dot{T} = 3.3$ K h^{-1}, initial water vapor mixing ratio $\chi_0 = 6.0$ ppmv, and monodisperse aerosols ($r = 0.1$ μm, $n = 2.0 \times 10^5$ L^{-1}). (B) Same as (A) but simulated under the bimodal aerosols ($r_\mathrm{a} = 0.1$ μm, $r_\mathrm{b} = 0.07$ μm, $n_\mathrm{a} = n_\mathrm{b} = 1.0 \times 10^5$ L^{-1}). The ice nucleation ratios R_a (dashed line), and R_b (dash-dot line) from large (r_a) and small (r_b) aerosols, respectively, and the sum ($R_\mathrm{a+b} = R_\mathrm{a} + R_\mathrm{b}$; solid line) are illustrated.

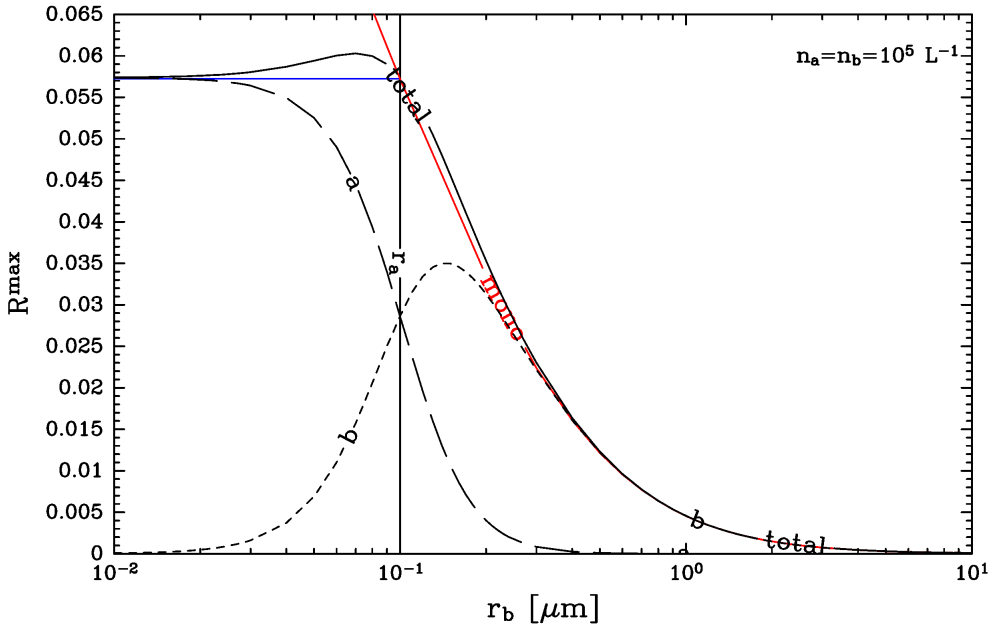

Figure 4.2: The dependencies of the maximum ice nucleation ratio of two kinds of aerosols $R_{\rm a}^{\rm max}$ (dashed) and $R_{\rm b}^{\rm max}$ (dotted) with the radius $r_{\rm a}$ and $r_{\rm b}$, respectively, and the sum $R_{\rm a+b}^{\rm max} = R_{\rm a}^{\rm max} + R_{\rm b}^{\rm max}$ (solid) on $r_{\rm b}$. The aerosol radius $r_{\rm a}$ is fixed to 0.1 μm (indicated by the vertical line) while $r_{\rm b}$ is swept in the range of 0.01–10 μm with the same number concentration ($n_{\rm a} = n_{\rm b} = 1.0 \times 10^5$ L^{-1}) under the condition of $-\dot{T} = 3.3$ K h^{-1} and $\chi_0 = 6.0$ ppmv. The $r_{\rm b}$ dependencies of the maximum ice nucleation ratio under monodisperse aerosols with $r = r_{\rm a}$ (blue) and $r = r_{\rm b}$ (red) are also shown for reference.

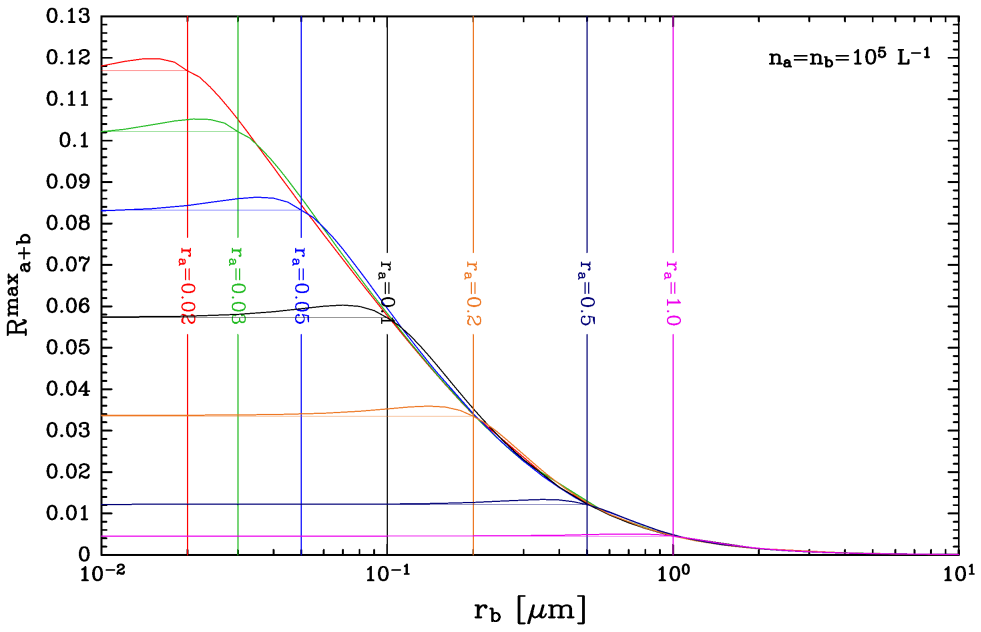

Figure 4.3: The dependencies of the maximum ice nucleation ratio $R^{\max}_{\mathrm{a+b}}$ on r_{b} simulated under the same condition as Fig.4.2 but for different r_{a}: 0.02 (red), 0.03 (green), 0.05 (blue), 0.1 (black), 0.2 (orange), 0.5 (navy-blue), and 1.0 (magenta) μm.

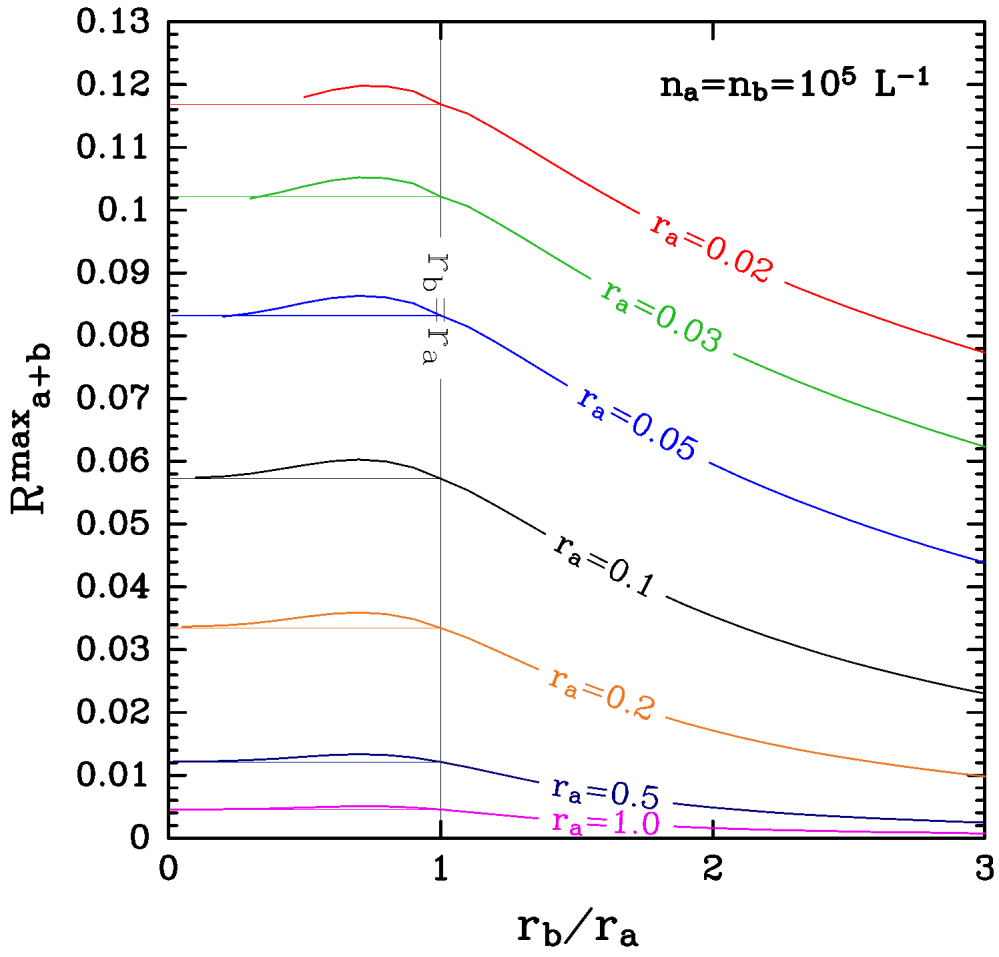

Figure 4.4: Same as Fig. 4.3, but rewritten by normalizing the horizontal axis by $r_{\rm a}$.

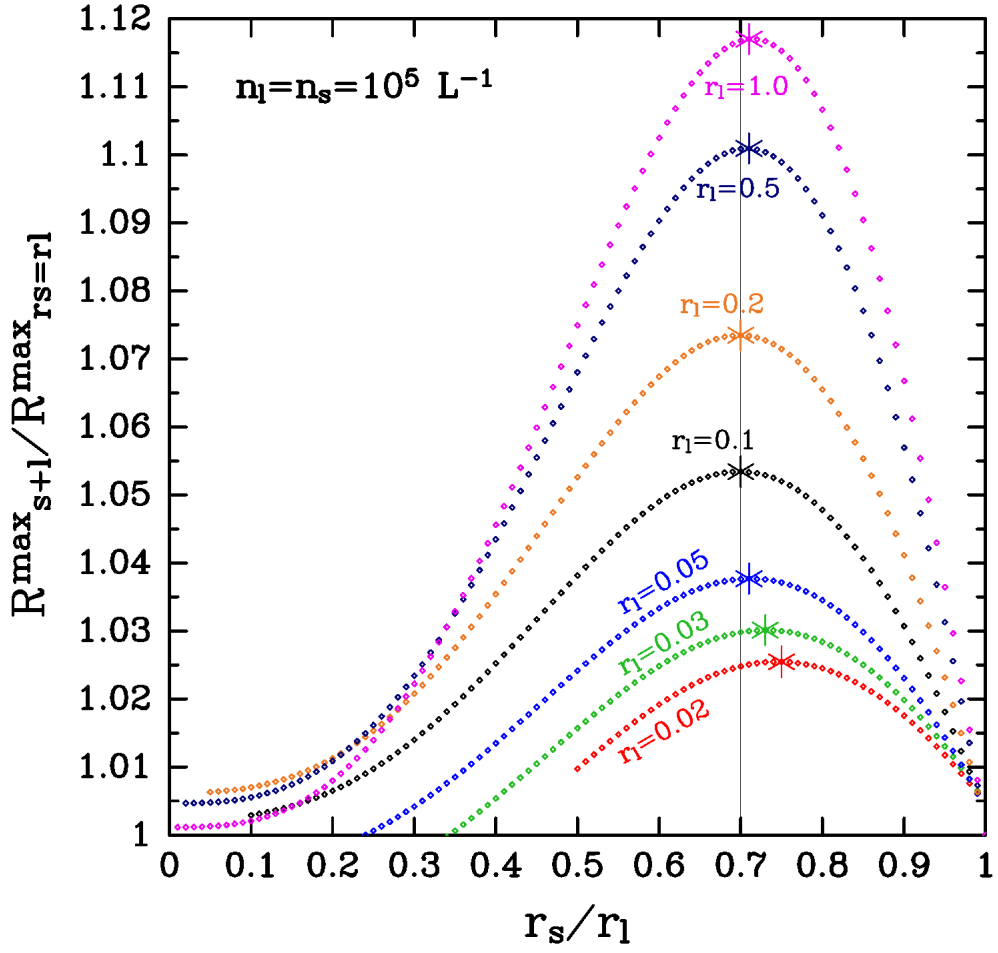

Figure 4.5: Same as Fig. 4.4, but redrawn by normalizing the vertical axis by the maximum ice nucleation ratio when $r_s = r_l$ ($R^{max}_{r_s=r_l}$).

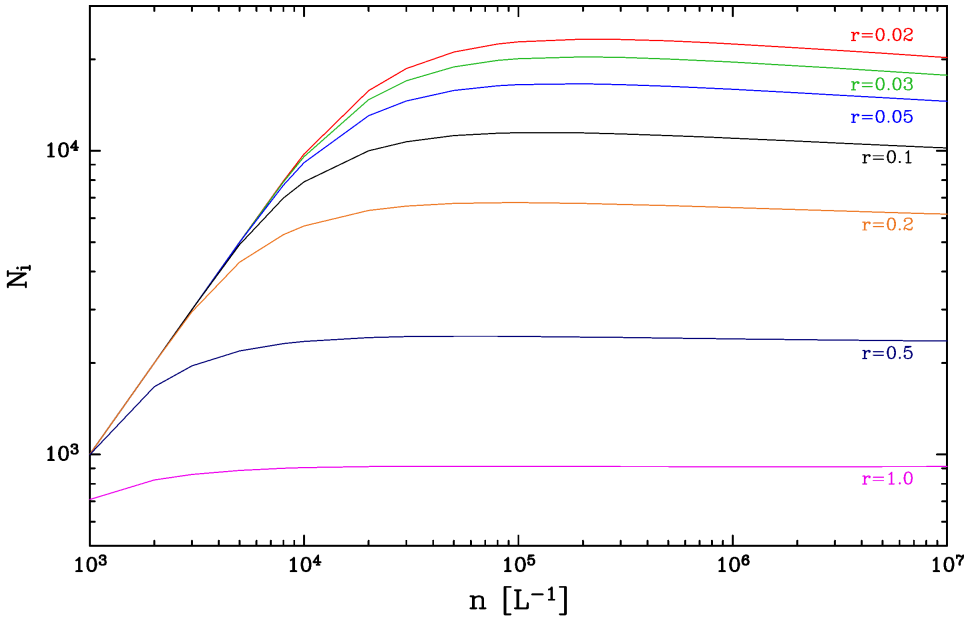

Figure 4.6: The number of ice particles nucleated under the condition of $-\dot{T} = 3.3$ K h^{-1}, $\chi_0 = 6.0$ ppmv and monodisperse aerosols with the radius r of 0.02 (red), 0.03 (green), 0.05 (blue), 0.1 (black), 0.2 (orange), 0.5 (navy-blue), and 1.0 (magenta) μm described as a function of aerosol number concentration. Initial volume of air is set to 1 L.

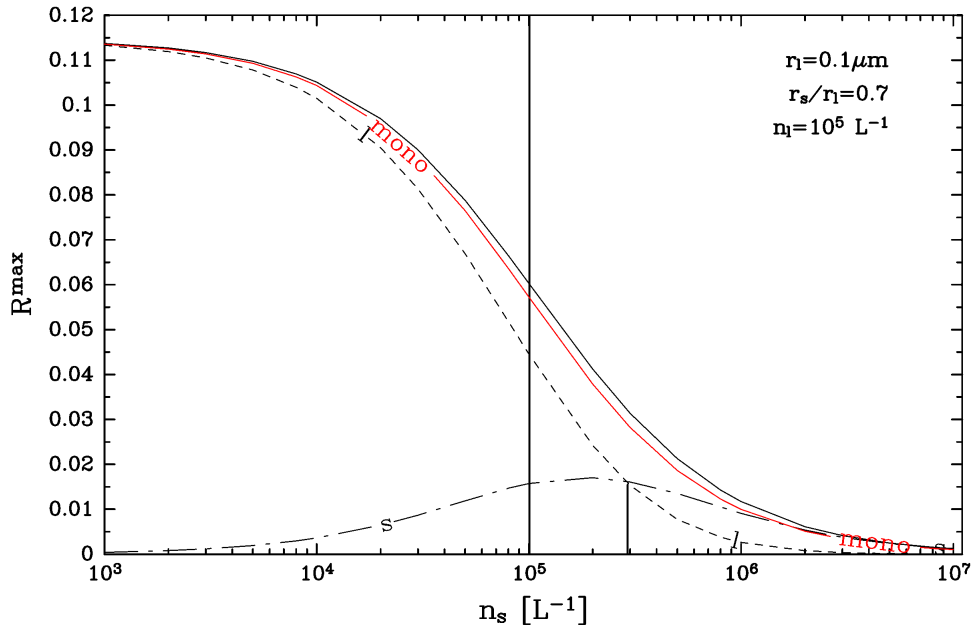

Figure 4.7: The maximum ice-nucleation ratio from large (dashed) and small (dash-dot) aerosols and the sum of them (black solid) as a function of $n_{\rm s}$ simulated under the condition of $-\dot{T} = 3.3$ K h^{-1}, $\chi_0 = 6.0$ ppmv, and the bimodal aerosols of $r_{\rm l} = 0.1$ μm, $r_{\rm s} = 0.07$ μm, and $n_{\rm l} = 10^5$ L^{-1}. Red solid curve indicates the maximum ice nucleation ratio simulated under the same condition but under monodisperse aerosols of $r = 0.1$ μm and $n = n_{\rm l} + n_{\rm s}$.

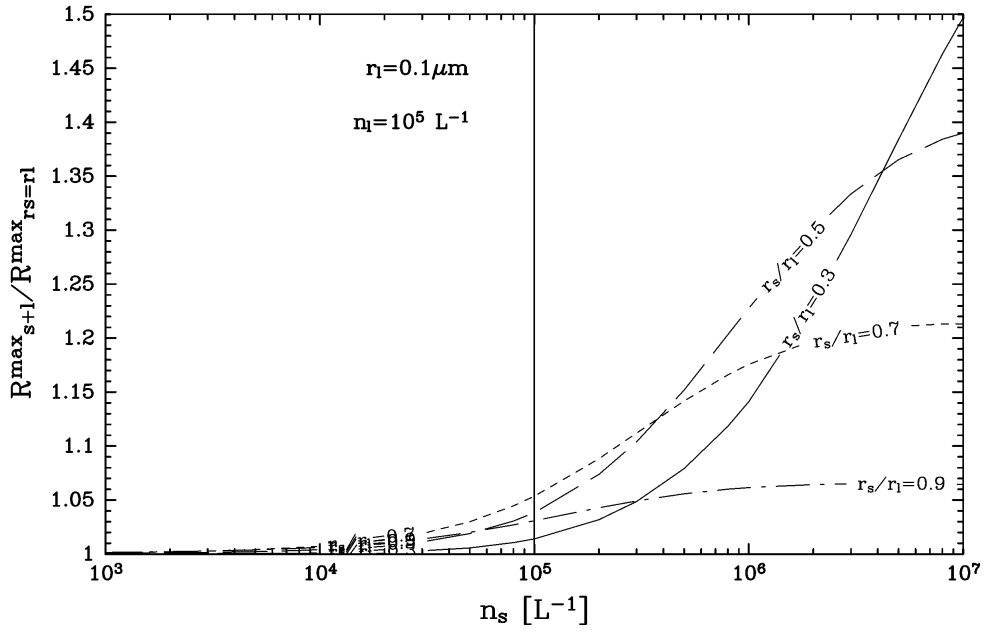

Figure 4.8: The variation of the ratio of $R^{\max}_{s+1}$, calculated under the same condition as in Fig. 4.7, to that under monodisperse aerosols of the radius $r_s = r_l$ ($R^{\max}_{r_s=r_l}$). The results of r_s/r_l =0.3 (solid), 0.5 (dashed), 0.7 (dotted), and 0.9 (dash-dot) are shown.

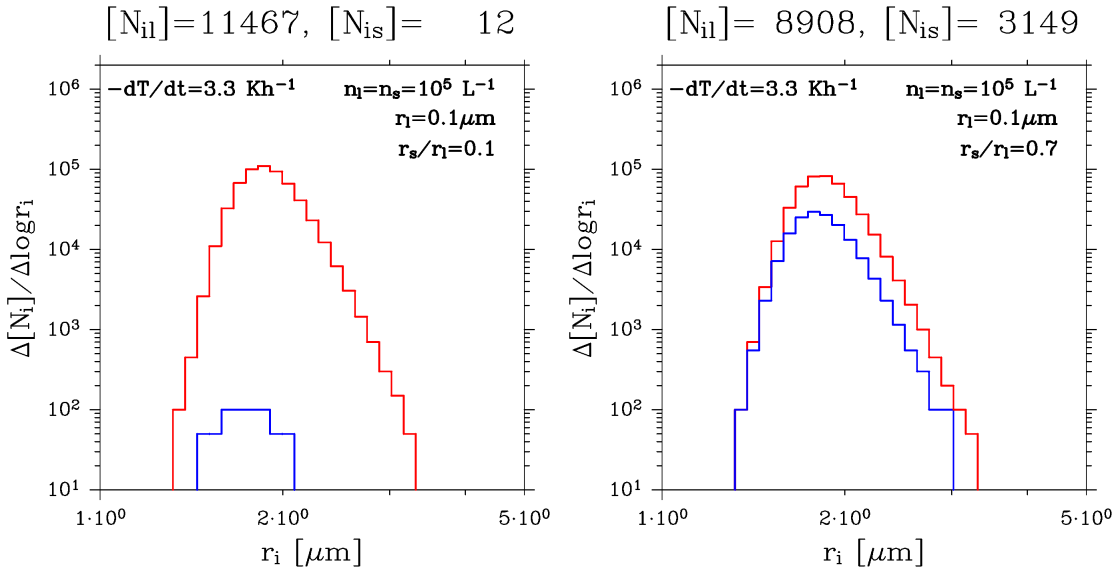

Figure 4.9: The ice-particle size distributions nucleated from large (red) and small (blue) aerosols at the time when the supersaturation is almost dissolved ($RH_i < 101\%$) for the cases of $r_s/r_l = 0.1$ (left panel) and $r_s/r_l = 0.7$ (right panel). Simulations are conducted under the condition of $-\dot{T} = 3.3$ K h^{-1}, $\chi_0 = 6.0$ ppmv, $r_l = 0.1$ μm, and $n_l = n_s = 10^5$ L^{-1}.

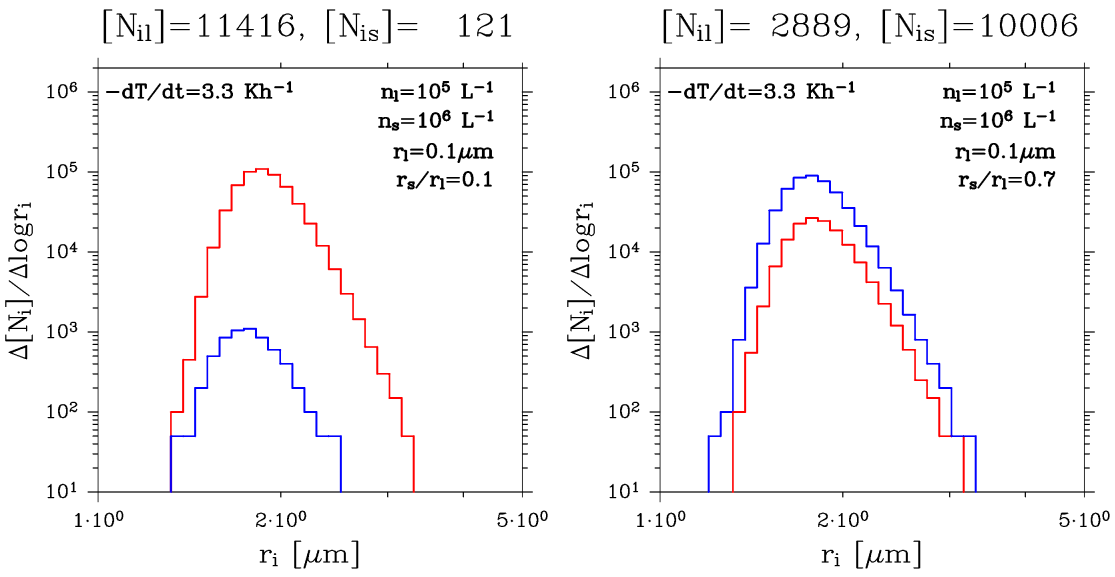

Figure 4.10: Same as Fig. 4.9, but for the cases of $n_{\rm s} = 10^6$ L^{-1} and $r_{\rm s}/r_{\rm l} = 0.1$ (left panel) and 0.7 (right panel).

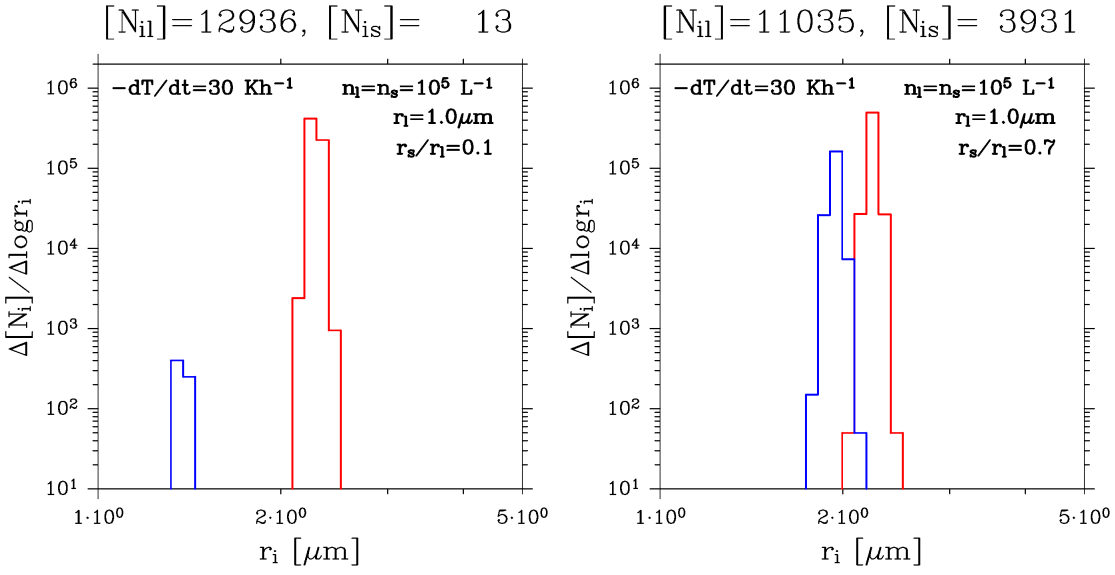

Figure 4.11: Same as Fig. 4.9, but for the results under the condition of $-\dot{T} = 30$ K h^{-1} and $r_{\rm l} = 1.0$ μm.

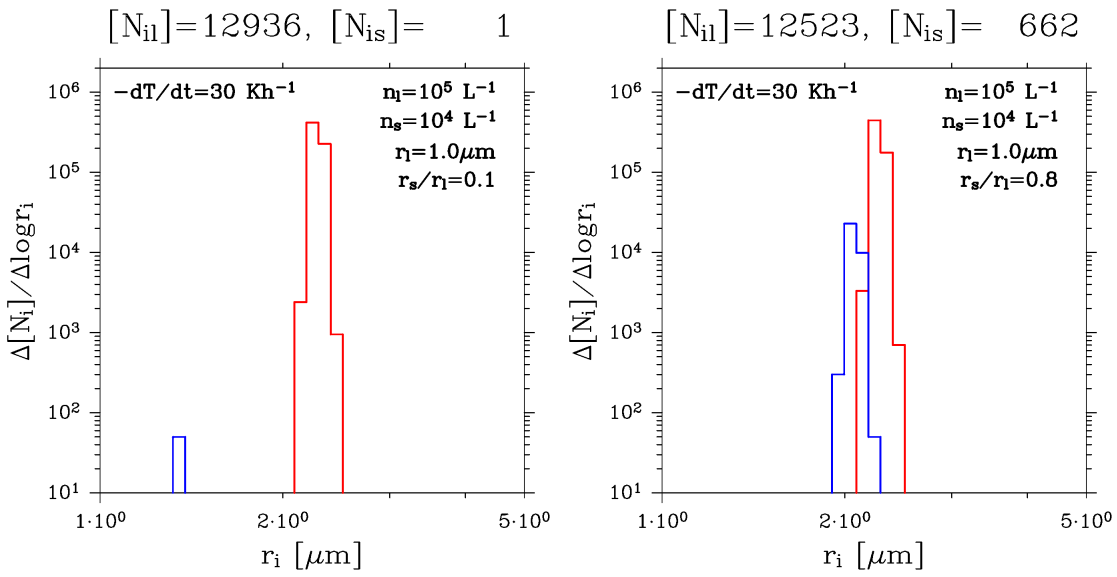

Figure 4.12: Same as Fig. 4.11, but for the cases of $n_{\rm s} = 10^4$ L^{-1} and $r_{\rm s}/r_{\rm l} = 0.1$ (left panel) and 0.8 (right panel).

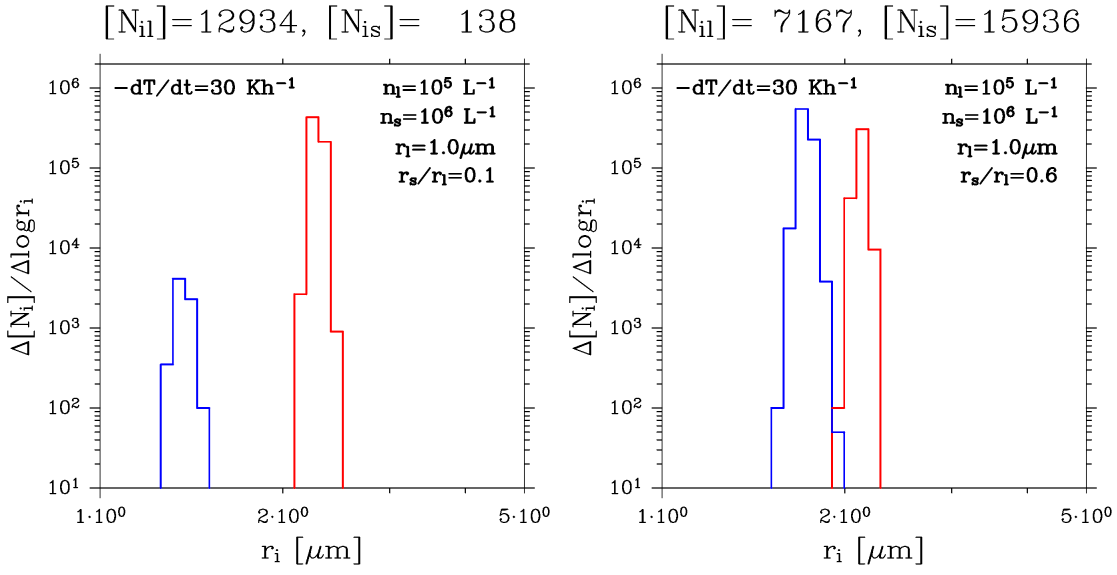

Figure 4.13: Same as Fig. 4.11, but for the cases of $n_{\rm s} = 10^6$ L^{-1} and $r_{\rm s}/r_{\rm l} = 0.1$ (left panel) and 0.6 (right panel).

Chapter 5

Discussion

5.1 Time scales associated with the TTL cirrus

The time scale of the formation of the observed TTL cirrus (Fig. 1.7(C)) characterized by high ice-particle concentration (10^4 L^{-1}) and thin structure (20 m) could be evaluated by the sum of that of the ice nucleation (10^0–10^1 minutes) and that of dissolving the supersaturation due to ice-particle growth (10^1–10^2 minutes) in the supposed range of the aerosol radius ($\leq$1.0 μm). On the other hand, the time scales for 10-m sedimentation of ice particles with the radius of 0.1 μm, 1 μm and 10 μm are estimated to be 5×10^4, 5×10^2 and 5×10^0 hours, respectively. As the former is much shorter than the later, it should be rare to observe the cirrus under the progress of formation and most of the observed cirrus will have completed ice nucleation. Referring to the ice-particle size distribution simulated in Sections 3.3 and 4.4, we could expect that the radius of ice particles nucleated from relatively small aerosols ($r_{\rm l}$ = 0.1 μm) will distribute in the range of 1.32–3.31 μm irrespective of the value of $r_{\rm s}$. The time scale for 10-m sedimentation of ice particles with the radius of 1.32–3.31 μm is estimated to be 13–2 days. Because the difference in the time scales of sedimentation are large for relatively small aerosols due to the broad size spectrum, the size distribution of the TTL cirrus formed under such condition will be

quickly deformed by differential sedimentation. The evaluated time scale, by taking only the effect of sedimentation into account, for conserving the primary size distribution of nucleated ice particles in the TTL cirrus will be $\sim$ 2 days. In the case of $r_{\rm l} = 1.0$ μm, on the other hand, the radius range and the time scale of 10-m sedimentation are 1.32–2.51, 1.74–2.51 and 2.09–2.51 μm, and 13–3, 7–3 and 5–3 days, for ice particles nucleated under the condition of $r_{\rm s}/r_{\rm l} = 0.1$, 0.7 and 1.0, respectively. As the difference in the radius of nucleated ice particles is small and the time scale for sedimentation is relatively short in the case of large aerosols, the primary size distribution of nucleated ice particles is conserved relatively long. The estimated time scales for conserving the primary size distributions of ice particles are 4–5, 6–7 and 11 days under the condition of $r_{\rm s}/r_{\rm l} = 0.1$, 0.7 and 1.0, respectively.

5.2 The amplification effect of ice nucleation

The amplification effect of ice nucleation under bimodal aerosol condition could be understood qualitatively as follows. Under bimodal condition, those small ice particles nucleated from small aerosols make up only a small portion of the ice particles. Such small ice particles cannot contribute much to the water vapor uptake and the reduction of relative humidity over ice ($\rm RH_i$) by their growth because of the small surface area and the small population. Thus the number of ice particles increases (amplification effect under the mixture of small aerosols as compared to the monodisperse aerosol condition).

The determination of the value of $r_{\rm s}/r_{\rm l}$ corresponding to the maximum of the amplification effect must be made carefully. The number of nucleated ice particles [$N_{\rm i}$] shows different time evolution after the first ice nucleation from small aerosols ([$N_{\rm is}$]$\geq$1) even if the difference in $r_{\rm s}/r_{\rm l}$ is small (i.e., $\delta(r_{\rm s}/r_{\rm l})$=0.001). The difference in the maximum number of nucleated ice particles $N_{\rm i}^{\rm max}$ arises from the delicate $r_{\rm s}/r_{\rm l}$-dependency of the amplification effect of ice nucleation (Fig. 4.5). Because the time interval of numerical

integration (Δt) is finite, the increment of $[N_{\rm i}]$ per one time step becomes too large when Δt is not taken to be small enough, making the precision of the simulation poor. The maximum of the amplification effect indicated by asterisks in Fig. 4.5 is thus determined carefully by taking the value of $\Delta t = 10^{-3}$ second in the case of large $r_{\rm l}$ while $\Delta t = 10^{-4}$ second for small $r_{\rm l}$ to realize the precision of 0.001 in $r_{\rm s}/r_{\rm l}$.

The value of $r_{\rm s}/r_{\rm l}$ that gives the maximum amplification effect is close to 0.7 irrespective of the value of $r_{\rm l}$ when $n_{\rm l} = n_{\rm s} = 10^5$ L^{-1}. As we can see from Fig. 4.5, there found small fluctuations such as $r_{\rm s}/r_{\rm l}$=0.714 and 0.698 when $r_{\rm l}$=1.0 and 0.1 μm, respectively. The specific $r_{\rm s}/r_{\rm l}$ decreases slightly as $r_{\rm l}$ becomes small when $r_{\rm l} \leq$0.1 μm. At this moment, we have no explanation as to why the specific values of $r_{\rm s}/r_{\rm l}$ are $\sim$0.7 and how these values depend on $r_{\rm l}$. These problems are left for future studies.

5.3 Size distributions of ice particles

The magnitude of amplification effect discussed in Section 5.2 is no more than 6% under the conditions of $n_{\rm l} = n_{\rm s} = 10^5$ L^{-1}, $-\dot{T} = 3.3$ K h^{-1}, and $r_{\rm l} = 0.1$ μm (Fig. 4.5). It becomes large for large $r_{\rm l}$, but still no more than 12% in the case $r_{\rm l} = 1.0$ μm. Therefore, the assumption of monodisperse aerosols (Chapter 3) to investigate the formation of the observed cirrus (Fig. 1.7(C)) is almost valid on the aspect of ice-particle concentration.

On the other hand, there is a clear limitation in the assumption of monodisperse aerosols because the size distribution of nucleated ice particles is always monodisperse under a constant cooling rate. In fact, the size distribution of nucleated ice particles shows two distinct maxima when appropriate parameters are chosen under bimodal aerosol condition. The set of parameters suitable for bimodal ice-particle distributions could be found in the domain where the dependencies of the number concentration of ice particles are large on both the heating rate and aerosol radius (e.g., $-\dot{T} = 30$ K h^{-1}, $r_{\rm l} = 1.0$ μm).

The features of the size distribution and the mode radius of nucleated ice particles

under bimodal aerosols are summarized as follows. When the aerosols are small and the cooling rates necessary for the formation of the ice particles in the concentration of 10^4 L^{-1} are small, small ice particles are nucleated due to Effect (a) and the mode radius is small. As the ice nucleation takes long, the difference in the length of exposure to supersaturation makes the growth of individual particles different depending on the timing of ice nucleation, and results in a broad size spectrum. This feature implies that the accommodation coefficient α which determines the efficiency of water vapor uptake by ice particle causes the change of ice-particle size distribution. In this study, the uncertainty of the maximum ice concentration associated with the variation of α is shown by the range of parameters corresponding to the change of α between 0.2 and 1.0 (Fig. 3.4). There are some studies, however, that report the minimum α to be 0.004 (e.g., *Pruppacher et al.*, 1998; *Magee et al.*, 2006). For this reason, the size distribution of nucleated ice particles is investigated by extending the range of α to be $0.001 \leq \alpha$. The results indicate that the small values of α result in a small mode radius and broad size spectrum of nucleated ice particles as expected (not shown).

The size distribution of ice particles in the cirrus clouds were observed by ATTREX2011 (*Jensen et al.*, 2013b). In the thin cirrus cloud of our interest (Fig. 1.7(C)), it is found that most of the ice particles are categorized in the bin of 0.5–1.6 μm in radius and the remaining ice particles ($\sim 10^2$ L^{-1}) are distributed in the next bin (1.6–4.7 μm). As is pointed out in Chapter 2, this cirrus is observed just a moment after nucleation, indicating that the ice-particle size distribution at the time of the end of nucleation is preserved, and making it possible to compare with our simulations. From such comparisons, we find that the majority of ice particles are categorized not in the bin of 0.5–1.6 μm but of 1.6–4.7 μm in radius for any set of parameters that realize $n_{\mathrm{i}}^{\mathrm{max}} \sim 10^4$ L^{-1}. This disagreement is quite robust and does not change depending on the value of α.

The reason why the simulated ice particles are larger than those observed may be interpreted as follows. Our simulations require that the ice particles in the concentration

of 10^4 L^{-1} must be nucleated from 2.5 ppmv of water vapor at the time of the termination of ice nucleation. If we assume the nucleated ice particles have the same radius r_i, it will be $\sim$1.9 μm due to the requirement of the conservation of W ($10^4 \times (4/3)\pi {r_i}^3 \rho_i$) to absorbed water vapor ($2.5 \times 10^{-6} p M_w/(R^* T)$) under the pressure of 100 hPa and air volume of 1L. This rough estimation suggests that ice particles will grow up to about 2 μm in radius until the supersaturation is dissolved anyway irrespective of the choice of nucleation parameters. The underestimation of ATTREX observations as compared to our simulations is consistent with the lack of water content in the ATTREX data estimated in Section 2.3. This robustness suggests that the ice-particle radius is underestimated or the water vapor mixing ratio is overestimated in ATTREX2011.

As can be seen from the comparison of ice-particle size distributions between Figs. 2.4 and 3.2, the resolution of the size spectrum in the ATTREX data are quite limited. If the ice-particle size distribution is observed in higher resolution, the formation process of the observed cirrus could be investigated by using the distribution function of ice particles. Furthermore, if the information about initial size distribution of aerosols becomes available at the same time, it may be used to constrain the uncertainties of accommodation coefficient. Detailed information on the size distributions of ice particles and aerosols are quite valuable for further understanding of the formation process of the TTL cirrus.

5.4 Meteorological conditions for the cirrus formation

The cooling rate necessary for the formation of the cirrus with the ice-particle concentration of 10^4 L^{-1} could be determined under the assumption of monodisperse aerosols of a given radius if the meteorological conditions are given (Chapter 3). The atmospheric disturbances responsible for the ice nucleation in the TTL are shown in Table 5.1 summarizing the values of atmospheric parameters such as the ascending speed, time scale of cooling, and associated vertical scale. The time scale associated with Matsuno-Gill pattern

is estimated by assuming horizontal wind velocity of 10 m s^{-1}.

According to the results shown in Fig. 3.4, the cooling rate of no less than 2.4 K h^{-1} is required for the aerosols of $r \geq 0.01$ μm. This cooling rate is converted to the ascending speed of 0.067 m s^{-1} by using following equation: $-\dot{T} \equiv -dT/dt = -(dT/dz)(dz/dt) = -gw/C_{\rm p} = -\Gamma w$, where w, g, and Γ are ascending speed of air, gravity acceleration, and dry adiabatic lapse rate defined as $\Gamma \equiv g/C_{\rm p}$, respectively. If we assume the horizontal motion with the wind speed of 10 m s^{-1}, the corresponding horizontal temperature gradient is -0.067 K km^{-1}. During the progress of ice nucleation for $\sim$10 minutes, the air parcel is cooled by 0.4 K traveling the horizontal distance of 6 km or adiabatically lifted by 0.04 km. These may be regraded as the horizontal and vertical scales of the cirrus formation. If we take the uncertainty of the accommodation coefficient into account, the cooling rate required for the formation of the observed cirrus will be 2–8 K h^{-1}. The meteorological conditions necessary for the formation of the cirrus with ice-particle concentration of 10^4 L^{-1} are summarized in Table 5.2. The estimated ascending speed (0.056–0.22 m s^{-1}) is much larger than the vertical velocity associated with the Matsuno-Gill pattern ($\sim 10^{-6}$ m s^{-1}) and that for synoptic disturbances such as equatorial Kelvin waves (0.002–0.04 m s^{-1}). However, it falls within the range of typical vertical speed of mesoscale disturbances such as gravity waves ($\geq$0.1 m s^{-1}). The spatio-temporal scales associated with mesoscale disturbances are 0.01 to 1 km and 1 to 10^3 minutes, respectively. The time scale of ice nucleation ($\sim$10 minutes) and vertical scale of 0.034–0.13 km are consistent with the above conditions, and we may safely regard the mesoscale disturbances such as gravity waves as the dynamical processes responsible for the formation of the observed cirrus.

5.5 Formation and growth of the TTL cirrus

How the characteristic thin structure (20 m) of Fig. 1.7(C) has been formed is of great interest. The fact that the observed cirrus could be formed in the mesoscale disturbances

does not mean we understand the formation process. Strictly speaking, the thickness of cirrus can not be determined by a single observation flight; it might have cut the edge of a thick cirrus accidentally. The aircraft flew at a horizontal speed of about 200 m s^{-1} accompanied by a slow descent of about 2 m s^{-1} when the cirrus shown in Fig. 1.7(C) was observed. It took 10 second to cross the cirrus which had a horizontal extension of at least 2 km. This horizontal scale is quite natural as it is much smaller than the horizontal scale of TTL cirrus (Section 2.1) reported by *Thomas et al.* (2002). Admitting that we have no further evidence of the thickness of 20 m, it is worth trying to investigate the formation process.

As is pointed out in Section 1.2.1, the rate coefficient of homogeneous nucleation is very sensitive to RH_i, thus T, so that the slight perturbation of RH_i (T) could trigger ice nucleation at some particular altitude. One possible scenario explaining the formation of the thin cirrus is schematically illustrated in Fig. 5.1, which shows given profiles of T (blue solid) and χ (green) at the vicinity of the temperature minimum (cold point) in the TTL. For simplicity, we assume χ is constant around the cold point, and decreases above some altitude shown in black dotted line. T_c, the threshold temperature of ice nucleation (blue dashed line), decreases as the altitude because of the decrease of water vapor pressure, and it decreases rapidly above the black dotted line due to the decrease of χ (panel A). As the air is lifted adiabatically by disturbances, the temperature decreases along the dry adiabat (light-blue dot). The uplift also moves profiles of χ and T_c upward as a whole, but those below the dotted line do not change making a sharp contrast to the rapid decrease of T. When $T \leq T_c$, ice nucleation starts and a thin cirrus (red) is formed (panel B). In this cirrus, χ and T_c have decreased due to the growth of ice particles, which leads the decrease of T_c and termination of ice nucleation. Further cooling moves the upper and lower boundaries of the layer in which $T \leq T_c$ upward and downward, respectively, making the thin cirrus thicker (panel C). The time evolution depicted here is consistent with our notion that the thin cirrus was observed a moment after the initiation of ice nucleation.

In addition, it is also suggested that the two kinds of cirrus with different thickness (Fig. 1.7(A), (C)) are simply observed at different stage of development. If this is the case, the unified scenario illustrated in Fig. 5.1 may well be applicable to the formation of various types of homogeneously-nucleated TTL cirrus with partial modification.

Table 5.1: Typical values of ascending speed and spatio-temporal scales of atmospheric disturbances in the TTL. (a) adiabatic motion associated with the Matsuno-Gill pattern (*Hatsushika and Yamazaki*, 2003) in cold region of the TTL, (b) synoptic disturbances (*Jensen et al.*, 2010; *Spichtinger and Krämer*, 2013; *Tsuda et al.*, 1994; *Suzuki and Shiotani*, 2008), (c) mesoscale disturbances (*Hoyle et al.*, 2005; *Jensen et al.*, 2010; *Jensen and Pfister*, 2004; *Spichtinger and Krämer*, 2013), estimated by assuming the horizontal wind speed of 10 m s^{-1}.

atmospheric disturbances	ascending speed	time scale	vertical scale
(a) Matsuno-Gill pattern	$\sim 10^{-6}$ m s^{-1}	$\sim$5 days	1 km
(b) synoptic disturbances	0.002–0.04 m s^{-1}	$\sim$2–4 days	3–4.5 km
(c) mesoscale disturbances	$\geq$0.1 m s^{-1}	1–10^3 min.	$\geq$0.01–1 km

Table 5.2: Meteorological condition responsible for the formation of the TTL cirrus with ice-particle concentration of 10^4 L^{-1} estimated from the results of numerical simulations conducted under the assumption of monodisperse aerosols. Horizontal wind speed of 10 m s^{-1} and adiabatic motion for 10 minutes are assumed referring to the time scale of ice nucleation.

accommodation coefficient	cooling rate (K h^{-1})	adiabatic ascending speed (m s^{-1})	horizontal temperature gradient (K km^{-1})	spatial scales		temperature change (K)
				horizontal (km)	vertical (km)	
0.2	2.0	0.056	0.056	6	0.03	0.3
0.3	2.4	0.067	0.067	6	0.04	0.4
1.0	8.0	0.22	0.22	6	0.1	1

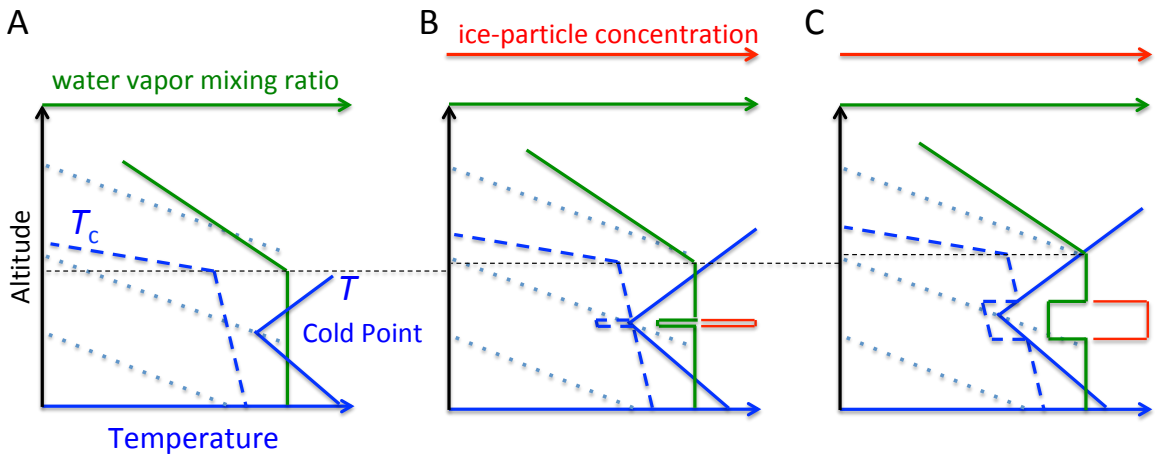

Figure 5.1: Schematic diagrams illustrating the formation of TTL cirrus. (A) Initial profiles of temperature (T; blue solid line), water vapor mixing ratio (χ; green solid line), the threshold temperature at which ice nucleation starts (T_c; blue dashed line), and dry adiabat (light-blue dot line). For simplicity, χ is constant around the cold point, while it decreases above a certain altitude shown by black dotted line. (B) The same as (A) but the air as a whole is lifted, thus cooled, adiabatically with a constant ascending speed. The vertical range of the illustration is much smaller than the vertical wave length of the disturbances responsible for the uplift. Within a thin layer where $T \leq T_c$ around the cold point, ice nucleation starts and a cirrus (ice-particle concentration; red line) is formed. (C) The profiles same as (A) but the air is lifted further. The thin cirrus evolves into a thick cirrus. The magnitude of the uplift in (B) and (C) is small as can be seen from the thin dotted lines.

Chapter 6

Conclusion

This study attempts to identify the formation process of a cirrus cloud observed by Airborne Tropical Tropopause Experiment (ATTREX) in the Tropical Tropopause Layer (TTL). The high concentration of ice particles (10^4 L^{-1}) and the thin structure (20 m) make it possible to assume that this cirrus is formed by homogeneous nucleation and has not yet been perturbed by sedimentation and mixing. A series of numerical experiments simulating isentropic ascent with constant cooling rates are conducted with the aid of a cloud microphysical model by sweeping various parameters that affect ice nucleation.

Under monodisperse aerosol conditions, the ice-particle concentration ($n_{\mathrm{i}}^{\mathrm{max}}$) shows the following features depending on meteorological conditions and aerosol properties:

1. $n_{\mathrm{i}}^{\mathrm{max}}$ increases as the increase of cooling rate.

2. $n_{\mathrm{i}}^{\mathrm{max}}$ decreases as the increase of initial water mixing ratio.

3. $n_{\mathrm{i}}^{\mathrm{max}}$ decreases as the increase of aerosol radius (r) non-linearly pronounced in large r.

4. $n_{\mathrm{i}}^{\mathrm{max}}$ decreases as the increase of accommodation coefficient.

The aerosol radius has the following effects on ice nucleation:

(a) Large (small) aerosols create small (large) numbers of large (small) ice particles due to the size dependency of the growth rate of ice particles.

(b) Large (small) aerosols initiate ice nucleation at a low (high) saturation ratio.

(c) Large aerosols make the mode radius large and the width of the size spectrum narrow.

The interaction between aerosols with different radius (r_l for large and r_s for small aerosols) is investigated by assuming bimodal size distribution. When large and small aerosols have the same number concentrations, the following features are found:

5. The ice nucleation is approximated by monodisperse aerosols of radius r_l when r_l and r_s are much different. This is understood by Effect (b).

6. The interaction emerges when $r_\mathrm{l} \sim r_\mathrm{s}$. The number of nucleated ice particles and the proportion of aerosols having been nucleated to ice (R^max) are larger than those under monodisperse condition. This amplification effect indicates that Effect (a) is also valid in the bimodal case.

7. While the amplification effect is generally large for large r_l, it is most pronounced at $r_\mathrm{s}/r_\mathrm{l} \sim 0.7$ irrespective of r_l.

The effect of the difference in the number concentrations of large (n_l) and small (n_s) aerosols is investigated under the condition of maximum amplification effect ($r_\mathrm{s}/r_\mathrm{l} = 0.7$). The major findings are:

8. R^max decreases monotonously as a function of n_s, while that from small aerosols takes a maximum at around n_sc at which the first nucleating aerosol is switched from small to large.

9. Relative magnitude of R^max for large and small aerosols is reversed at the $r_\mathrm{s}/r_\mathrm{l}$ ratio at which the first nucleating aerosol is switched.

These features suggest that $R^{\max}$ depends strongly on the ice nucleation rate but weakly on the growth rate of nucleated ice particles.

The size distribution of nucleated ice particles is investigated under the condition that reproduces the ice-particle concentration of 10^4 L^{-1}. We find:

10. Under small r_l conditions (e.g., 0.1 μm), the size spectrum of nucleated ice particles is monodisperse and broad irrespective of the values of r_s and n_s, because of the long nucleation time with weak cooling.

11. The bimodal distribution of nucleated ice particles appears in the case of large r_l (e.g., 1.0 μm). This is made possible by the strong cooling having been applied to large aerosols in which ice-particle concentration depends strongly on aerosol radius.

12. The bimodal distribution becomes evident especially when r_s/r_l is small and n_s is large.

The simulated ice particles are found to be larger than those observed by ATRREX2011 in all parameter ranges. This is consistent with the fact that the total water content within the cirrus layer is smaller than that in the immediate vicinity, suggesting that either the radius and/or concentration of ice particles are underestimated or the water vapor mixing ratio is overestimated in the observations. The required cooling rate to reproduce the thin high-ice-concentration cirrus suggests that the uplift associated with mesoscale disturbances may be responsible for its formation. A hypothetical scenario is proposed to explain the formation and development of TTL cirrus in a single story.

Acknowledgements

I would express my deepest gratitude to Prof. Fumio Hasebe, who always supervises, makes helpful discussions, and supports for me with great patience. I would express my hearty gratitude to Prof. T. Watanabe, Prof. M. Fujiwara, Prof. K. Suzuki and Prof. T. Toyota for their helpful and constructive comments. I would also be greatly indebted to Prof. Takashi Shibata for many fruitful cooperations, especially with respect to cloud microphysical model, and helpful suggestions for my study. I would appreciate to constructive comments and encouragements from Prof. M. Hayashi and Prof. S. Iwasaki. I would also appreciate to Dr. Y. Inai, who spared much time for discussion, guidance and encouragement for constructing of my doctoral study. I would be grateful to members of the Soundings of Ozone and Water in the Equatorial Region group for instructive discussions. I would also be grateful to my course's supervisors for their constructive comments and encouragements, to members of my laboratory for their kind cooperations, and to my colleagues for encouragements. I would be thankful to the ATTREX group for providing datasets and the World Meteorological Organization for financial support to attend the Composition and Transport in the Tropical Troposphere and Lower Stratosphere (CT3LS) meeting. I would also be thankful to American Meteorological Society (AMS) for their financial support to attend the 97th AMS Annual Meeting, 19th Conference on Atmospheric Chemistry, Seattle, USA. This work was supported by the Japan Society for the Promotion of Science, Grant-in-Aid for Scientific Research (S) 26220101. Finally, I would thank to my families for their supports and encouragements.

References

Atticks, M., and G. Robinson (1983), Some features of the structure of the tropical tropopause, *Quarterly Journal of the Royal Meteorological Society*, *109*(460), 295–308.

Baustian, K., M. Wise, and M. Tolbert (2010), Depositional ice nucleation on solid ammonium sulfate and glutaric acid particles, *Atmospheric Chemistry and Physics*, *10*(5), 2307–2317.

Borrmann, S., D. Kunkel, R. Weigel, A. Minikin, T. Deshler, J. C. Wilson, J. Curtius, C. M. Volk, C. D. Homan, A. Ulanovsky, et al. (2010), Aerosols in the tropical and subtropical ut/ls: in-situ measurements of submicron particle abundance and volatility, *Atmospheric Chemistry and Physics*, *10*(12), 5573–5592.

Brewer, A. (1949), Evidence for a world circulation provided by the measurements of helium and water vapour distribution in the stratosphere, *Quarterly Journal of the Royal Meteorological Society*, *75*(326), 351–363.

Brock, C., P. Hamill, J. Wilson, H. Jonsson, K. Chan, et al. (1995), Particle formation in the upper tropical troposphere: A source of nuclei for the stratospheric aerosol, *Science-AAAS-Weekly Paper Edition*, *270*(5242), 1650–1652.

Cziczo, D. J., K. D. Froyd, C. Hoose, E. J. Jensen, M. Diao, M. A. Zondlo, J. B. Smith, C. H. Twohy, and D. M. Murphy (2013), Clarifying the dominant sources and mechanisms of cirrus cloud formation, *Science*, *340*(6138), 1320–1324.

Daneva, D., and T. Shibata (2001), Behavior of externally mixed liquid and solid polar stratospheric cloud particles in a numerical box model under temperature decrease, *Polar meteorology and glaciology*, *15*, 32–42.

Danielsen, E. F. (1982), A dehydration mechanism for the stratosphere, *Geophysical Research Letters*, *9*(6), 605–608.

Dobson, G. (1956), Origin and distribution of the polyatomic molecules in the atmosphere, *Proceedings of the Royal Society of London. Series A, Mathematical and Physical Sciences*, *236*(1205), 187–193.

Field, P., R. Wood, P. Brown, P. H. Kaye, E. Hirst, R. Greenaway, and J. Smith (2003), Ice particle interarrival times measured with a fast fssp, *Journal of Atmospheric and Oceanic Technology*, *20*(2), 249–261.

Fuchs, N., and A. G. Sutugin (1971), High-dispersed aerosols, in *Topics in current aerosol research*, p. 1, Elsevier.

Fujiwara, M., S. Iwasaki, A. Shimizu, Y. Inai, M. Shiotani, F. Hasebe, I. Matsui, N. Sugimoto, H. Okamoto, N. Nishi, et al. (2009), Cirrus observations in the tropical tropopause layer over the western pacific, *Journal of Geophysical Research: Atmospheres*, *114*(D9).

Fujiwara, M., H. Vömel, F. Hasebe, M. Shiotani, S.-Y. Ogino, S. Iwasaki, N. Nishi, T. Shibata, K. Shimizu, E. Nishimoto, et al. (2010), Seasonal to decadal variations of water vapor in the tropical lower stratosphere observed with balloon-borne cryogenic frost point hygrometers, *Journal of Geophysical Research: Atmospheres*, *115*(D18).

Fujiwara, M., T. Sugidachi, T. Arai, K. Shimizu, M. Hayashi, Y. Noma, H. Kawagita, K. Sagara, T. Nakagawa, S. Okumura, et al. (2016), Development of a cloud particle sensor for radiosonde sounding, *Atmospheric Measurement Techniques*, *9*(12), 5911.

Goff, J. A. (1946), Low-pressure properties of water from-160 ° f to 212 ° f., *Trans-actions of the American Society of Heating and Ventilating Engineers*, *52*, 95–121.

Hamill, P., O. Toon, and C. Kiang (1977), Microphysical processes affecting stratospheric aerosol particles, *Journal of the Atmospheric Sciences*, *34*(7), 1104–1119.

Hartmann, D. L., J. R. Holton, and Q. Fu (2001), The heat balance of the tropical tropopause, cirrus, and stratospheric dehydration, *Geophysical research letters*, *28*(10), 1969–1972.

Hasebe, F., Y. Inai, M. Shiotani, M. Fujiwara, H. Vömel, N. Nishi, S.-Y. Ogino, T. Shibata, S. Iwasaki, N. Komala, et al. (2013), Cold trap dehydration in the tropical tropopause layer characterised by sower chilled-mirror hygrometer network data in the tropical pacific, *Atmospheric Chemistry and Physics*, *13*(8), 4393–4411.

Hatsushika, H., and K. Yamazaki (2003), Stratospheric drain over indonesia and dehydration within the tropical tropopause layer diagnosed by air parcel trajectories, *Journal of Geophysical Research: Atmospheres*, *108*(D19).

Heymsfield, A. J. (1986), Ice particles observed in a cirriform cloud at- 83 c and implications for polar stratospheric clouds, *Journal of the atmospheric sciences*, *43*(8), 851–855.

Highwood, E., and B. Hoskins (1998), The tropical tropopause, *Quarterly Journal of the Royal Meteorological Society*, *124*(549), 1579–1604.

Holton, J. R., and A. Gettelman (2001), Horizontal transport and the dehydration of the stratosphere, *Geophysical Research Letters*, *28*(14), 2799–2802.

Hoyle, C., B. Luo, and T. Peter (2005), The origin of high ice crystal number densities in cirrus clouds, *Journal of the atmospheric sciences*, *62*(7), 2568–2579.

Inai, Y., F. Hasebe, M. Fujiwara, M. Shiotani, N. Nishi, S.-Y. Ogino, H. Vömel, S. Iwasaki, and T. Shibata (2013), Dehydration in the tropical tropopause layer estimated from the water vapor match, *Atmospheric Chemistry and Physics*, *13*(17), 8623–8642.

Iwasaki, S., K. Maruyama, M. Hayashi, S.-Y. Ogino, H. Ishimoto, Y. Tachibana, A. Shimizu, I. Matsui, N. Sugimoto, K. Yamashita, et al. (2007), Characteristics of aerosol and cloud particle size distributions in the tropical tropopause layer measured with optical particle counter and lidar, *Atmospheric Chemistry and Physics*, *7*(13), 3507–3518.

Jensen, E., and L. Pfister (2004), Transport and freeze-drying in the tropical tropopause layer, *Journal of Geophysical Research: Atmospheres*, *109*(D2).

Jensen, E., L. Pfister, T. Bui, A. Weinheimer, E. Weinstock, J. Smith, J. Pittman, D. Baumgardner, P. Lawson, and M. J. McGill (2005), Formation of a tropopause cirrus layer observed over florida during crystal-face, *Journal of Geophysical Research: Atmospheres*, *110*(D3).

Jensen, E., P. Lawson, B. Baker, B. Pilson, Q. Mo, A. Heymsfield, A. Bansemer, T. Bui, M. McGill, D. Hlavka, et al. (2009), On the importance of small ice crystals in tropical anvil cirrus, *Atmospheric Chemistry and Physics*, *9*(15), 5519–5537.

Jensen, E., L. Pfister, T.-P. Bui, P. Lawson, and D. Baumgardner (2010), Ice nucleation and cloud microphysical properties in tropical tropopause layer cirrus, *Atmospheric Chemistry and Physics*, *10*(3), 1369–1384.

Jensen, E., R. Lawson, J. Bergman, L. Pfister, T. Bui, and C. Schmitt (2013a), Physical processes controlling ice concentrations in synoptically forced, midlatitude cirrus, *Journal of Geophysical Research: Atmospheres*, *118*(11), 5348–5360.

Jensen, E. J., G. Diskin, R. P. Lawson, S. Lance, T. P. Bui, D. Hlavka, M. McGill, L. Pfister, O. B. Toon, and R. Gao (2013b), Ice nucleation and dehydration in the

tropical tropopause layer, *Proceedings of the National Academy of Sciences*, *110*(6), 2041–2046.

Jensen, E. J., L. Pfister, D. E. Jordan, D. W. Fahey, P. A. Newman, T. Thornberry, A. Rollins, G. Diskin, T. P. Bui, M. McGill, et al. (2013c), The nasa airborne tropical tropopause experiment (attrex), *SPARC Newsletter*, *41*, 15–24.

Jensen, E. J., L. Pfister, D. E. Jordan, T. V. Bui, R. Ueyama, H. B. Singh, T. D. Thornberry, A. W. Rollins, R.-S. Gao, D. W. Fahey, et al. (2017), The nasa airborne tropical tropopause experiment: High-altitude aircraft measurements in the tropical western pacific, *Bulletin of the American Meteorological Society*, *98*(1), 129–143.

Kärcher, B., and U. Lohmann (2002a), A parameterization of cirrus cloud formation: Homogeneous freezing of supercooled aerosols, *Journal of Geophysical Research: Atmospheres*, *107*(D2).

Kärcher, B., and U. Lohmann (2002b), A parameterization of cirrus cloud formation: Homogeneous freezing including effects of aerosol size, *Journal of Geophysical Research: Atmospheres*, *107*(D23).

Kay, J. E., and R. Wood (2008), Timescale analysis of aerosol sensitivity during homogeneous freezing and implications for upper tropospheric water vapor budgets, *Geophysical Research Letters*, *35*(10).

Koop, T., B. Luo, A. Tsias, and T. Peter (2000), Water activity as the determinant for homogeneous ice nucleation in aqueous solutions, *Nature*, *406*(6796), 611–614.

Korolev, A., E. Emery, J. Strapp, S. Cober, and G. Isaac (2013), Quantification of the effects of shattering on airborne ice particle measurements, *Journal of Atmospheric and Oceanic Technology*, *30*(11), 2527–2553.

Krämer, M., C. Schiller, A. Afchine, R. Bauer, I. Gensch, A. Mangold, S. Schlicht, N. Spelten, N. Sitnikov, S. Borrmann, et al. (2009), Ice supersaturations and cirrus cloud crystal numbers, *Atmospheric Chemistry and Physics*, *9*(11), 3505–3522.

Lawson, R., B. Pilson, B. Baker, Q. Mo, E. Jensen, L. Pfister, and P. Bui (2008), Aircraft measurements of microphysical properties of subvisible cirrus in the tropical tropopause layer, *Atmospheric Chemistry and Physics*, *8*(6), 1609–1620.

Lynch, D. K., K. Sassen, D. O. Starr, and G. Stephens (2002), *Cirrus*, Oxford University Press.

Magee, N., A. M. Moyle, and D. Lamb (2006), Experimental determination of the deposition coefficient of small cirrus-like ice crystals near- 50 ° c, *Geophysical Research Letters*, *33*(17).

Marenco, A., V. Thouret, P. Nédélec, H. Smit, M. Helten, D. Kley, F. Karcher, P. Simon, K. Law, J. Pyle, et al. (1998), Measurement of ozone and water vapor by airbus in-service aircraft: The mozaic airborne program, an overview, *Journal of Geophysical Research: Atmospheres*, *103*(D19), 25,631–25,642.

Maruwaka, K. (2009), High ice supersaturation in cirrus clouds observed near tropical tropopause (in japanese), Master's thesis, Graduate School of Environmental Studies, Nagoya University.

McFarquhar, G. M., A. J. Heymsfield, J. Spinhirne, and B. Hart (2000), Thin and subvisual tropopause tropical cirrus: Observations and radiative impacts, *Journal of the atmospheric sciences*, *57*(12), 1841–1853.

McFarquhar, G. M., J. Um, M. Freer, D. Baumgardner, G. L. Kok, and G. Mace (2007), Importance of small ice crystals to cirrus properties: Observations from the tropical warm pool international cloud experiment (twp-ice), *Geophysical research letters*, *34*(13).

Mimura, S., F. Hasebe, and T. Shibata (2016), Constraints on the formation of high-ice-concentration thin cirrus in the tropical tropopause layer, *SOLA*, *12*(Special_Edition), 18–21.

Mote, P. W., K. H. Rosenlof, M. E. McIntyre, E. S. Carr, J. C. Gille, J. R. Holton, J. S. Kinnersley, H. C. Pumphrey, J. M. Russell, and J. W. Waters (1996), An atmospheric tape recorder: The imprint of tropical tropopause temperatures on stratospheric water vapor, *Journal of Geophysical Research: Atmospheres*, *101*(D2), 3989–4006.

Murphy, D. M., and T. Koop (2005), Review of the vapour pressures of ice and supercooled water for atmospheric applications, *Quarterly Journal of the Royal Meteorological Society*, *131*(608), 1539–1565.

Newell, R. E., and S. Gould-Stewart (1981), A stratospheric fountain?, *Journal of the Atmospheric Sciences*, *38*(12), 2789–2796.

Peter, T., B. Luo, M. Wirth, C. Kiemle, H. Flentje, V. A. Yushkov, V. Khattatov, V. Rudakov, A. Thomas, S. Borrmann, et al. (2003), Ultrathin tropical tropopause clouds (uttcs): I. cloud morphology and occurrence, *Atmospheric Chemistry and Physics*, *3*(4), 1083–1091.

Peter, T., C. Marcolli, P. Spichtinger, T. Corti, M. B. Baker, and T. Koop (2006), When dry air is too humid, *Science*, *314*(5804), 1399–1402.

Pratte, P., H. van den Bergh, and M. J. Rossi (2006), The kinetics of h2o vapor condensation and evaporation on different types of ice in the range 130- 210 k, *The Journal of Physical Chemistry A*, *110*(9), 3042–3058.

Pruppacher, H. R., J. D. Klett, and P. K. Wang (1998), Microphysics of clouds and precipitation.

Sakurai, M., and T. Shibata (2012), Numerical experiments focusing on the relation between aerosol and the cirrus formation in the tropical tropopause layer (in japanese), in *Semi-annual Meeting of Meteorological Society of Japan*, vol. October 5th.

Sherwood, S. C. (2000), A stratospheric "drain" over the maritime continent, *Geophysical research letters*, *27*(5), 677–680.

Shi, X., X. Liu, and K. Zhang (2015), Effects of pre-existing ice crystals on cirrus clouds and comparison between different ice nucleation parameterizations with the community atmosphere model (cam5), *Atmospheric Chemistry and Physics*, *15*(3), 1503–1520.

Shibata, T., H. Vömel, S. Hamdi, S. Kaloka, F. Hasebe, M. Fujiwara, and M. Shiotani (2007), Tropical cirrus clouds near cold point tropopause under ice supersaturated conditions observed by lidar and balloon-borne cryogenic frost point hygrometer, *Journal of Geophysical Research: Atmospheres*, *112*(D3).

Shibata, T., M. Hayashi, A. Naganuma, N. Hara, K. Hara, F. Hasebe, K. Shimizu, N. Komala, Y. Inai, H. Vömel, et al. (2012), Cirrus cloud appearance in a volcanic aerosol layer around the tropical cold point tropopause over biak, indonesia, in january 2011, *Journal of Geophysical Research: Atmospheres*, *117*(D11).

Skrotzki, J., P. Connolly, M. Schnaiter, H. Saathoff, O. Möhler, R. Wagner, M. Niemand, V. Ebert, and T. Leisner (2013), The accommodation coefficient of water molecules on ice–cirrus cloud studies at the aida simulation chamber, *Atmospheric Chemistry and Physics*, *13*(8), 4451–4466.

Solomon, S., K. H. Rosenlof, R. W. Portmann, J. S. Daniel, S. M. Davis, T. J. Sanford, and G.-K. Plattner (2010), Contributions of stratospheric water vapor to decadal changes in the rate of global warming, *Science*, *327*(5970), 1219–1223.

Spichtinger, P., and D. J. Cziczo (2010), Impact of heterogeneous ice nuclei on homoge-

neous freezing events in cirrus clouds, *Journal of Geophysical Research: Atmospheres*, *115*(D14).

Spichtinger, P., and K. Gierens (2009), Modelling of cirrus clouds–part 1b: Structuring cirrus clouds by dynamics, *Atmospheric Chemistry and Physics*, *9*(2), 707–719.

Spichtinger, P., and M. Krämer (2013), Tropical tropopause ice clouds: a dynamic approach to the mystery of low crystal numbers, *Atmospheric Chemistry and Physics*, *13*(19), 9801–9818.

Spichtinger, P., K. Gierens, and W. Read (2003), The global distribution of ice-supersaturated regions as seen by the microwave limb sounder, *Quarterly Journal of the Royal Meteorological Society*, *129*(595), 3391–3410.

Suzuki, J., and M. Shiotani (2008), Space-time variability of equatorial kelvin waves and intraseasonal oscillations around the tropical tropopause, *Journal of Geophysical Research: Atmospheres*, *113*(D16).

Thomas, A., S. Borrmann, C. Kiemle, F. Cairo, M. Volk, J. Beuermann, B. Lepuchov, V. Santacesaria, R. Matthey, V. Rudakov, et al. (2002), In situ measurements of background aerosol and subvisible cirrus in the tropical tropopause region, *Journal of Geophysical Research: Atmospheres*, *107*(D24).

Tsuda, T., Y. Murayama, H. Wiryosumarto, S. W. B. Harijono, and S. Kato (1994), Radiosonde observations of equatorial atmosphere dynamics over indonesia: 1. equatorial waves and diurnal tides, *Journal of Geophysical Research: Atmospheres*, *99*(D5), 10,491–10,505.

Ueyama, R., E. J. Jensen, L. Pfister, G. S. Diskin, T. Bui, and J. M. Dean-Day (2014), Dehydration in the tropical tropopause layer: A case study for model evaluation using aircraft observations, *Journal of Geophysical Research: Atmospheres*, *119*(9), 5299–5316.

Weisenstein, D., J. Penner, M. Herzog, and X. Liu (2007), Global 2-d intercomparison of sectional and modal aerosol modules, *Atmospheric Chemistry and Physics*, *7*(9), 2339–2355.

Wise, M. E., K. J. Baustian, and M. A. Tolbert (2010), Internally mixed sulfate and organic particles as potential ice nuclei in the tropical tropopause region, *Proceedings of the National Academy of Sciences*, *107*(15), 6693–6698.